University of California
Los Angeles

Stochastic Systems Far From Equilibrium

A dissertation submitted in partial satisfaction
of the requirements for the degree
Doctor of Philosophy in Physics

by

Christian Vaca

2015

Abstract of the Dissertation

Stochastic Systems Far From Equilibrium

by

Christian Vaca

Doctor of Philosophy in Physics

University of California, Los Angeles, 2015

Professor Alexander Jacob Levine, Chair

We discuss some general methodology used to study stochastic systems outside of equilibrium, be it mechanical or thermal equilibrium via the use of the Master equation or Langevin-like methods. We apply these methods to the following problems in non-equilibrium statistical mechanics: The nonlinear dynamics of semiflexible filaments networks under load, the position-velocity distribution of an ion trapped in an RF-trap in the presence of two different buffer gasses at different temperatures, and the response function of two harmonically coupled particles near a mechanical phase transition interacting with a non-Gaussian and Gaussian, white noise source. We find that the movement of a tracer particle in semiflexible networks is governed by single filament crosslinker rupture events. For the ion trapped in the RF-trap, we find non-Maxwellian probability distributions for the system far from equilibrium but in a steady state. We find the response function for the two harmonically coupled particles shows new interactions with the dissipative background due to the introduction of non-Gaussian noise in a spatially asymmetric fashion to lowest order in perturbation theory. Finally we discuss extensions of the methods used to future work.

The dissertation of Christian Vaca is approved.

Robijn Bruinsma

William Klug

Alexander Jacob Levine, Committee Chair

University of California, Los Angeles

2015

To my parents and L.V....
Only with your guidance and love
was I able to rebel enough to
accomplish anything worthwhile

Table of Contents

List of Figures

List of Tables

Acknowledgments

First and foremost, I would like to thank my advisor, Alex Levine for constantly pushing me to be a better scientist. He inspired me to become a physicist as an undergraduate in chemistry while taking his quantum mechanics course at UCLA. I was amazed by all the beautiful Feynman diagrams that he drew one day during the discussion of propagators in lecture. I had no idea what any of it meant and most of the lecture was lost upon me; This was the first time in my undergraduate career that I had ever experienced such a thing. Too long had I been taking the easy route through my academic career, and Alex challenged me in that quantum mechanics course (whether to his knowledge or not is another question), forever changing my life. I knew I had to be able to work and understand these mysterious symbols, and (for the most part) I can do that today. Alex gave me the liberty to explore as many courses as I wished in physics and satisfy my intellectual curiosity to learn as much about the universe as I possibly could. He is a brilliant physicist and good man who has taught me problem solving skills that I will hold onto dearly for the rest of my life.

Next I would like like to thank my office mates, Devin Kachan, Art Evans, Roie Shlomovitz, and Louis Foucard. All of these men have listened to me ramble on and on about my work and the frustrations that went along with it, providing me key insights many times to progress past the difficulties presented in many of my problems during graduate school. Their intelligence provided me just enough insecurity to push myself to become a better scientist and thinker, and for that I am grateful. I will never forget the intellectual discussions that happened in our office in the Geology building, and I hope to continue those discussions into the future.

To all of the faculty and friends I met throughout my career at UCLA and elsewhere that I have had discussions with regarding the nature of the universe among other things, you are not lost in my thoughts. The Biophysics group meetings and Soft Matter Journal Club were among the highlights of my graduate career, and those vibrant discussions during those meetings showed me the heart and soul of science.

Finally, I would like to thank my fiance, Loren. We met during my second year of

graduate school and little did I know then that the most important thing to my success in graduate school would be your love and support. You were my biggest supporter on all my projects, and you kept me from falling apart when things were their roughest. I would not have finished this work without you and for that I will be eternally grateful.

-C.V.

Vita

2007	Student at Consumnes River College
Summer 2007	Intern, Center for Biophotonics University of California, Davis
2009	B.S. (Chemistry-Physical Chemistry Concentration), University of California, Los Angeles.
2009–2012	Teaching Assistant, Chemistry Department, UCLA.
2012	M.S. (Physical Chemistry), UCLA.
2012–2015	Teaching Assistant, Physics Department, UCLA.
2012–2015	Research Assistant, Physics Department, UCLA.
2013–2015	Ph.D. Candidate, Physics Department, UCLA.

Publications

Christian Vaca, Yali Yang, Megan Valentine, and Alex J. Levine, *Bond breaking dynamics in semiflexible networks under load*, Soft Matter, 2015. Research article.

CHAPTER 1

Introduction

1.1 Markov Processes

Disordered systems are ubiquitous throughout the study of condensed matter systems. Given the enormous number of particles that must be taken into account in the study of physical phenomena at mesoscopic scales[1] and larger, it no longer becomes possible to make definite, quantitative statements about systems at these length scales and one must resort to statistical statements of the expected behavior of said system due to atomic fluctuations. The shear complexity of systems with such a large amount of constituents has been studied in great detail for systems at thermal equilibrium, and a variety of very powerful theorems have arisen for systems near thermal equlibrium including the fluctuation-dissipation theorem[48] among many others. However, the search to find universal theoretical tools to explain statistical mechanical systems outside of thermal equilibrium has so far eluded even the best of intellectual efforts. There are no analogous statements to the results of the fluctuation-dissipation theorem for systems far out of thermal equilibrium to date, though many attempts have been made.

Nevertheless, it is still possible to describe systems outside of thermal equilibrium by the use of stochastic calculus as well as a detailed understanding of the form of the physical fluctuations of the system in question. Though no universal laws governing the behavior of thermodynamics systems outside of equilibrium have been discovered, we nevertheless seek to describe and characterize some features common among all non-equilibrium systems and outline some general principles to study these systems.

We will denote a general stochastic process as $x(t)$, where it may stand for the time evolution of any tensorial object of any rank. A particular subclass of stochastic processes

[1] Mesoscopic is taken to mean systems greater than the size of small molecules $\mathcal{O}(\text{Å})$

that have been ubiquitously studied in physics and chemistry due to their simplicity are the Markov processes which are defined in terms of the following conditional probability statement [2]

$$P_{1|n-1}(x_n, t_n|x_{n-1}, t_{n-1}; ...; x_1, t_1) = P_{1|1}(x_n, t_n|x_{n-1}, t_{n-1}); \qquad (1.1)$$
$$t_1 < t_2 < ... < t_n$$

where $P_{1|1}(x_n, t_n|x_{n-1}t_{n-1})$ denotes the conditional probability of being in the state x_n at time t_n given that the system was in the state x_{n-1} at time t_{n-1}. An analogous definition holds for $P_{1|n-1}$ [44],[2]. This conditional probability statement from Eq. (1.1) simply says that the conditional probability of observing the system at state x_n at time t_n is only dependent on the immediate history of the stochastic process and not any of the times before then i.e. $\{t_{n-2}, t_{n-3}, \ldots, t_1\}$.

These Markov processes are among the most simple set of stochastic processes to study due to their analytic tractability, however determining whether a physical process is amenable to a Markov process analysis is dependent on choosing an appropriate time scale. The condition for a stochastic process to be described by a Markov process is that we choose a time step Δt sufficient large [2] to remove any time memory of the stochastic fluctuations associated with the stochastic process yet short enough to not lose any of the relevant aspects of the dynamics of the system. How to chose this time scale is dependent upon the exact phenomenology of the system under study. In practice however, there is very rarely a physical system where an appropriate Δt cannot be chosen to model the system as Markovian.

Assuming that all the processes which we will be studying are of the Markov type and given Eq. (1.1), we may define all joint probability densities
$P_n(x_1, t_1; x_2, t_2; \ldots, : x_n, t_n)$ i.e. the probability of observing the stochastic process x to have value x_1 at time t_1, x_2 at time t_2, etc. using the related conditional probability distributions of

$$\begin{aligned} P_3(x_1, t_1; x_2, t_2; x_3, t_3) =& P_2(x_1, t_1; x_2, t_2) P_{1|2}(x_3, t_3|x_1, t_1; x_2, t_2) \\ =& P_1(x_1, t_1) P_{1|1}(x_2, t_2|x_1, t_1) P_{1|1}(x_3, t_3; x_2, t_2). \end{aligned} \qquad (1.2)$$

[2] We assume the reader is familiar with Bayes' theorem regarding conditional probabilities

it is clear that this process can be iterated for any of the P_n, giving the aforementioned analytic tractability of the Markov Process. The only distributions that will be needed to describe any of the joint probabilities will be the P_1 and $P_{1|1}$ distributions. We establish the next relationship from Eq. (1.1), the Chapman-Kolmogorov equation which is

$$P_2(x_1,t_1;x_3,t_3) = P_1(x_1,t_1)\int \mathrm{d}x_2 P_{1|1}(x_2,t_2|x_1,t_1)P_{1|1}(x_3,t_3|x_2,t_2).$$

Dividing by $P_1(x_1,t_1)$ and using the Markov property of Eq. 1.2 yields

$$P_{1|1}(x_3,t_3|x_1,t_1) = \int \mathrm{d}x_2 P_{1|1}(x_2,t_2|x_1,t_1)P_{1|1}(x_3,t_3|x_2,t_2). \tag{1.3}$$

This identity must be obeyed by any transition probability of any Markov process, the type that will be studied in this work.

1.2 Homogenous processes and the Master Equation

Among Markov processes in particular, we are interested in homogenous Markov processes whose transition probability $P_{1|1}$ only depends on the time difference between the two states of interest i.e.

$$P_{1|1}(x_2,t_2,|x_1,t_1) = T_\tau(x_2|x_1) \text{ with } \tau = t_2 - t_1. \tag{1.4}$$

We may now rewrite Eq. 1.3 as

$$T_{\tau+\tau'}(x_3|x_1) = \int \mathrm{d}x_2\, T_{\tau'}(x_3|x_2)T_\tau(x_2|x_1). \tag{1.5}$$

This relationship though simple in its derivation is not very tractable in its application to study a physical system. We instead appeal to the limit of this equation as the time intervals of interest go to zero, and write down the differential equation known as the Master equation.

In order to proceed, we must determine the functional form of T_τ in the limit that $\tau \to 0$ which is

$$T_{\tau'}(x_2|x_1) = (1-a_0\tau')\delta(x_2-x_1) + \tau' W(x_2|x_1) + \mathcal{O}(\tau'^2) \tag{1.6}$$

where $W(x_2|x_1)$ is the transition probability per unite time from x_1 to x_2 and $a_0(x_1) = \int \mathrm{d}x_2 W(x_2|x_1)$, meaning $1-a_0\tau'$ is the probability that no transition takes place during

the time interval τ'. Hence we may rewrite the Chapman-Kolmogorov Equation by using this definition for $T_{\tau'}$ for small τ' and find

$$T_{\tau+\tau'}(x_3|x_1) = [1 - a_0(x_3)\tau']T_\tau(x_3|x_1) + \tau' \int \mathrm{d}x_2 W(x_3|x_2)T_\tau(x_2|x_1) \tag{1.7}$$

Dividing by and taking the limit as τ' goes to zero yields

$$\partial_\tau T_\tau(x_3|x_1) = \int \mathrm{d}x_2 \left\{W(x_3|x_2)T_\tau(x_2|x_1) - W(x_2|x_3)T_\tau(x_3|x_1)\right\} \tag{1.8}$$

We rewrite the equation in its more simplified, intuitive form as

$$\partial_t P(x,t) = \int dx' W(x|x')P(x',t) - W(x'|x)P(x,t) \tag{1.9}$$

where we interpret the first term on the right hand side as all the possible ways one may arrive at the state x from the states x' given that we started at some arbitrary state x_0 while the second term is all the ways one leaves the state x to go to the states x' given that we started at the same arbitrary state x_0.

Note that the only assumptions that were made in the derivation of the Master equation were that we were analyzing a homogeneous, Markov process. No assumptions were made regarding the size of transitions available to the stochastic process, whether the process was at thermal equilibrium or not. Hence if one can figure out the form of the $W(x|x')$, a stochastic system may be analyzed whether it is in a state of equilibrium or not.

The Master equation will be our starting point for our analyses of lower dimensional phase spaces, amenable to exact solutions for a system out of mechanical equilibrium and a system out of thermal equilibrium which will be studied in Chapters 2 and 3. However the analysis of higher-dimensional phase spaces becomes analytically and computationally intractable, hence we need a new approach in order to study these systems. For this we appeal to a Langevin-like noise approximation, which we outline next.

1.3 Langevin-Like Noise

Although the Master equation is the most ideal point to start a study for a stochastic system outside of equilibrium due to its generality and exactness, it becomes analytically and numerically infeasible to solve the equation for large, multidimensional phase spaces

outside of the thermal equilibrium limit where Maxwell-Boltzmann statistics hold. Hence we seek a different method in order to study our stochastic system outside the thermal equilibrium limit. In order to do this we will analyze the equations of motion of two non-linear harmonic oscillators in Chapter 4 in the presence of a non-Gaussian, white noise source near a second-order phase transition.

In anticipation of this, we give a simpler version of the problem we wish to analyze by providing a simple reference system i.e. the motion of a particle in the presence of damping and random thermal forcing

$$m\dot{v} + \Gamma v = f(t) \tag{1.10}$$

where m is the mass of the particle of interest, Γ is the friction constant, v is the velocity of the particle. When this system is studied in thermal equilibrium, the force is considered to come from a Gaussian, white-noise probability distribution $P[f(t)] = \mathcal{N} \exp\left[-(2D)^{-1} \int \mathrm{d}t f^2(t)\right]$ where $\mathcal{N}$ is an uninteresting normalization constant and D is the spread of thermal forces which is proportional to the thermal energy scale, $k_B T$. This means the first two cumulants of $f(t)$ are given by $\langle f(t) \rangle = 0$ and $\langle\langle f(t) f(t') \rangle\rangle = D\,\delta(t - t')$. Given that the probability distribution for the force is Gaussian, all higher order cumulants are zero, hence the velocity-velocity correlation function in frequency space it can be solved via a simple Fourier transform to yield

$$\langle v(\omega) v(\omega') \rangle = \frac{2\pi D\,\delta(\omega + \omega')}{|-i\,m\,\omega + \Gamma|^2}.$$

This correlation functions along with the correlation functions of various combinations of the velocity field time derivatives provides a physically realizable quantity to measure to determine whether the system is at thermal equilibrium or not. If the velocity-velocity correlation function does not match the spectrum given by the correlation functions in the presence of Gaussian noise, then a new approach will be necessary in order to understand the fluctuation spectrum of the system.

The results for the velocity-velocity correlation function are well known for the stochastic statistics of systems at or near thermal equilibrium and can be related to response function of the system to yield a version of the fluctuation-dissipation theorem. However, note that these results only hold because we are assuming a Gaussian, white-noise force

profile. Once these assumptions are eliminated for the noise, there is no guarantee that the fluctuation-dissipation theorem holds anymore.

We are interested in this type of regime where our noise sources are still white (uncorrelated in time), but do not come from a Gaussian probability distribution and are interested in how these fluctuations affect a system near a phase transition through its correlation functions. For these type of systems, correlation functions for systems in the presence of non-Gaussian, white noise may have terms proportional to the now nontrivial higher order cumulants such as $\langle\langle f(t_1)f(t_2)f(t_3)f(t_4)\rangle\rangle = \Gamma_4\delta(t_1-t_2)\delta(t_1-t_3)\delta(t_1-t_4)$ where Γ_4 is a constant associated with the quartic averaging of the forces[3]. Though terms like these are irrelevant for the study of the velocity-velocity correlation function of our overdamped particle, these force averaging terms are important for higher order in power velocity correlation functions and for non-linear systems, such as the one explored in Chapter 4.

Nevertheless to illustrate the effect of non-Gaussian white noise, we solve for the four point function for our simple free particle in an overdamped dynamic to see the effect of the quartic cumulant of the forces on the four point function i.e. we give

$$\begin{aligned}\langle v(\omega)v(\omega')v(\omega'')v(\omega''')\rangle =& \frac{2\pi}{(-i\,m\,\omega+\Gamma)(-i\,m\,\omega'+\Gamma)(-i\,m\,\omega''+\Gamma)(-i\,m\,\omega'''+\Gamma)}\times \\ & \big(\Gamma_4\delta(\omega+\omega'+\omega''+\omega''') + 2\pi\Gamma_2^2\left(\delta(\omega+\omega')\delta(\omega''+\omega''')\right. \\ & \left.+\delta(\omega+\omega'')\delta(\omega'+\omega''')+\delta(\omega+\omega''')\delta(\omega'+\omega'')\right)\big)\,. \end{aligned} \tag{1.11}$$

Note the appearance now of the delta function with the sum of the four ω's having equal to zero. The effect of this term is visualized easier in the time domain, so we Fourier transform back and find the four point function in the time space to be assuming $t_4 > t_3 > t_2 > t_1$ is $\langle v(t_1)v(t_2)v(t_3)v(t_4)\rangle =$

$$\begin{aligned} & \Gamma_4\frac{\exp\left[-\frac{\Gamma}{m}(t_4-t_1)\right]\exp\left[-\frac{\Gamma}{m}(t_3-t_1)\right]\exp\left[-\frac{\Gamma}{m}(t_2-t_1)\right]}{4\,\Gamma m^3} \\ & + \frac{\Gamma_2^2}{4\Gamma^2m^2}\left(\exp\left[-\frac{\Gamma}{m}(t_4-t_1)\right]\exp\left[-\frac{\Gamma}{m}(t_3-t_2)\right]\right) \\ & + \frac{\Gamma_2^2}{4\Gamma^2m^2}\left(\exp\left[-\frac{\Gamma}{m}(t_4-t_2)\right]\exp\left[-\frac{\Gamma}{m}(t_3-t_1)\right]\right) \\ & + \frac{\Gamma_2^2}{4\Gamma^2m^2}\left(\exp\left[-\frac{\Gamma}{m}(t_4-t_3)\right]\exp\left[-\frac{\Gamma}{m}(t_2-t_1)\right]\right). \end{aligned} \tag{1.12}$$

[3]We only consider symmetric noise sources, meaning all odd powered force cumulants are zero

We see now that the non-Gaussian noise for our simple, linearized theory of a particle in an damped medium provides additional corrections to the four point function that decay exponentially in time and are proportional to Γ_4. The effect of non-Gaussian noise is hence most visible for times shorter than Γ/m and contributes significantly to the four point function in an underdamped medium i.e. when our decay correlation time, m/Γ, is small compared to other natural time scales arising in our system. This holds true even for the non-linear set of equations we will be studying in Chapter 4. We now proceed to show the effect of the non-Gaussian noise on the conditional probability statements of our stochastic system.

1.4 Fokker-Planck like equation and the equivalent Master equation

Typically during the examination systems near thermal equilibrium using a Langevin approach, a corresponding Fokker-Planck equation is written down as well by looking at the conditional probability statement of the form

$$P(v,t|v_0,t_0) = \langle \delta(v - v(t)) \rangle_{v_0,t_0} \tag{1.13}$$

which is the probability of finding the diffusing particle at velocity v at time t given that it had velocity v_0 at time t_0. The probability that the particle has velocity v at time $t + \Delta t$ is given by the sum of all paths through phase space to achieve said velocity i.e.

$$P(v,t+\Delta t|v_0,t_0) = \int \mathrm{d}v' P(v,t+\Delta t|v',t) P(v',t|v_0,t_0) \tag{1.14}$$

We may write out the conditional probability $P(v,t+\Delta t|v',t) = \langle \delta(v - v(t+\Delta t)) \rangle_{v',t}$ using the equation motion and expanding in terms proportional to Δt

$$v(t+\Delta t) = v' - \frac{\Gamma}{m} v' \Delta t + \frac{1}{m} \int_t^{t+\Delta t} \mathrm{d}t'\, f(t'). \tag{1.15}$$

Typically one only expands to $\mathcal{O}(f^2(t))$ [50] in force terms as these are the only terms proportional to Δt in the expansion of the conditional probability evaluated at $t + \Delta t$. However the introduction of the nontrivial quartic cumulants produces additional terms

now proportional to Δt of the form

$$\int_t^{t+\Delta t} \mathrm{d}t_1 \int_t^{t+\Delta t} \mathrm{d}t_2 \int_t^{t+\Delta t} \mathrm{d}t_3 \int_t^{t+\Delta t} \mathrm{d}t_4 \langle f(t_1) f(t_2) f(f_3) f(t_4) \rangle \propto \Gamma_4 \Delta t + \mathcal{O}(\Delta t^2) \tag{1.16}$$

Hence when expanding our conditional probability, we find new terms proportional to Δt that do not appear for the particle in the presence of Gaussian, white-noise forcing of the form

$$\begin{aligned} \langle \delta(v - v(t+\Delta t)) \rangle_{v',t} =& \delta(v-v') - \langle \Delta v \rangle \partial_v \delta(v-v') + \frac{\langle (\Delta v)^2 \rangle}{2!} \partial_v^2 \delta(v-v') + \\ & \frac{\langle (\Delta v)^4 \rangle}{4!} \partial_v^4 \delta(v-v') + \mathcal{O}(\langle (\Delta v)^6 \rangle). \end{aligned} \tag{1.17}$$

Note that this summation continues *ad infinitum* in even powers of $\Delta v = v(t+\Delta t) - v'$, meaning that there is an equivalent Master equation that to match the Fokker-Planck like equation if one performs the appropriate Kramers-Moyal expansion.

Thus we see that with non-Gaussian, white noise, we may capture the behavior of a stochastic system which requires a full Master equation description while appealing only to the equations of motion. This ability to look at the stochastic equations of motions allows us to explore higher dimensional phase spaces of stochastic systems in an analatically tractactable way as we will explore in Chapter 4.

1.5 Outline of the text

Our analysis of stochastic systems outside of equilibrium will proceed as follows. In Chapter 2, we will explore the effect of a probe particle under a constant, applied force field on the stochastic bond-breaking dynamics of a highly cross-linked microtubule network. This system is out of mechanical equilibrium with its surroundings at a single temperature. We will write down and solve a Master equation for the state of unbinding for a single filament in the network and relate measurements of the probe particle's movement to the underlying microscopic, stochastic unbinding of single cross-linkers from a single filament.

In Chapter 3, we will explore the dynamics of a single ion trapped in a time-dependent harmonic potential colliding with two non-interacting buffer gasses at different temperatures. The cause of the stochastic system being out of equilibrium in this particular case

is the two buffer gasses not being able to equilibrate on a sufficiently fast time scale to a single temperature due to their small collision cross-section, allowing us to treat the gasses as noninteracting except for their collisions with the trapped ion. We will write down and solve the Master equation for the position and velocity distribution of the ion and discuss some of the striking features associated with the steady-state properties of the ions' position-velocity distribution.

Chapter 4 will consist of examining the correlation function of the vibrational modes of two particles harmonically coupled to each other in the presence of stochastic forces. The cause of the stochastic system being out of equilibrium here is that there are two types of stochastic forces acting upon the system, one will be a Gaussian, white noise force, that at steady state, reproduces Maxwell-Boltzmann statistics. The other type of noise will be non-Gaussian as described above. We will write down and solve the equations of motion perturbatively for the vibrational modes of the system in the presence of these two noise sources and use these solutions to calculate the correlation functions for the system after an averaging over the noise near a second order phase transition. We will find that near this second order phase transition that the system responds to the Gaussian and non-Gaussian contributions to the noise differently, leading to different contributions to the correlation function that differ by orders in magnitude.

We will conclude with a an overview of the unifying themes surrounding the study of these stochastic systems. We will discuss a general methodology to study these systems that should be applicable to nearly all systems outside of equilibrium. Finally we suggest future systems far from equilibrium for future study.

CHAPTER 2

Single Filament Dissociation

2.1 Introduction

The first system that we will be studying will involve the dissociation dynamics of a semi-flexible filament embedded in highly-crosslinked semi-flexible filament network. The filament is out of mechanical equilibrium with its surroundings due to contact with a probe particle under a constant force. Given the large separation in time scales between the time of dissociation of cross-linkers and the relaxation dynamics of the filament after a cross-linker unbinding, we are able to write down a Master equation for the state of dissociation of the given filament. We begin our discussion with experimental motivations.

2.1.1 Motivation

Semiflexible networks are materials composed of stiff filaments cross-linked densely on the scale of their own thermal persistence length. As such, the constituent filaments can support stress via bending as well as stretching. The study of such semiflexible gels has been inspired by their importance in cellular mechanics, where the semiflexible network of the cytoskeleton confers mechanical rigidity and is the source of force generation in eukaryotic cells. These studies have yielded a rich phenomenology including nonaffine deformation [39, 81, 79], continuous, zero-temperature phase transitions [11, 27, 78], complex nonlinear elasticity [70, 54, 46, 10], and the active mechanics of motor-driven networks [59, 57, 53, 72, 75, 6].

Understanding the collective mechanical response of such networks has implications for the dynamics [29] and mechanobiology of cells [33, 3, 34], but also offers new insights into fundamental mechanical properties of this special class of polymer gels – fiber networks rather than flexible (Gaussian coil) polymer gels. One feature of these networks re-

ceiving renewed attention is the role of cross-linker mechanics in the collective response of the network. These include exploring the mechanical effect of flexible cross-linkers [9, 43], cross-linker protein domain unfolding [25, 26], and cross-linker unbinding [54, 55, 40]. The latter effect is particularly interesting as this allows for structural rearrangements on long time scales either as the network approaches thermal equilibrium [20] or in the response to applied loads [83, 61].

Previous work [83] on the motion of a bead (with a radius much larger than the mesh size of the network) show that there is a regime of creep in which the bead moves with constant velocity v in response to a constant applied force F. Energy dissipation in the network results primarily from bond breaking as can be inferred from the observed force-velocity relation, $\log(v) \sim F$, consistent with a Bell model for ligand unbinding rates [4]. In spite of this bond breaking, the modulus of the network remains essentially unchanged. One infers that bond breaking and reformation occur at equal rates in the loaded network. Closer examination of the beads' trajectories reveals many small stochastic hops on the scale of tens of nanometers, suggesting that one can indeed resolve individual bond breaking events within the large-scale drift of the bead under load.

In this chapter, we explore a single filament model for such bond breaking events, which we use to understand a few fundamental features of the dissipative dynamics in the constant velocity regime. In order to apply our results to cross-linked microtubule networks, which is the system of experimental interest, we ignore entropic effects. This very stiff network is effective a zero temperature system; as such our analysis should apply equally well to a variety of fiber networks and fiber-reenforced composites. We examine the spatial distribution of mechanical loading of the many non-covalent cross-linking bonds between filaments and develop a statistical model for the bond breaking dynamics. Using this model we reexamine the apparently uniform motion of the bead, which can be resolved into a series of microscale jumps, and conclude that these dynamics are consistent with the bond-breaking of just the highly loaded cross-linkers in the immediate vicinity of the bead. This bond breaking is consistent with a picture of bond breaking occurring on many different filaments rather than sequential breaking of bonds along a single filament. The network remodels with many independent events occurring on many filaments rather than in the peeling away of any one filament in particular. We conclude this chapter with

a discussion of further experimental tests of this emerging understanding of the network's failure and a few speculations on the appearance of cross-linker unbinding deformation in such transiently cross-linked fiber networks.

2.2 Single Filament Model

We begin with a single filament model. As shown in Fig. 2.2.1a, the filament in question (shown as a dashed line) is being deflected by the bead (large sphere); it is also bound to the network (solid lines) by a random set of cross-linkers (small spheres). In our single filament analysis we replace the entire network by an array of posts along the $\hat{z}$ axis to which the single filament is bound – see Fig. 2.2.1*b*. The bead is replaced by point loading at the origin of the coordinate system. Here we control either the load or the displacement. If the bead filament interaction allows for slip, it may generate only perpendicular forces; sticky beads may also apply longitudinal forces along the filament leading to tension. We consider both cases below, but begin with the more simple case of slip boundary conditions and perpendicular loading of the filament.

We assume that bond breaking, when it occurs, is instantaneous and that the time between bond breaking events is long compared to the relaxation time of filaments, so that filament evolves from one static mechanical equilibrium configuration to the next upon each bond breaking event. To understand the loading of these bonds in static equilibrium, we must first determine the forces on the cross-linkers for a semiflexible filament linked to a spatially random set of cross-linkers. We derive the equations of equilibrium in Appendix 2.4.

Taking the undeformed state of the filament to be straight and $\zeta(z)$ to be the perpendicular displacement of the filament in response to the applied force F acting at the origin, we write the elastic free energy $\mathcal{F}$ of the filament under uniform tension τ as [49]

$$\mathcal{F} = \int_{L_c} dz \left[\frac{\kappa}{2} \left(\partial_z^2 \zeta(z) \right)^2 + \frac{\tau}{2} \left(\partial_z \zeta(z) \right)^2 + \right. \\ \left. + \frac{V(z)}{2} \left(\zeta(z) \right)^2 - F\, \delta(z)\, \zeta(z) \right]. \tag{2.1}$$

Here κ is the bending rigidity of the filament, which is related to the filament's elastic moduli and cross sectional geometry in the usual way [49]. The function $V(z)$ represents

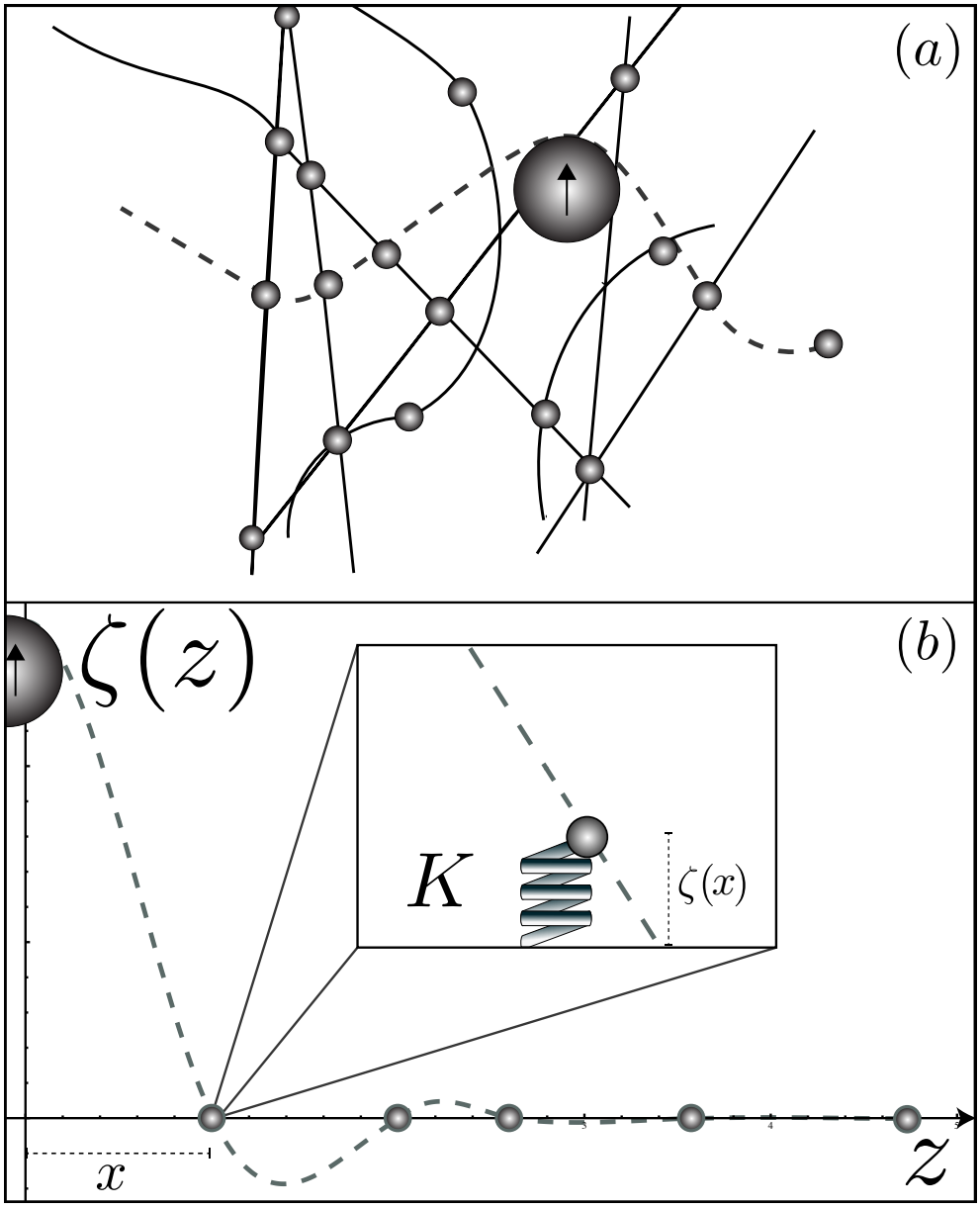

Figure 2.2.1: (a) A single filament of interest (dashed line) embedded in a cross-linked filament network (solid lines) being deformed by a force F transmitted by the probe particle (large shaded circle). (b) The deflection $\zeta(z)$ of that same filament in a two-dimensional, single filament model, where the undeformed (straight) filament is bound to a random array of cross-linkers along the $\hat{z}$-axis. x is the position of the nearest cross-linker to the applied force.

the harmonic interaction of filament with the cross-linkers and the rest of the network. We take this to be

$$V(z) = K \sum_i \delta(z - z_i), \tag{2.2}$$

where the set of linker locations $\{z_i | i = 1, \ldots, N\}$ are quenched stochastic variables chosen so that there is a Poisson distribution of lengths between adjacent linkers – see Ref. [39] for details – with mean length $\bar{\ell}$ between consecutive cross-linkers. The elastic compliance K^{-1} of the linkers is meant to reflect the combined compliance of the linking molecules and the filament network in which they are embedded. The latter compliance dominates the former so that $K \sim 6\pi G_0 a$, where G_0 is the plateau modulus of the network and a a size characteristic of the bond to network connection. Taking $a \sim 10^{-9}$m and gel moduli in the kPa or softer range, we find $K \sim 10^2 \mathrm{pN}/\mu\mathrm{m}$.

Minimization of Eq. 2.1 with respect to the deflection field yields the condition for force balance obeyed by the filament in between bond breaking events

$$\kappa\, \partial_z^4 \zeta(z) - \tau\, \partial_z^2 \zeta(z) + V(z)\zeta(z) = F\, \delta(z). \tag{2.3}$$

From this equation and the mean length between consecutive cross-linkers, one obtains two fundamental length scales – the potential length ℓ_p and the bending length ℓ_κ defined respectively to be

$$\ell_p = \left(\frac{144\, \kappa\, \bar{\ell}}{K} \right)^{1/4}; \quad \ell_\kappa = \left(\frac{\kappa}{\tau} \right)^{1/2}. \tag{2.4}$$

The potential length is a measure of how far the deflection field of the filament due to the applied point force penetrates past the first unbroken cross-linker. As one might expect, this penetration depth grows with the elastic compliance of linkers K^{-1} and with the bending modulus of the filament[1].

The bending length measures the relative importance of bending and tension in the force balance relation. Forces associated with filament bending are related to higher derivatives of the filament configuration, and thus always dominate at sufficiently short distances. At distances greater than the bending length ℓ_κ, tension rather than bending plays the dominant role in the force balance relation, Eq. 2.3. At those length scales, the mechanics of the filament is more analogous to that of a taut string. We will see

[1]The numerical prefactor 144 is included to simplify later calculations.

that for distances small compared to the bending length ℓ_κ the stiff filament acts like a lever, leading to an acceleration of the rate of subsequent unbinding events, as described in Section 2.2.2-see Fig. 2.2.4 inset.

Our analysis proceeds as follows. First we calculate all of the forces on the cross-linkers by solving Eq. 2.3 for states of mechanical equilibrium either with prescribed displacement or force at the origin. Using the calculated forces on the cross-linkers, we calculate the dissociation rates of the cross-linkers. We note that, due to the exponential dependence of the linker unbinding rate on force and the exponential decrease of the loading on the cross-linker with distance from the point of force application, it reasonable to assume that linkers break in sequence – the surviving linker currently nearest the point of force application is overwhelming most likely to break next. Using this observation, we make the *sequential unbinding approximation* and then compute the dynamics of filament unbinding. We then turn to the experiments. For the reader's convenience we provide a complete list of variables used in Table 2.1.

2.2.1 States of mechanical equilibrium

The solution of the mechanical equilibrium of the filament is facilitated by a transfer matrix approach. In the intervals of length $\ell_{i+1} = z_{i+1} - z_i$ between consecutive cross-linkers, we solve Eq. 2.3 with a shifted independent variable:

$$y_i = z - \sum_{q=0}^{i} z_q, \tag{2.5}$$

where we define $z_0 = 0$. In this way the deflection field $\zeta_i(y_i)$ between the i^{th} and $(i+1)^{\text{th}}$ linker is simply given by

$$\zeta_i(z) = \zeta_i^{(0)} + \zeta_i^{(1)}\, y_i + \zeta_i^{(2)}\, \ell_\kappa^2 \left[\cosh \frac{y_i}{\ell_\kappa} - 1\right] \tag{2.6}$$

$$+ \zeta_i^{(3)}\, \ell_\kappa^3 \left[\sinh \frac{y_i}{\ell_\kappa} - \frac{y_i}{\ell_\kappa}\right], \tag{2.7}$$

in terms of the (as yet unknown) boundary conditions: $\zeta_i^{(n)}$, $n = 0, \ldots, 3$ representing the displacement $\zeta_i^{(0)}$ at the i^{th} linker and its first three derivatives. In the limit of no tension, Eq. 2.7 becomes

$$\zeta_i(z) = \zeta_i^{(0)} + \zeta_i^{(1)}\, y_i + \zeta_i^{(2)}\, \frac{y_i^2}{2!} + \zeta_i^{(3)} \frac{y_i^3}{3!}, \tag{2.8}$$

Table 2.1: List of variables. Dimensions: $[L]$ =Length, $[t]$ =time, and $[F]$ =Force.

Symbol	Dimensions	Description
z	$[L]$	Position along contour length of undeformed filament
z_i	$[L]$	Position of i^{th} cross-linker down filament's undeformed contour length, L_c
$\ell_i = z_i - z_{i-1}$	$[L]$	Distance between i^{th} and $(i-1)^{\text{th}}$ cross-linker
x	$[L]$	Distance to nearest unbroken cross-linker from applied force, F
$\zeta(z)$	$[L]$	Deflection field of filament perpendicular to undeformed configuration
ζ_i	$\{[L],1,[L]^{-1},[L]^{-2}\}$	Vector of derivatives of the deflection field at i^{th} cross-linker
κ	$[F][L]^2$	Bending modulus of filament
τ	$[F]$	Applied tension on filament
K^{-1}	$[L]\ [F]^{-1}$	Elastic compliance of cross-linkers
ℓ_p	$[L]$	Potential length
ℓ_κ	$[L]$	Bending length
$\bar{\ell}$	$[L]$	Mean distance between cross-linkers
F	$[F]$	Applied force
$T(\ell_i)$	Multiple dimensions	Transfer matrix (see appendix for dimensions of elements)
k	$[t]^{-1}$	Bell model dissociation rate (base rate of cross-linker dissociation)
k_0	$[t]^{-1}$	Base rate of cross-linker dissociation
F_0	$[F]$	Thermal force scale
$\mathcal{T}$	$[t]$	Total time of dissociation of a filament from cross-linker density
$P_m(t)$	1	Probability that m cross-linkers have dissociated by time t
$v_\perp(x)$	$[L]\ [t]^{-1}$	Normal velocity of point of loading for a cross-linker at x
$\mathcal{P}_N(n)$	1	Probability of n sequential peeling events occurring over one mean dissociation time τ on a filament bound to N cross-linkers

as is clear from taking the appropriate limit of Eq. 2.7. In both cases, the solution is written in terms of the four unknown parameters.

Since the filament must be continuous and have continuous first and second derivatives, knowing the solution for the filament in the i^{th} segment $\ell_i = z_i - z_{i-1}$ provides these three boundary conditions for the solution of the filament trajectory in the next segment $\ell_{i+1} = z_{i+1} - z_i$. Integration of Eq. 2.3 across z_i yields the discontinuity in $\zeta'''(z)$, which is determined by the harmonic force provided by that linker: $\zeta_i'''(0) - \zeta_{i-1}'''(\ell_i) = -\frac{K}{\kappa}\,\zeta_{i-1}(\ell_i)$.

Imposing these boundary conditions across the i^{th} cross-linker amounts to solving a linear system of equations for $\zeta_{i+1}^{(n)}$ in terms of the analogous information at the previous cross-linker $\zeta_i^{(n)}$. Thus, the effect of the solution of the differential equation for the filament trajectory between cross-linkers is to propagate that boundary condition information forward via a linear transformation, which may be described in terms of a transfer matrix

$$\zeta_{i+1} = T(\ell_i)\,\zeta_i, \tag{2.9}$$

where $\zeta_i = \{\zeta_i^{(0)}, \zeta_i^{(1)}, \zeta_i^{(2)}, \zeta_i^{(3)}\}$. The full transfer matrix is readily computed from the solutions given in Eqs. 2.7,2.8 for the cases of finite and zero tension respectively. The matrix is shown in Appendix A.

Iteration of the transfer matrix on the vector representing the state of the filament at the point of force application yields the state of the filament at an arbitrary cross-linker: ζ_n: $\zeta_n = [T(\ell_n)T(\ell_{n-1})\ldots T(\ell_1)]\,\zeta_0$. The differential equation solutions then give the correct form of the filament's trajectory in force balance in between these site. However, since our interest is solely in the forces at the linkers, the full filament trajectory information is unnecessary.

It remains to determine the initial boundary condition vector ζ_0 at the site of force application. We choose to apply a point force F and we require a zero tangent condition: $\zeta_0^{(1)} = 0$, i.e, a "clamped" boundary condition. Of course, there are two other boundary conditions needed to determine the initial value of the vector ζ_0, as is expected for the fourth order differential equation Eq. 2.3. We must specify these at the other end of the filament. There are two classes of problems that one may address. For finite length filaments, we may require the far end to be both force and torque free. For infinite

length filaments, we will assume that the filament and its local slope both approach zero: $\zeta_i^{(0,1)} \to 0$ for $i \to \infty$. Both cases are discussed further below.

2.2.2 An infinite filament interacting with a lattice of linking sites

The simplest solution is obtained for the case of an infinite filament with an ordered lattice of binding sites. In this case $\bar{\ell} = z_{i+1} - z_i$ for all i and the product of transfer matrices necessary for the solution becomes simply the n^{th} power of one transfer matrix. This problem is best addressed by working in the eigenbasis of the transfer matrix. There are four complex eigenvalues λ_i, which are the roots of the polynomial

$$\lambda_i^4 + 1 - (\lambda_i^3 + \lambda_i)(2 + 2\cosh\gamma + 144\,\frac{\alpha}{\gamma^2} - 144\,\frac{\alpha}{\gamma^3}\sinh\gamma) \tag{2.10}$$

$$+2\,\lambda_i^2(1 + 2\cosh\gamma + 144\,\frac{\alpha}{\gamma^2}\cosh\gamma - 144\,\frac{\alpha}{\gamma^3}\sinh\gamma) = 0. \tag{2.11}$$

These roots are functions of two dimensionless control parameters: $\alpha = \left(\bar{\ell}/\ell_p\right)^4$ and $\gamma = \bar{\ell}/\ell_\kappa$. The first measures the (fixed) distance between binding sites in terms of the potential length. The second compares the same inter-binding site distance to the bending length.

In Fig. 2.2.2a we plot the logarithm of the modulus of these four eigenvalues $\lambda_i = \lambda_i(\alpha, \gamma)$ as a function of α for fixed $\gamma = 5$. This plot shows a number of generic features that characterize all solutions. Two of the four eigenvalues have a modulus greater than one and two less than one; this point will be essential when studying the infinite filament solutions below. For any nonzero value of γ (i.e., for finite tension in the filament) there are three classes of roots $\lambda_i = \lambda_i(\alpha, \gamma)$. For sufficiently small α, one finds the *high tension regime* where there are four distinct real eigenvalues, shown in the figure as dashed lines. The subspace spanned by the eigenvectors with eigenvalues having magnitudes less than one span the set of all monotonically decaying displacement field solutions. In this limit where the tension is high and the linker compliance is also large, the relaxation of the filament back to the axis containing the linkers is generically a double exponential decay. A typical solution is shown by the dashed line in Fig. 2.2.2b.

For larger α, one encounters the *incommensurate regime* where the eigenvalues come in two complex conjugate pairs. These four solutions are represented by the solid lines in Fig. 2.2.2a (the complex conjugate pairs necessarily have the same modulus). The

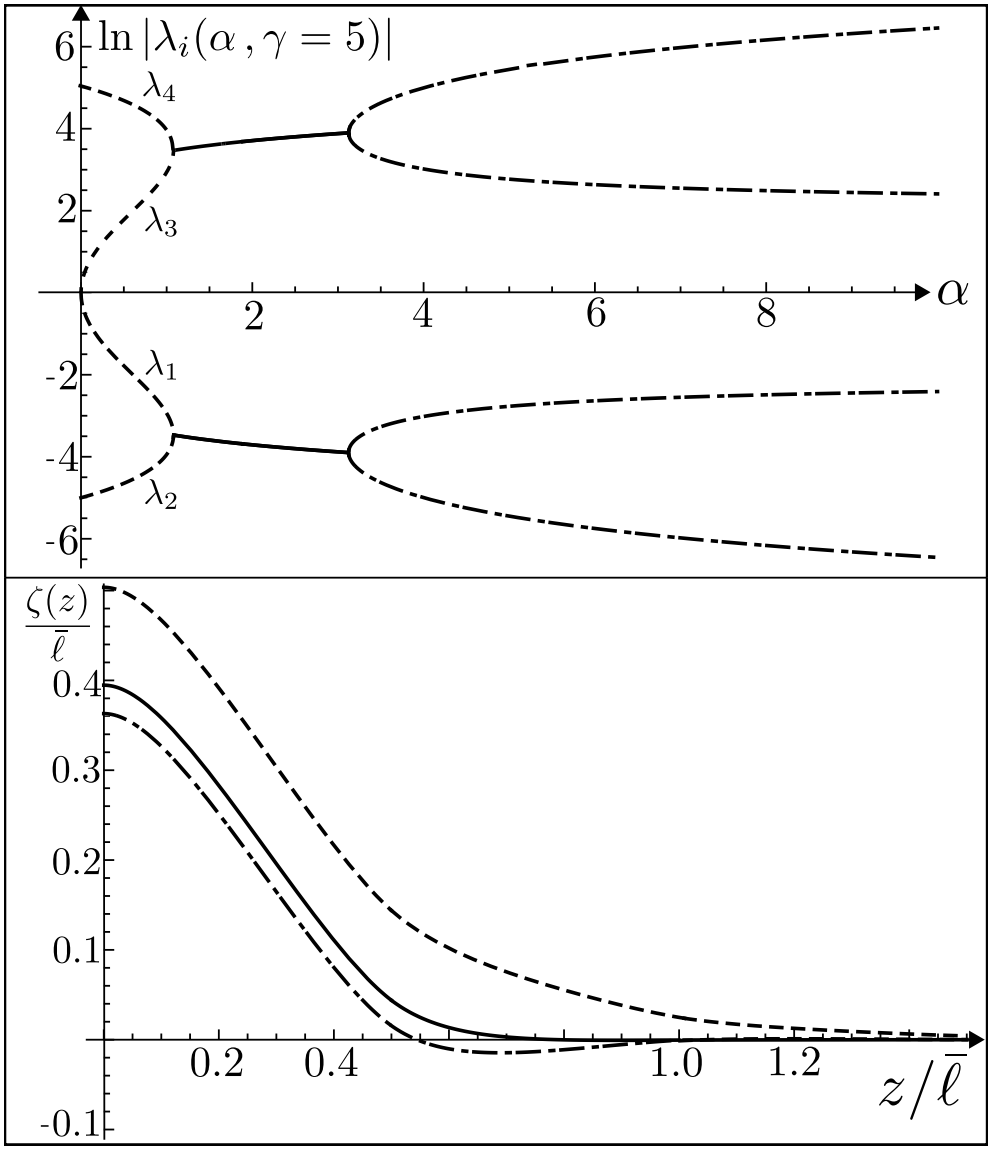

Figure 2.2.2: (Top) The log of the modulus of the four eigenvalues as a function for α for a tensed filament: $\gamma = 5$ showing the high tension, incommensurate, and lock-in regimes, as described in the text. (Bottom) Typical filament deflections for a filament of infinite length interacting with a a lattice of linker sites in the high tension (dashed), incommensurate (solid) and lock-in (dash-dotted) regimes.

subspace spanned by the decaying solutions (corresponding to eigenvalues with modulus less than unity) takes the form $\zeta_n \sim \exp(-kn)\cos(n\phi)$. The filament's displacement decays exponentially but overshoots the linkers positions. Since the phase angle ϕ is generically not a rational fraction of 2π, the periodicity of the height field at the linkers is typically incommensurate with the linker lattice – a solution of this type is shown by the dash-dotted line in Fig. 2.2.2b. For even larger α corresponding to more incompliant linkers, these incommensurate undulations lock-in with the lattice leading to a form $\zeta_n \sim \exp(-kn)\cos(n\pi)$. A typical solution of this form is shown by the solid line in Fig. 2.2.2b. For zero tension, the transition from incommensurate to commensurate filament undulations remains, but the high tension region vanishes.

We first consider the case of infinitely long filaments. Finite length effects are addressed in the next section. The known applied force at the origin and the clamped (zero slope) boundary condition determine two of the four unknown coefficients $\zeta_0 = \left\{\zeta_0^{(0)}, 0, \zeta_0^{(2)}, -F/\kappa\right\}$. To solve the filament trajectory and, from that, the loading on each of the linkers for an infinite filament one must work in the subspace spanned by the eigenvectors $\mathbf{w}_{1,2}$ corresponding to the small modulus ($|\lambda_{1,2}| < 1$) eigenvalues in order to obtain decaying solutions. We expand the solution in terms of two unknown coefficients $\zeta_0 = b_1\mathbf{w}_1 + b_2\mathbf{w}_2$. These are given by

$$b_1 = \frac{F}{\kappa}\frac{(\lambda_1 - 1)(\lambda_2 + 1)(\lambda_1 - \cosh\gamma)}{(\lambda_1 - \lambda_2)(\lambda_1\lambda_2 + \lambda_1 + \lambda_2 - 2\cosh\gamma - 1)} \tag{2.12}$$

$$b_2 = \frac{F}{\kappa}\frac{(\lambda_2 - 1)(\lambda_1 + 1)(\lambda_2 - \cosh\gamma)}{(\lambda_2 - \lambda_1)(\lambda_1\lambda_2 + \lambda_1 + \lambda_2 - 2\cosh\gamma - 1)}. \tag{2.13}$$

Recalling that each linker is a Hookean spring, it is simple to obtain the force on each linker: the force on the i^{th} linker F_i is simply linear in the deflection at that point and proportional to the spring constant

$$F_i = K\left(b_1\,\lambda_1^i\,w_1^0 + b_2\,\lambda_2^i\,w_2^0\right) \tag{2.14}$$

where w_i^0 is the first component of the i^{th} eigenvector corresponding to $\zeta^{(0)}$, the deflection field.

In order to follow the dynamics of bond breaking, one needs to know how these forces are redistributed after each linker dissociation event. Anticipating the sequential

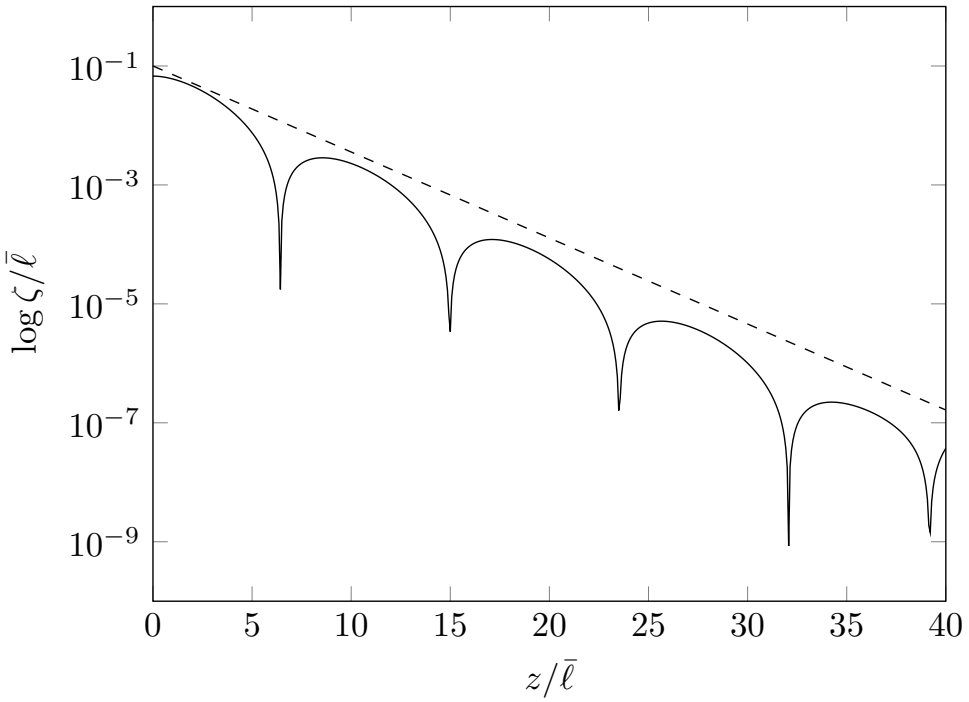

Figure 2.2.3: Absolute value of the deflection of an infinite semiflexible filament interacting with a lattice of binding sites in the locked-in regime showing oscillations and an exponential envelope (dashed line).

breaking assumption (to be justified by the exponential decay of forces along the filament) we focus on the case in which the first p cross-linkers have failed. To take into account the load redistribution after p cross-linkers have been dissociated, we replace the first $(p+1)$ transfer matrices in the product by one with an increased inter-linker distance. The solution for the filament trajectory at the surviving linker sites $n > p+1$ is then given by ζ_n with

$$\zeta_n = T[\bar{\ell}]^{\,n-(p+1)}\, T\left[(p+1)\,\bar{\ell}\right]\, \zeta_0. \tag{2.15}$$

The analysis now proceeds along the same lines, but the state vector of the filament after the first unbroken cross-linker must remain in the subspace spanned by the two decaying modes. Thus, the boundary conditions at the point of force application are chosen to give $T\left[(p+1)\,\bar{\ell}\right]\zeta_0 = b_1\mathbf{w}_1 + b_2\mathbf{w}_2$.

We show in Fig. 2.2.3 the absolute value of the deflection field for an infinite semiflexible filament interacting with a lattice linker sites before any bond dissociations. Parameters are chosen so that the filament is in the locked-in regime – see Fig. 2.2.2b. The semilog plot demonstrates the exponential decay of the envelope of oscillations the deflec-

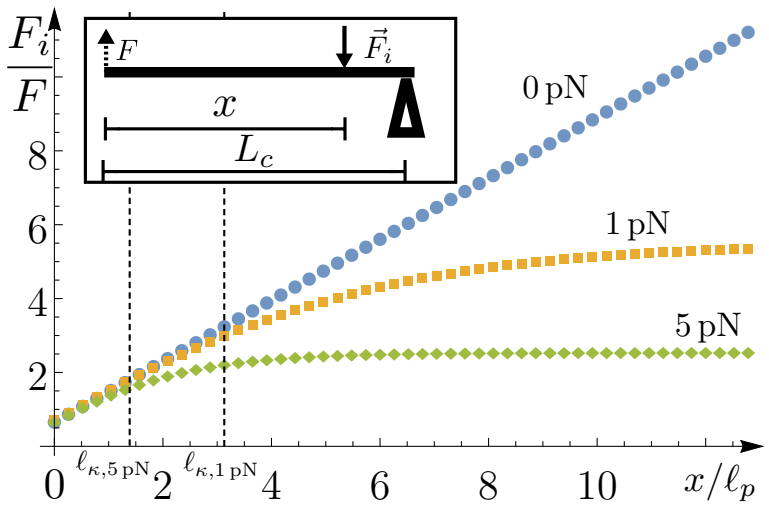

Figure 2.2.4: Force on the first unbroken cross-linker after i cross-linkers have already broken in the linker lattice. The lever arm effect provides increasing mechanical advantage for subsequent linker peeling over distances ℓ_κ. x is the distance to the nearest cross-linker to the applied force, F. Inset: Diagram of the "class two" lever where the load (cross-linker force, F_i) lies between the effort (applied force, F) and the fulcrum (the remaining cross-linkers not undergoing dissociation).

tion amplitude (dotted line). As consequence, the cross-linker loading is largest on the first unbroken linker. In fact, for a total force F, the load on the first linker is typically greater than the applied force $\sim 2F$. This and Bell model for cross-linker disassociation rates justifies our sequential unbinding approximation for the dynamics – see Sec. 2.3.

Given the sequential breaking assumption, one must determine the load on the first unbroken linker after the first p linkers have already been broken. This is straightforward using Eq. 2.15 and the harmonic linker potential to convert the deflection to a force. We plot the result in Fig. 2.2.4. For $\tau = 0$, there is a linear increase in the force due to a lever arm effect [37, 5].

The array of unbroken cross-linkers provides the fulcrum of the lever, and the lever arm is the section of the filament that has already undergone cross-linker dissociation – see inset. Subsequent breaking events increase the lever arm and the mechanical advantage of the load, suggesting that peeling dynamics should accelerate. Finite tension $\tau > 0$ cuts off this growth at $\sim \ell_\kappa$.

2.2.3 Finite length corrections

We now examine the forces on the finite contour length filament for an ordered array of cross-linkers. We take the end of the filament to be force and torque free, setting $\zeta_N = \{\zeta_N^{(0)}, \zeta_N^{(1)}, 0, 0\}$ at the end of the filament so that there are two boundary conditions to be satisfied on each end of the filament. We recapitulate the transfer matrix solution for the finite filament with p broken linkers using Eq. 2.15 and solving for the four unknown constants, $x = \{\zeta_0^{(0)}, \zeta_0^{(2)}, \zeta_N^{(0)}, \zeta_N^{(1)}\}$. Solving this linear system of equations can be done as follows. Writing the matrix $M = T^{N-(p+1)}\left[\bar{\ell}\right] T\left[(p+1)\bar{\ell}\right]$ in terms of the column vectors $(\vec{m}_1, \vec{m}_2, \vec{m}_3, \vec{m}_4)$, and introducing unit column vectors in the 1 and 2 directions, $\hat{e}_{1,2}$ respectively, one may write linear system of equations in the form

$$\zeta_0^{(0)}\vec{m}_1 + \zeta_0^{(2)}\vec{m}_3 - \zeta_N^{(0)}\hat{e}_1 - \zeta_N^{(1)}\hat{e}_2 = -\frac{F}{\kappa}\vec{m}_4, \tag{2.16}$$

which may be inverted to obtain the four undetermined coefficients. To briefly summarize, we find that for ordered arrays of linkers, the effect of finite length becomes significant only in a region of length $\sim \ell_p$ near the ends, assuming that the filament is at least of order ℓ_p. For disordered arrays of the linkers, it appears that the infinite length filament approximation also remains valid for some region at least a few ℓ_p away from the ends.

2.2.4 Random arrays of linkers

In a random isotropic network, one expects that the distribution of distances between consecutive cross-linkers to be random with a Poisson distribution. Specifically, given a mean distance $\bar{\ell}$ between cross-linkers, the probability of finding a distance between consecutive linkers between z and $z + dz$ is $P(z)dz = \exp\left[-z/\bar{\ell}\right]/\bar{\ell}\ dz$. This implies that there will be exponentially rare long gaps, i.e., much larger than the mean spacing, between cross-linkers. Understanding the effect of such quenched random linker positions on the unpeeling process is important for assessing the implications of the simple lattice model for more physical random filament networks.

To explore this issue, we generated an ensemble randomly pinned filaments using products of transfer matrices $\Pi_{i=1}^{N} T(\ell_i)$, with the distance between the cross-linkers, ℓ_i, selected from a Poisson distribution in place of the simple product of identical transfer matrices used in Eq. 2.15. For all simulations discussed below, the following values of

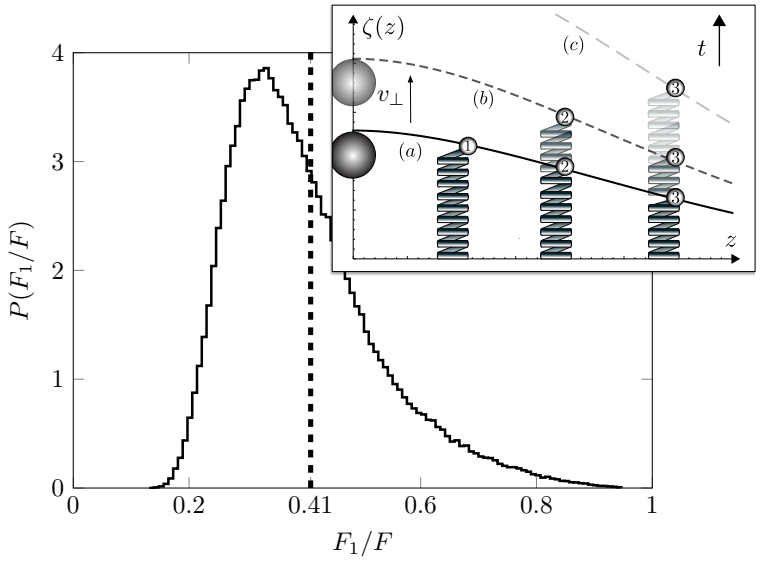

Figure 2.2.5: Distribution of loading on the first unbroken linker for Poisson distributed cross-linkers on a single filament. The equivalent loading for a regular linker array with the same inter-linker mean spacing is shown as the dashed line. Inset: Schematic of sequential peeling showing filament after zero (a), one (b), and two (c) linker rupture events.

material parameters of the semiflexible filament were used: (when applicable) $\tau = 5\,\mathrm{pN}$ and $K = 100\,\mathrm{pN}/\mu\mathrm{m}$. The results are summarized in Fig. 2.2.5, where we see that the distribution of loading on the first unbroken cross-linker in the disordered case (solid line) lies mostly to the left of that force for the linker lattice having the same mean spacing as the disordered array. The preponderance of these lower forces leads to generically slower peeling dynamics in disordered linker arrays as compared to regular ones at the same mean linker density. We directly observe this effect in the calculation of the dynamics – see Fig. 2.3.2.

2.3 Peeling dynamics

Having examined the problem of mechanical equilibrium, we turn to the question of forced peeling dynamics of a single filament from an array of linkers. The disassociation of non-covalent bonds are generally well-understood in terms of the Bell model [4], which postulates that the unbinding rate k is exponentially sensitive to force applied to that

bond

$$k(F) = k_0 e^{F/F_0}, \tag{2.17}$$

where both the zero force off-rate and the force scale F_0 depend on microscopic parameters specific to the linker in question. For biotin avidin bonds the force scale is $F_0 \sim 30$ pN [83] Subsequently, much work has been done on the effect of the loading rate on the mean force [28] of rupture in force-ramp experiments. We expect that loading to be rapid compared to the

mean time to failure for a bond, and neglect the dependence on loading rate. The stochastic nature of the unbinding process implies that, although the linker loading is deterministic, the peeling dynamics are always stochastic. It is essential to distinguish between the two different types of random variables in this problem: the stochastic dynamics associated with the unbinding of a given linker and the quenched random distribution of linker positions along a filament.

Based on the exponential dependence of the unbinding rate upon load – see Eq. 2.17 – and exponential decay of the bond loading on subsequent linkers moving down the filament from the point of loading – see Fig. 2.2.3 – the first unbroken linker is always significantly more likely to break than any of the others. Based on this, we introduce the sequential unbinding approximation in which we consider a special (but dramatically more probably) sequence of breaking events in which only first unbroken linker fails. This limits our analysis to a particular subclass of stochastic trajectories of the filament under loading and greatly simplifies the analysis. A schematic of the allowed unpeeling trajectories is shown in in the inset of Fig. 2.2.5 in which we define $v_\perp$, the velocity of the point of loading normal to the initial direction of the undeformed filament.

Given the force-dependent bond rupture rate, it is a simple matter to write the bond survival probability [67, 45] at time t after having been loaded with force F at $t = 0$: $p(t) = \exp\left[-k(F)\, t\right]$. To study the stochastic dynamics of the unpeeling process, we need to calculate the probability that the m^{th} cross-linker breaks in an infinitesimal interval of time dt at time t after initially loading the filament at the origin.

To determine this we must integrate over all allowed (i.e., sequential) breaking trajectories. In other words, each of the N bonds ruptures in turn, causing the filament

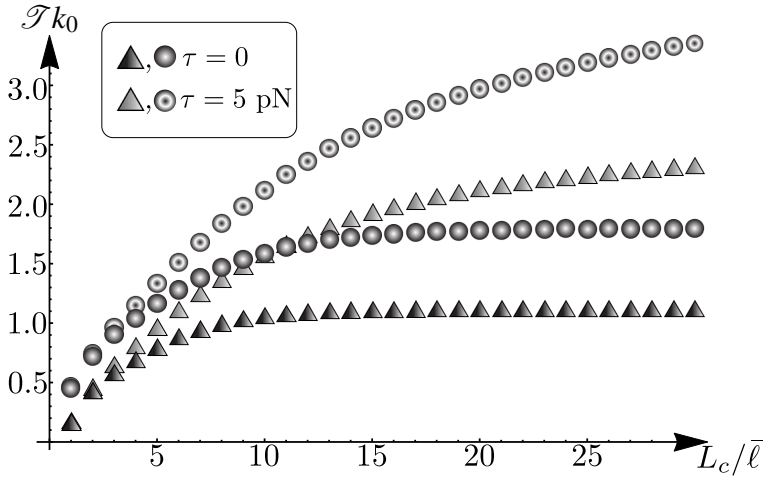

Figure 2.3.1: $\mathcal{T}$ as a function of filament length L_c for a regular lattice (triangles) and Poisson distribution (circle) of cross-linkers-see Eq. 2.22. Distances are measured in mean linker spacings $\bar{\ell}$. In the tensionless cases (filled symbols) the lever-arm effect accelerates peeling. In all cases, disorder slows the mean peeling rate, due to "trapping regions" having anomalously high linker density.

to redistribute the load on the surviving bonds. From this series of stochastic events, one may define the survival probability of the m^{th} bond at a time t after the filament is initially loaded at the origin, $P_m(t)$. This may be written as a integral over all intervals of time t_k between the rupture of bonds $k-1$ and k for the first $k = 1, \ldots m-1$ bonds. These bonds must break before the m^{th} bond, which is next to break (assuming sequential breaking). The sum of these intervals and time that the m^{th} bond has survived as the next to break must add to the total time t. The integral is given by

$$P_m(t) = \int_0^t dt_m \int_0^{t_m} dt_{m-1} \ldots \int_0^{t_2} dt_1 \exp\left[-k_1\, t_1\right] k_1 \times \\ \exp\left[-k_2(t_2 - t_1)\right] k_2 \ldots k_m \exp\left[-k_{m+1}(t - t_m)\right], \tag{2.18}$$

where the breaking rates $k_1, \ldots, k_{m+1}$ are determined by the solution of the mechanics problems previously discussed. The evaluation of those rates lies at the heart of the calculation.

Assuming those rates are known, the evaluation of the integral is straightforward:

$$P_m(t) = (-1)^m \left(\prod_{i=1}^{m} k_i\right) \left(\sum_{q=1}^{m+1} \frac{\exp\left[-k_q\, t\right]}{Y(q,m)}\right);$$

where

$$Y(q,m) = \prod_{j\neq q}^{j\leq m+1} (k_q - k_j). \tag{2.19}$$

Taking the time derivative of $P_m(t)$ in Eq. 2.18, one may obtain a recursive set of differential equations for the various bond-breaking probabilities. These have a simple interpretation, which is discussed in appendix B.

The probability for bond m to break is the negative derivative that bond's survival probability [45]

$$f_m(t) = -\frac{d}{dt}\left(\sum_{q=0}^{m} P_q(t)\right) = k_{m+1}P_m(t). \tag{2.20}$$

From this we compute the quantity of primary interest: the mean time for the rupture of the m^{th} linker along the filament. This mean τ_m, which is the first moment of the distribution $f_m(t)$ given by Eq. 2.20 is equal to the product of the m breaking rates of that bond and the earlier bonds

$$\tau_m = \int_0^\infty dt f_m(t)\, t = \sum_{q=1}^{m} \frac{1}{k_q}. \tag{2.21}$$

Setting $m = N$ and using Eq. 2.17, we obtain the total time for filament peeling

$$\mathcal{T} = k_0^{-1} \sum_{i=1}^{N} e^{-F_i/F_0}, \tag{2.22}$$

where F_i is the force on the first unbroken bond after bonds $1, \ldots, i-1$ have broken. The result is proportional to the fundamental rupture time scale $1/k_0$, specific to the linkers in question.

2.3.1 Asymptotic peeling rates for long filaments

From this linker-breaking scenario for the dissipative dynamics of the network, one must associate the loading time sufficient to cause plastic deformation with the time required for a typically filament to be peeled off of its original links to the network. Thus the mean time for rupturing a significant fraction of linkers from a very long filament gives a prediction of the model for the loading time required for plastic deformation as a function of applied force. Calculating the mean peeling time remains a complex problem for disordered linker arrays and even for ordered linker lattices since the loading on the i^{th} linker generically has a nontrivial dependence on linker number i.

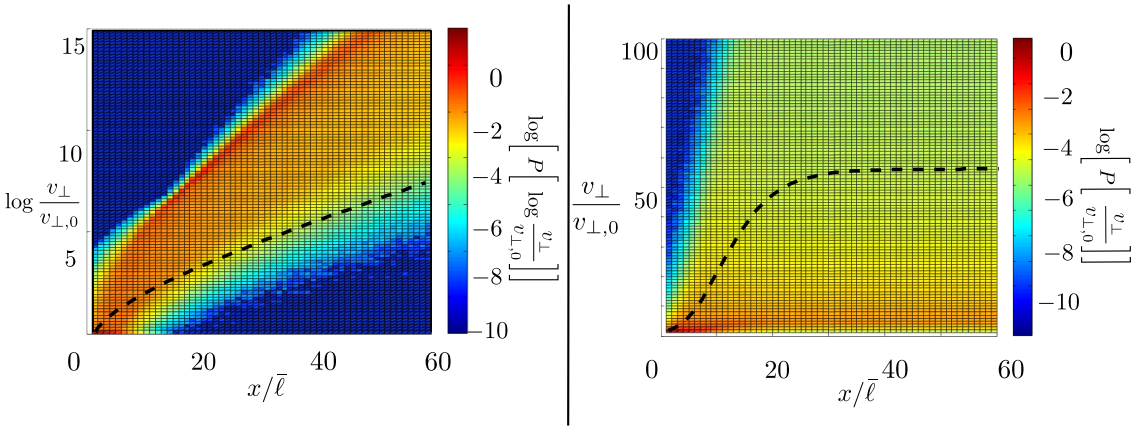

Figure 2.3.2: (Left) Distribution of the logarithm of the perpendicular velocities with $\tau = 0$ showing the predicted peeling acceleration due to the lever arm effect holds in a random array of linkers. Dashed line corresponds to the velocity for an ordered array of cross-linkers. (Right) the same distribution for $\tau = 5\,\mathrm{pN}$, but on a linear scale (right). Here the peeling velocity approaches a constant as predicted based on the lattice calculations.

For peeling a very long filament, however, the asymptotic peeling dynamics reached after many bond ruptures is more easily analyzed. Examining Fig. 2.2.4, we note that in the tension free case, the linker loading increases linearly with linker number: $F_i = \Xi\, i$ due to the lever arm effect. For the case of tensed filaments, the loading plateaus after a finite number of linker ruptures: $F_i = \Xi'$, independent of i. Using these approximations for all of the rupture events contributing to the mean peeling time, one may simply perform the sum in Eq. 2.22 to find for the tension-free case with accelerating peeling

$$\mathcal{T}k_0 = \frac{e^{-\Xi/F_0} - e^{-\Xi(N+1)/F_0}}{1 - e^{-\Xi/F_0}}. \tag{2.23}$$

Due to the unbounded acceleration of the peeling, an infinite number of linkers $N \to \infty$ may be broken in finite time. This unphysical outcome results from our neglect of inertia in the problem, but the high peeling velocity case is not of physical interest as larger displacements of the filament associated with the massive lever arm effect necessarily generate tension. Turning to the case with with tension, leading to constant velocity peeling, we find the simple result

$$\mathcal{T}k_0 = Ne^{-\Xi'/F_0}. \tag{2.24}$$

We tested these approximate solutions to the problem of average peeling dynamics for both ordered and disorder linker arrays using respectively analytic solutions and

numerical simulations. In all cases, mean peeling time scaled with load F as predicted by the above results and the best fit was obtained using $\Xi'/F = 1.92$ and $\Xi/F = 0.25$ (using the values from Fig. 2.3.1). The first result demonstrates the force overshoot leading to a linker loading almost twice that of the applied force; the second shows that, without tension, the loading on sucessive linkers during the peeling grows by one quarter of the total applied force. We now turn to the peeling dynamics simulations in disordered linker arrays.

2.3.2 Peeling dynamics in disordered linker arrays

To explore the single-filament peeling dynamics numerically, we constructed an ensemble of linker distributions for filaments in which the distance to the first linker is from 1 to 60 $\bar{\ell}$. Each filament had a total of 40 linkers, so 39 linkers were distributed beyond the first one. We consider both ordered linker arrays and disordered ones in which the interlinker spacing is selected from a Poisson distribution [39]. The stochastic peeling dynamics were simulated by computing the loading on the first unbroken linker and then selecting a waiting time for rupture using the Bell model. The results are plotted in Fig. 2.3.1. The spatial disorder increases the total time of peeling relative to the linker lattice when the mean linker separation in the disordered case is chosen to be equal to the lattice constant in the ordered one. For each simulated unpeeling event, we compute the normal velocity of the point of loading $v_\perp$,

$$\frac{v_\perp(x)}{v_0} = \frac{\Delta\zeta_0^{(0)}(x)\, k(x)}{\bar{\ell}\, k_0}, \tag{2.25}$$

defined by the product of the jump in the normal displacement of the filament at the point of loading $\Delta\zeta_0^{(0)}$ upon a bond rupture at point x down the filament and the rate of bond breaking of that linker $k(x)$. This velocity is nondimensionalized by the product of the mean interlinker distance and the zero force bond breaking rate $\bar{\ell}k_0 = v_0$ Thus each jump of the filament at the point of loading due to a discrete rupture event contributes to the time-averaged velocity of the point of loading. These velocities are then, in turn, averaged over 1.5×10^5 realizations of the disordered linker positions along the filament (beyond the broken linker in question). Assuming the motion of the tracer particle in experiments depends solely on the unpeeling of one filament, this quantity reflects the bead's observed velocity; we address the validity of this assumption later in our discussion

of the experiments – see Sec. 2.4.

We plot the probability distributions for $v_\perp/v_0$ in Fig. 2.3.2 for tensed (right) and untensed (left) filaments. The most probable peeling velocities as a function of the position of the first unbroken linker x reflect the lattice calculation. The lever-arm effect in the untensed case (left) leads to a high probability of accelerated peeling of the filament even from a disordered array of linkers. Rare "trapping region" configurations of many close linkers produce trapping states that lead to a lower mean velocity of the peeling resulting from a tail of low velocity states in the probability distribution – see the bottom right corner of Fig.7 left. The same feature applies to the tensed case; we see that the highest probability trajectories mimic the predictions of the lattice model. The disordered array of linkers, however, provides new tight-binding regions leading to a significant probability of observing slower peeling dynamics in any realization of the disordered pinning array when compared to the ordered one.

Given the stochastic nature of the peeling dynamics, one expects to observe "ripping events" in which multiple linker rupture in succession over a time short compared to the mean time between such linker ruptures. To look at such ripping events, we calculate the probability of n sequential peeling events occurring over one mean dissociation time $\bar{\tau}$ on a filament bound to N cross-linkers, $\mathcal{P}_N(n)$. Specifically, an n-linker rip occurs when a sequence of consecutive linkers rupture with the sum of their waiting times is less than mean time between ruptures: $\tau_i + \ldots + \tau_{i+n-1} \leq \bar{\tau}$. We allow the same τ_i to be part of multiple dissociation types i.e. if $\tau_1 \leq \bar{\tau}$ and $\tau_1 + \tau_2 \leq \bar{\tau}$, then τ_1 contributes to the count of a single dissociation event as well as a sequential 2 cross-linker dissociation event. The high-n tail of this distribution then reflects the expected rarity of such multiple linker rips. These should be observable in experiment as sudden large-scale jumps of the tracer bead under constant load. We discuss this further in Sec 2.4.

To compute $\mathcal{P}_N(n)$, we created an ensemble of filaments (1.5×10^5 filaments) each with $N = 40$ cross-linkers having a mean spacing, $\bar{\ell}$, of one micron. We looked for ripping events, as defined above, for two different loadings: $F = \{30 \text{ pN}, 120 \text{ pN}\}$ on filaments with and and without applied tension. The results are plotted in Fig. 2.3.3.

As expected, the frequency and size of rips both increase with the force for tensed and untensed filaments. The upper set of histograms in Fig. 2.3.3 show the frequency

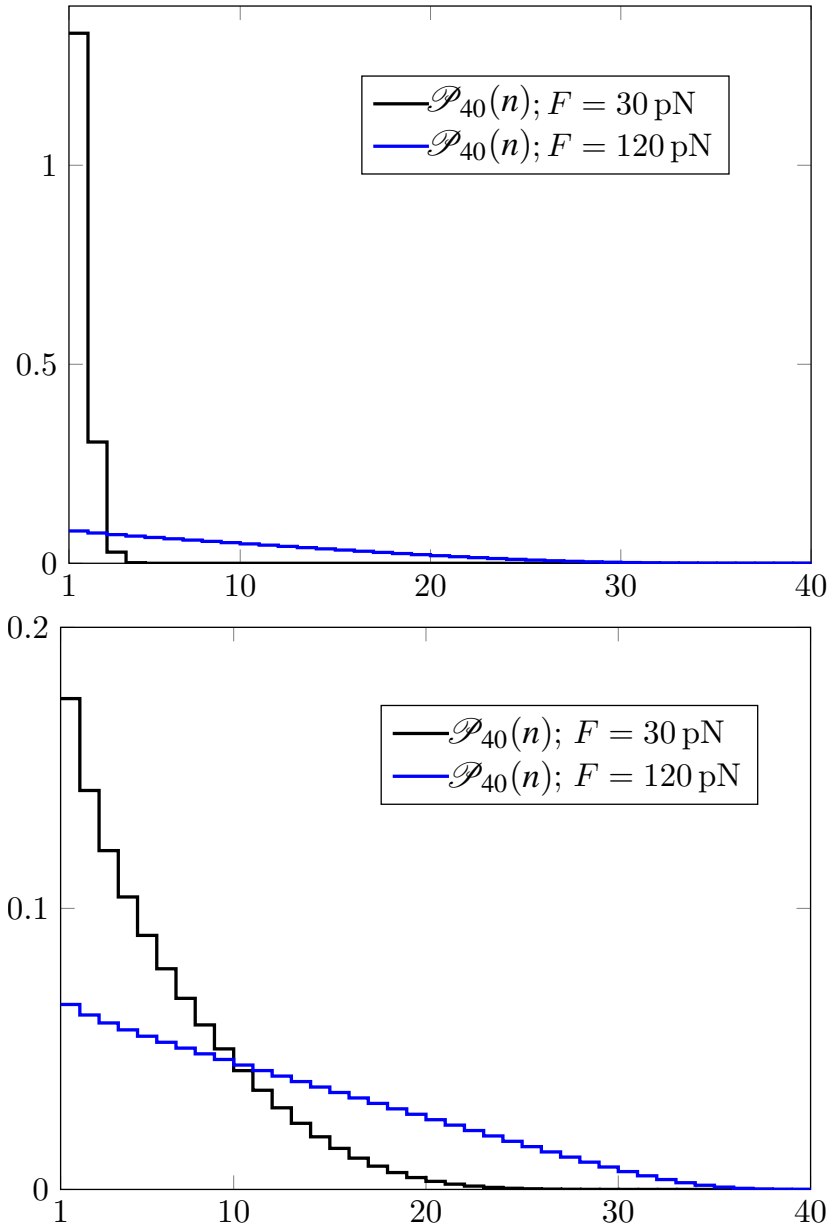

Figure 2.3.3: Distribution of multiple linker rupture events $\mathcal{P}_N(n)$. Top: With tension uncorrelated rupture events are selected from the same Poisson distribution as the loading plateaus. Bottom: Without tension, the lever arm effect accelerates peeling, leading to a higher frequency of fast ruptures or ripping events. $K = 100\,\mathrm{pN}/\mu\mathrm{m}$.

of ripping events of various size for tensed filaments. For small forces, the likelihood of n-linker rip decays exponentially with n, consistent with the waiting times between sequential ruptures being uncorrelated and being selected from the same distribution. This can be understood in terms of our mechanics calculation. Once the rip passes down the filament farther than ℓ_κ, the lever-arm effect is suppressed and the loading on first unbroken linker consequently plateaus. Now the Bell model dissociation rate is fixed for all subsequent ruptures. Waiting times for these ruptures are the selected from a fixed Poisson distribution with no correlations between events. This result holds even in the presence of the quenched linker disorder on the filament. It is the bending modulus and the applied tension down the length of the filament that controls the peeling dynamics.

The lower set of histograms in Fig. 2.3.3 show the frequency of ripping events of various sizes for untensed filaments. Without tension $\ell_\kappa \to \infty$, the lever arm effect applies for all distances producing an unbounded acceleration of the peeling, which in our currently analysis, appears as a high probability of observing large n ripping events. We observe that the probability of observing large n rips decays more slowly than exponentially for large n (in fact, essentially linearly). Without tension, large ripping events become the norm rather than the exception.

2.4 Comparison to experiment

There are really two classes of experiments to which our theory should apply. Single filament manipulation of biopolymers such as F-actin or microtubules should provide the most direct test of the theory. One may imagine a single filament being pulled from a regular or disordered array of sticky sites on a substrate (generated perhaps by micro-contact printing techniques [51]). Given that the Bell model parameters are known with reasonable precision for a number of biologically ubiquitous noncovalent bonds (e.g., biotin avidin binding) and that the elastic properties of the semiflexible filaments are well characterized, such single filament measurements provide the most stringent test of the model, one with no fitting parameters.

As discussed in the introduction, the original inspiration for the theoretical work, however, is found in the many filament experiments in which a large bead (i.e., much

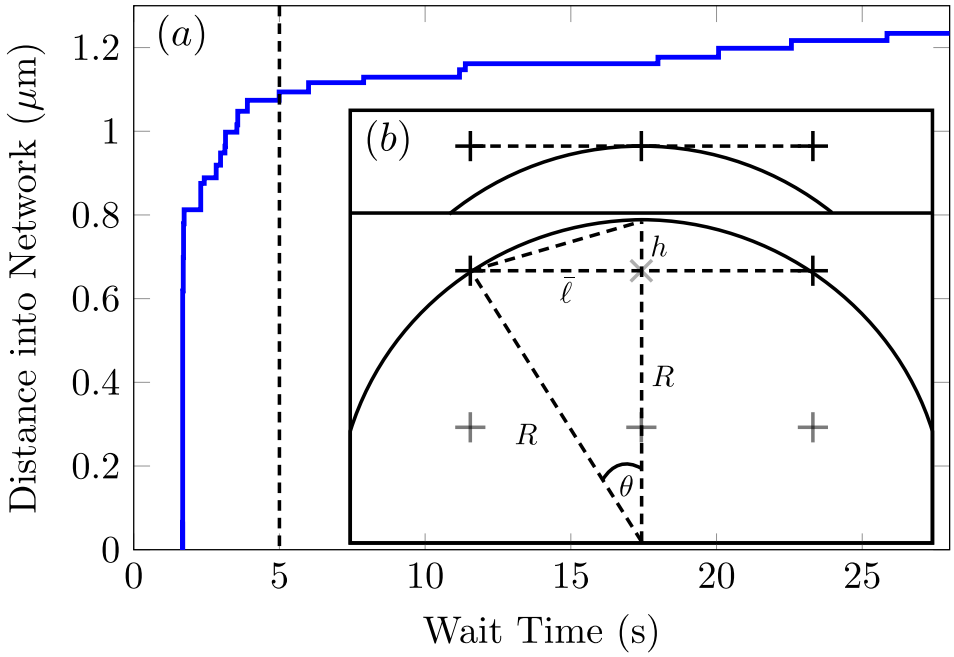

Figure 2.3.4: Representative experimental probe trajectory resolving multiple $\sim$ 10nm scale jumps within the constant velocity regime to the right of the vertical dashed line. (b) Geometric model of the spherical probe of radius R in the semiflexible gel with mesh size $\bar{\ell} = 0.25\mu$m. After linker $\times$ breaks, the probe moves a distance h before contacting the filaments $+$ in the network. For $R \gg \bar{\ell}$, $h \sim$ 10nm.

bigger than the mesh size of the gel) is moved through the network. This sort of test of the single filament model is necessarily less direct, but we believe that the present single-filament calculation provides at least two key insights into the more complex problem of the gel's dynamics.

First and most generally, the calculations show that the loading of cross-linkers is strongest near the point of force application. In the experiment, there are only a small number (order ten) of filaments in direct contact with the bead. Based on the single filament calculations presented here, we see that the total applied force appears essentially on the first cross-linker away from the bead; the small number of filaments in contact with the bead then divide that load over just a few cross-linkers. This assumption was previously made in order to explain the observed linker-breaking rates as a function of force [83]. The present calculation justifies this assumption.

Our present calculation allows us to address a second and more subtle issue of the

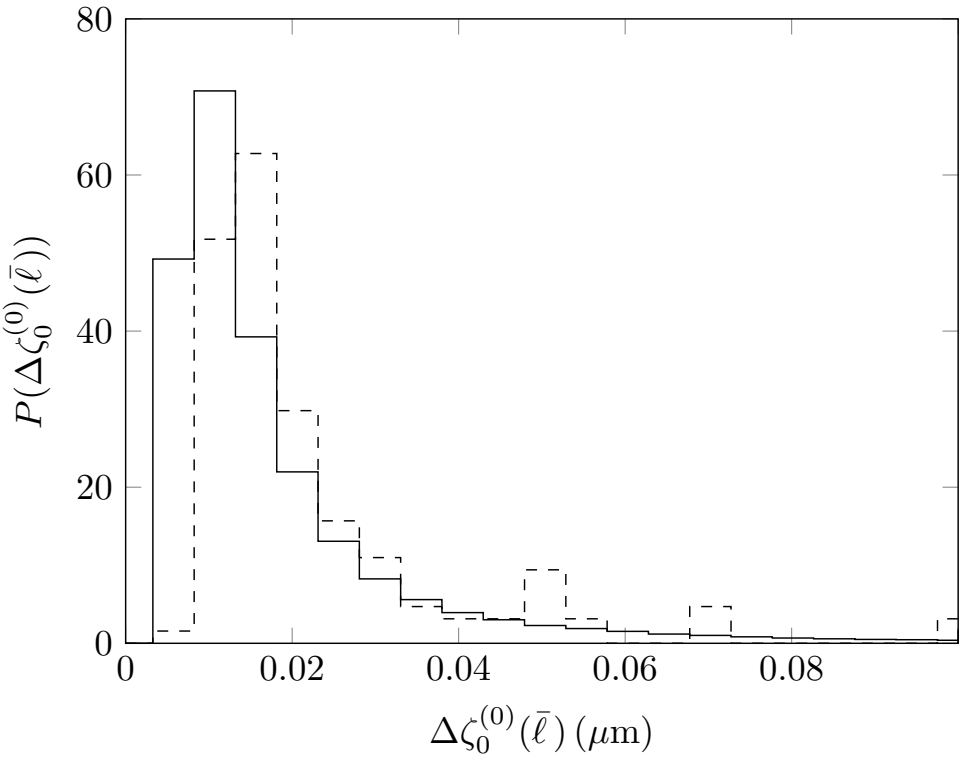

Figure 2.4.1: Dashed Line: Probability distribution of jump sizes for a probe particle under an applied force of 150 pN in a microtubule gel with mesh size$\sim 0.25\,\mu$m. Solid Line: Prediction of jump size distribution for first linker rupture from a disordered linker array with $\bar{\ell} = 0.25\,\mu$m for an untensed filament. $\kappa = 20\,\mathrm{pN}(\mu\mathrm{m})^2$, $K = 100\,\mathrm{pN}/\mu\mathrm{m}$, and $F = 5\,\mathrm{pN}$

observed bead dynamics. Within the apparently constant velocity drift of the bead under load, one observes a spectrum of essentially discontinuous (i.e., more rapid than the data acquisition rate of 60 Hz) jumps of the bead's position, typically on the scale of tens of nanometers. A typical bead trajectory is shown in Fig. 2.3.4 by the solid (blue) line. The initial elastic jump and relaxation of the network occur to the left of the dashed vertical line ($t < 5$s); the set of small jumps making up the "constant velocity" drift of the bead occurs for larger times. From these data at larger times, we plot in Fig. 2.4.1 the observed distribution of such jumps using a dashed line. Given our predictions for the relative probability of larger ripping events along a single filament, we may ask whether the observed distribution of jumps is consistent with large n rips – coordinated ruptures of many linkers along one filament – or simply the result of individual linker ruptures happening independently on different filaments.

To explore the latter hypothesis, we show the expected distribution of bead displacements associated with *single rupture events on a filament* having a Poisson distribution of inter-linker spacing consistent with the experimental gel's mesh size of 0.25μm. This prediction, shown by the solid line in Fig. 2.4.1, is consistent with the observed jump distribution once the applied force on that filament is adjusted to 5pN. This suggests that ~ 30 filaments are involved in supporting the full 150pN load on the bead. That estimate is predicted on using a stiff linker spring constant of 100pN/μm. If this is reduced, one finds the same jump distribution at a larger applied force implying that fewer filaments are engaged. If we were to attempt the to fit the experimental jump frequency data assuming that these jumps are occurring due to multiple sequential rupture evens on one filament, the model would predict larger jumps with too high a frequency to fit the data. Ripping along one filament is inconsistent with these jump frequency data. The picture emerges that the bead's motion is the result of many individual linker ruptures occurring on different filaments in an uncorrelated manner.

Finally, we note that there is a distinct lack of jumps larger than 10nm found in the data. To understand this, consider a simple geometric model of the gel as shown in the inset of Fig. 2.3.4. Here the bead is shown as a circular arc while filaments (heading into the page) are shown as crosses +, separated by the mesh size ℓ. To calculate the largest expected jump, we assume that when one linker ruptures, that filament no longer is able to support the applied load. The filament with the broken linker is shown as $\times$ in the inset. Upon the rupture, the bead moves forward a distance h until it impinges upon new filaments in the network. This simple geometric argument leads to an upper limit on bead jumps $h \sim 10$nm, again consistent with the data. These two lines of evidence support the picture that, in the network, bead motion results from the uncorrelated rupture of linkers on one of the few filaments in direct contact with the bead. We conclude that there are no catastrophic ripping events at least for these loads. In other words, there is nothing like crack propagation as a failure mode.

The single filament peeling dynamics in our single filament model are dominated by the interplay between bending and tension, as demonstrated by the role of ℓ_κ in controlling the lever arm effect. Calculations based on the stochastic peeling dynamics of the filament from a regular array of linkers provides a useful and broadly accurate

understanding of the more complex problem of peeling a filament from a disordered array of linkers with two caveats: (1) linker disorder generically slows the peeling rate relative to that of the lattice with same mean inter-linker spacing; and (2) there is broad tail of the peeling velocity distribution towards slow peeling rates associated with rare "tight-binding" regions consisting of many closely spaced linkers. The analysis of multi-linker rips and the comparison to experiment points to a picture of dissipative dynamics in the gel associated with the uncorrelated rupture of individual linkers on the various filaments in contact with the probe particle. All rupture events should occur essentially at the nearest cross-link to the probe, i.e., within one mesh size from it. We expect this single-filament work to serve as a foundation for more complex multifilament models of linker rupture and dissipative dynamics in a broad class of semiflexible gels.

Appendix

2.A Equations of Equilibrium

Taking the undeformed state of the single filament to be straight, we derive the equations of equilibrium for a filament below a la Landau[49] where the filaments position in space is given by the vector $\vec{r}(l)$. We first consider a single element along the arc-length of the filament dl and derive the force and moment balance equations for this filament. As seen in Figure 2.A.1, there are the internal forces and moments on the filament, $\vec{F}$ and $\vec{M}$ as well as an external force per unit length $\vec{K}$. The sum of all forces and moments acting upon the filament arc-length dl yields the following force and moment balance equations from the simple geometry of the figure to lowest order in dl

$$\frac{d\vec{F}}{dl} = -\vec{K}; \qquad \frac{d\vec{M}}{dl} = \vec{F} \times \vec{t}. \tag{2.26}$$

Assuming that the unit tangent vector is essentially parallel to the undeformed axis of the filament $\hat{z}$ and taking the derivative of the moment balance equation, we arrive at

$$\frac{d^2\vec{M}}{dl^2} = \hat{t} \times \vec{K} + \vec{F} \times \frac{d\hat{t}}{dl}. \tag{2.27}$$

The moments in the $\{\hat{x}, \hat{y}\}$ directions are given approximately by the product of the Young's Modulus, E, and moment of inertia, I, and the component of the rotation vector, $\vec{\Omega}$ i.e. $M_x = EI_\xi \Omega_\xi \approx -EI_x \partial_z^2 Y(z)$ and $M_y = EI_\eta \Omega_\eta \approx EI_y \partial_z^2 X(z)$ where $\vec{r}(l) = \{X(z), Y(z), z\}$ and $\vec{\Omega} = \hat{t} \times \frac{d\hat{t}}{dl} + \hat{t}\Omega_\zeta$. $\{X(z), Y(z)\}$ are the deflection fields in the directions perpendicular to the undeformed filaments contour length Using the derivative of the moment equation, we find equations of equilibrium of the form Eq. 2.3 given in the text.

2.B Transfer matrix

The transfer matrix necessary for the solution of the mechanics problem discussed in Eq. 2.9 is given by $T(\ell_i) =$

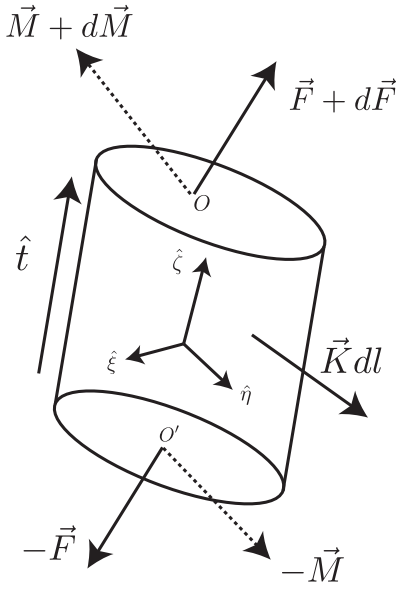

Figure 2.A.1: A small length of a semi-flexible filament dl showing the various forces and moments being applied on said segment. $\vec{F}$ and $\vec{M}$ are the forces and moments being applied at the ends of the filament segment, dl. $\vec{K}$ is the external force per unit length on the filament

$$\begin{pmatrix} 1 & \ell_i & \ell_\kappa^2\left[\cosh \ell_i/\ell_\kappa - 1\right] & \ell_\kappa^3\left[\sinh \ell_i/\ell_\kappa - \ell_i/\ell_\kappa\right] \\ 0 & 1 & \ell_\kappa \sinh \ell_i/\ell_\kappa & \ell_\kappa^2\left[\cosh \ell_i/\ell_\kappa - 1\right] \\ 0 & 0 & \cosh \ell_i/\ell_\kappa & \ell_\kappa \sinh \ell_i/\ell_\kappa \\ -\frac{K}{\kappa} & -\frac{K}{\kappa}\ell_i & \left(\sinh \ell_i/\ell_\kappa - A\left[\cosh \ell_i/\ell_\kappa - 1\right]\right)/\ell_\kappa & \cosh \ell_i/\ell_\kappa - A\left[\sinh \ell_i/\ell_\kappa - \ell_i/\ell_\kappa\right], \end{pmatrix} \tag{2.28}$$

where $A = (K/\tau)\ell_\kappa$. Thus the transfer matrix depends on the bending length ℓ_κ, the distance between consecutive cross-linkers ℓ_i, and the spring constant K of the linker (though the dimensionless parameter A, defined above). In the limit of zero tension,

$\ell_\kappa \to \infty$ the transfer matrix goes to simpler limiting form:

$$T(\ell_i) = \begin{pmatrix} 1 & \ell_i & \ell_i^2/2! & \ell_i^3/3! \\ 0 & 1 & \ell_i & \ell_i^2/2! \\ 0 & 0 & 1 & \ell_i \\ -\frac{K}{\kappa} & -\ell_i \frac{K}{\kappa} & -\frac{K}{2!\,\kappa}\ell_i^2 & 1 - \frac{K}{3!\,\kappa}\ell_i^3 \end{pmatrix} \tag{2.29}$$

In either case, for a fixed array of binding sites, the product of transfer matrices becomes a product of random matrices depending on the quenched random variables ℓ_i. For a regular array of binding sites, this matrix product is easily performed in the diagonal basis. This approach returns us to the discussion of the four eigenvalues of the transfer matrix found in the main text.

2.C Master equation for linker rupture

The integral formulation of the probability of the m^{th} bond rupture at time t given by Eq. 2.19 is a complete solution to the problem of the stochastic dynamics of peeling along any one distribution of linkers; that distribution sets the values of k_i in the integral. The result, however, is more transparent if one takes the time derivative. In that case, due to the sequential breaking approximation, one may write the time derivative of P_m solely in terms of itself and the breakage probability of the last broken cross-linker P_{m-1}:

$$\dot{P}_m(t) = k_m\, P_{m-1}(t) - k_{m+1}\, P_m(t), \tag{2.30}$$

for all but the first cross-linker, i.e., for $m > 0$. The first term represents the increase in breakage probability due to the loss of the $m-1$ cross-linker, making cross-linker m the next to break. The second term represents the breakage of that cross-linker. These equations are supplemented by two more specific to the first

$$\dot{P}_0(t) = -k_1\, P_0(t), \tag{2.31}$$

and last

$$\dot{P}_N(t) = k_N P_{N-1}(t) \tag{2.32}$$

cross-linker, where clearly only one of these two processes are operative. Finally, one needs the initial conditions $P_m(t=0) = \delta_{m0}$, indicating that no linkers are broken initially. At long times, $P_N(t \to \infty) = 1$; any finite filament eventually becomes completely unbound.

CHAPTER 3

The Ion Trap Problem

3.1 Introduction

In this chapter we explore the stochastic dynamics of an ion trapped in a time varying harmonic potential suffering collisions with two nonintectating species of gasses held at different temperatures. We will find that the addition of a second temperature bath for the particle to interact with leads to drastic deviations from the results expected from thermodynamics, statistical mechanics, and the fluctuation-dissipation theorem. We will begin by showing how the typical methods to study such systems fails to produce the correct probability distributions for the position and velocity distributions of the particle in steady state. We will proceed to show that a Master equation approach is the correct way to study such systems. Finally we discuss possible experiments to explain such phenomena. We begin by outlining our motivations to study such problems.

3.2 Motivation

A wide variety of natural processes occur far from equilibrium. Their complex phenomenology is, in many cases poorly understood, but has wide-ranging implications from heart dynamics [64] to climate modeling [68]. These systems may exhibit elaborate spatiotemporal patterns, such as in Rayleigh-Benard convection [19], oscillatory chemical reactions [77], or in swarms of active swimmers [12]. Some theorems [60, 41] have been put forward regarding their (typically large) fluctuations [22]. The number, however, of well-characterized nonequilibrium steady-states is limited. To date, soft matter systems such as active gels [59], colloids [62], or fluids [31, 32] have been considered as prototypical models. Developing even simpler model systems amenable to precise control of their nonequilibrium state is essential for further progress in the field.

We investigate such a prototypical nonequilibrium system consisting of a single ion immersed in two non-interacting ideal gases, which can be realized in a recently developed hybrid atom-ion trap [66, 38, 65, 84, 82, 35]. There, the single ion, held in a radio-frequency (rf) trap, interacts with either two-independent laser-cooled buffer gases or one laser-cooled buffer gas and a low pressure background gas. Because the neutral-ion collision cross section is orders of magnitudes larger than neutral-neutral collision cross sections, the interaction of the buffer gases with one another can be neglected, so that the buffer gas species may have large temperature differences, driving the system out of equilibrium. The rf trap also generates micro-motion [52], further driving the ion out of equilibrium [23, 17]. In our theoretical analysis, we distinguish these two effects by considering both the experimental rf trap and a hypothetical static one.

We show here that an ion in either trap with a two-temperature buffer gas should exhibit striking nonequilibrium features. We focus on three in particular. We demonstrate (i) large departures from a Maxwellian velocity distribution and (ii) the non-factorizability of the joint position–velocity probability distribution. This factorizibility is a hallmark of classical equilibrium statistical mechanics. In the nonequilibrium state, the ion exhibits *position-velocity sorting* wherein ionic high velocity states are overpopulated in regions of high potential energy relative to regions of low potential energy. This property allows one to construct, in principle, a heat engine, even in the static trap, using the edges and center of the trap as heat sources and sinks, respectively. We also demonstrate (iii) the breakdown of the fluctuation-dissipation theorem from a comparison of ionic mobility and diffusion. There will be interesting nonequilibrium effects in ionic transport. These three features demonstrate that this system is a rich playground for exploring nonequilibrium physics in a precise and controllable manner. We conclude by suggesting experiments to observe these features and propose future research directions.

We begin with a one-dimensional model of a trapped ion of mass M interacting with two non-interacting ideal gases of masses $m_{\rm h}$ and $m_{\rm c}$ at differing temperatures – see the inset of Fig. 1 for a schematic representation of the ion (green) in a potential interacting with hot (red) and cold (blue) atoms. The time-dependent probability distribution $P(x, v, t)$ of the ion velocity v and position x obeys the master equation

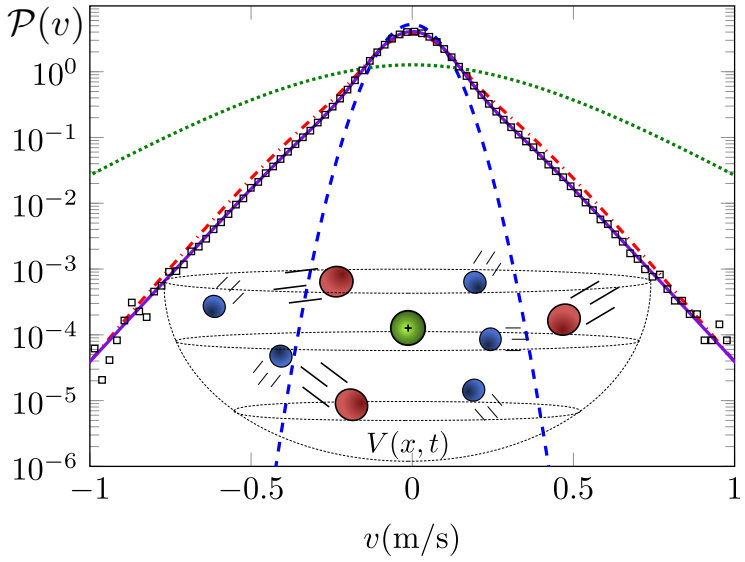

Figure 3.2.1: Steady-state ionic velocity distribution $\mathcal{P}(v)$ for a two-temperature buffer with $T_c = 1(\mathrm{m/s})^2 = 0.01T_h$ with no trap. $m_c/m_h = 20$, $m_c/M = 40/173$. The distribution is shown for a Langevin ion-atom cross section (purple, solid) and a geometric cross section (red,dashed-dotted). The power-law velocity tails agree with a Monte Carlo simulation of the velocity transitions (open squares), and are distinct from the Gaussian MB distribution of the cold atoms (blue dashed line). Time-averaged $\mathcal{P}(v)$ in a rf trap with $\Omega = 2\pi\mathrm{s}^{-1}$ and a spring constant $k = 100\,s^{-2}$ and using the Langevin collision cross section is shown by the (green) dotted line.

$$\left(\partial_t + v\,\partial_x + \frac{F(x,t)}{M}\,\partial_v\right) P(x,v,t) = \int dv'\, W(v|v')P(x,v',t) - \int dv'\, W(v'|v)\, P(x,v,t). \tag{3.1}$$

The left side of Eq. 3.1 contains the time derivative of the probability density and two streaming terms representing the advection of probability in position space due to the ion velocity v and the advection of probability in velocity space due to the acceleration of the ion in response to the trapping force $F(x,t)$. The terms on the right side of Eq. 3.1 represent the effect of collisions between the ions and the buffer gases. These collisions generate ion velocity transitions from v_1 to v_2 with probability per unit time $W(v_2|v_1)dv_2$. We assume that the two buffer gases are themselves in equilibrium states with Maxwell-Boltzmann (MB) velocity distributions corresponding to temperatures $T_h > T_c$ and number densities c_h, c_c respectively. The buffer gases constitute large enough thermal reser-

voirs to maintain their temperatures in spite of the exchange of energy with the ion, and are decoupled from the external force $F(x,t)$, which acts solely on the ion.

This master equation was studied by Alkemade and van Kampen [1], where it was assumed that the ionic mass M was sufficiently large compared to those of the buffer gas atoms that one may expand W for small momentum transfer. This allowed the replacement of the above integro-differential equation with a differential equation containing a small expansion parameter related to the ratio of the buffer gas mass to the tracer particle mass. In order to account for hot and heavy buffer gasses we avoid this Kramers-Moyal expansion. Nevertheless, it will be of interest to compare and contrast the results associated with a Kramers-Moyal expansion in our study of this system.

3.3 Calculation of Velocity Distribution using Kramers-Moyal Expansion

3.3.1 Velocity Difference Moments for two Temperature System

Here we expand the Master equation using a Kramers-Moyal expansion a la [1] in the parameter $\epsilon = M^{-1/2}$ for the ion embedded in a two temperature buffer gas system and show how various approaches using a Focker-Planck and Langevin approach fail to explain the ion/two buffer gasses at drastically different temperature systems.

In order to calculate the probability distribution for the ion's velocity v as described in [1], $\mathcal{P}(v,t)$, we must derive the probability per unit time, $W(v'|v)$, that the ion goes from a velocity v to a velocity $v'+dv'$ arbitrary buffer gasses with temperature T_i due to elastic collisions, (Eqns. (13a) and (13b) of [1])

$$W(v'|v) = \sum_l \left(\frac{M+m_l}{2m_l}\right)^2 (v'-v) f_l \left(\frac{M+m_l}{2m_l}v' - \frac{M-m_l}{2m_l}v\right) \text{ for } v' > v \tag{3.3}$$

$$= \sum_r \left(\frac{M+m_r}{2m_r}\right)^2 (v-v') f_r \left(\frac{M+m_r}{2m_r}v' - \frac{M-m_r}{2m_r}v\right) \text{for } v' < v \tag{3.4}$$

where the summation over the indices l and r extends over all particle species to the

left (right) side of the ion with masses $m_l\,(m_r)$ and

$$f_i(v) = c_i \left(\frac{m_i}{2\pi k_B T_i}\right)^{\frac{1}{2}} \exp\left[-\frac{m_i v^2}{2k_B T_i}\right] \tag{3.5}$$

is the one-dimensional Maxwell velocity distribution for particle species i with concentration c_i, mass m_i, on its respective side with temperature T_i.

Given the forms of Eq. (3.3) and (3.4), we recalculate the derivatives of the velocity difference moments $\alpha_n^{(p)}$ given in [1] using these modified Maxwell distributions of the left and right buffer gasses and find that

$$\alpha_n^{(p)} = \sum_l \left(\frac{1+m_l/M}{2m_l}\right)^2 \int_0^\infty dq\, q^{n+1} f_l^{(p)} \left(\frac{1+m_l/M}{2m_l} q\right) - \tag{3.6}$$

$$\sum_r \left(\frac{1+m_r/M}{2m_r}\right)^2 \int_{-\infty}^0 dq\, q^{n+1} f_r^{(p)} \left(\frac{1+m_r/M}{2m_r} q\right) \tag{3.7}$$

where like in [1], $f_i^{(p)}$ denotes the p^{th} derivative of $f_i(v)$ evaluated at $((1+m_i/M)/2m_i)\,q$ respectively.

The evaluation of Eq. (3.7) follows identically to the calculation in the appendix of [1] only with small modifications to the terms related to the temperatures of the two sides of the ion yielding the following general expressions for $\alpha_n^{(p)}$:

$$\alpha_n^{(p)} = \frac{(-1)^{\frac{1}{2}(p+n+2)}}{\sqrt{\pi}} 2^{n-\frac{1}{2}}\,(n+1)!\,(p-n-3)!!\times$$

$$\sum_i (\pm_i)^{n+p} c_i m_i^{\frac{1}{2}(n+p-1)}\,(k_B T_i)^{-\frac{1}{2}(p-n-1)}\,(1+m_i/M)^{-n}\; p > n+1; p-n \text{ even} \tag{3.9}$$

$$= 0 \text{ for } p > n+1; p-n \text{ odd} \tag{3.10}$$

$$= \frac{(-1)^p}{\sqrt{\pi}} 2^{\frac{1}{2}(3n-p-1)} \frac{(n+1)!}{(n+1-p)!} \Gamma\left[\frac{1}{2}(n-p)+1\right] \times$$

$$\sum_i (\pm_i)^{n+p} c_i m_i^{\frac{1}{2}(n+p-1)}\,(k_B T_i)^{\frac{1}{2}(n-p+1)}\,(1+m_i/M)^{-n} \text{ for } p \le n+1 \tag{3.11}$$

where the index i denotes the sum over the left and right sides and $(\pm_i)$ is $(+1)$ for the i^{th} gas species in the left chamber and (-1) for the i^{th} species in the right chamber.

The only differences that now arise in the calculation of the $\mathcal{P}(v,t)$ to arbitrary order in ϵ calculated in [1] versus those of the two temperature problem found here are the redefinitions of the $\alpha_n^{(p)}$ in Eqns. (3.9), (3.10), and (3.11). All other formulas are identical to those found in [1].

3.3.2 Velocity Difference Moments for Langevin Collsion Cross-Section

As we are interested in modeling the effect of two noninteracting buffer gasses interacting with an ion, we take into account the appropriate Langevin collision cross-section and rederive the velocity difference moments for neutral particles colliding with an ion as well.

We make the ansatz, using the work of [21] and [16] for the collision cross-section of a neutral atom with an ion, and modify our velocity transition rates for an elastic cross-section by taking $W(v'|v) \to W(v'|v)\sigma_L$ where $\sigma_L = \pi\, g\, \sqrt{4\, C_4/|v'-v|^2\mu_i}$, where g has units of m^{-2} to correct for the 1-D nature of our collisions, μ_i is the reduced mass for the collision for the appropriate buffer gas with the ion, and C_4 is a constant related to the polarizability of the neutral atoms. We take $g = 2\frac{m_i}{m_i+M}m^{-2}$ in our calculations for both gasses to match the collision rates of [16]. We may now expand the master equation using these modified velocity transition rates i.e.

$$\begin{aligned}\partial_t P(x,t) = &\int dq\, \Phi(\epsilon x - \epsilon^4 q; q) P(x - \epsilon^3 q, t) \\ &- \Phi(\epsilon x; q) P(x,t)\end{aligned} \tag{3.12}$$

where $M = \epsilon^{-2}$, $q = M^2 = (v'-v)$, $\epsilon x = v$, and

$$\begin{aligned}\Phi(V;q) = &\sum_l \left(\frac{1+m_l/M}{2\,m_l}\right)^{3/2} \pi\, g \sqrt{8\, C_{4,l}} f_l \left(v + q\left(\frac{1/M + m_l/M^2}{2m_l}\right)\right); \text{for } q > 0 \\ &\sum_r \left(\frac{1+m_r/M}{2\,m_r}\right)^{3/2} \pi\, g \sqrt{8\, C_{4,r}} f_r \left(v + q\left(\frac{1/M + m_r/M^2}{2m_r}\right)\right); \text{for } q < 0\end{aligned} \tag{3.13}$$

Performing the Kramers-Moyal expansion yields

$$\partial_t = \sum_{n=1}^{\infty} (-1)^n \frac{\epsilon^{3\,n}}{n!} \partial_x^n \left(\alpha_n(\epsilon x) P(x,t)\right) \tag{3.14}$$

means we must now evaluate the following velocity difference moments of

$$\alpha_n = \int dq\, q^n \Phi(\epsilon x; q) \tag{3.15}$$

We expand the α_n and find

$$\alpha_n = \sum_{p=0}^{\infty} \alpha_n^{(p)} \frac{(\epsilon x)^p}{p!} \tag{3.16}$$

where now the full master equation may be written as

$$\partial_t P(x,t) = \sum_{n=1}^{\infty} \frac{(-1)^n}{n!} \sum_{p=0}^{\infty} \frac{\epsilon^{3\,n+p}}{p!} \alpha_n^{(p)} \partial_x^n \left(x P(x,t) \right) \tag{3.17}$$

. The calculation of the $\alpha_n^{(p)}$ amounts to evaluating integrals of the following form:

$$\begin{aligned} \alpha_n^{(p)} = & \sum_l \left(\frac{1 + m_l/M}{2 m_l} \right)^{3/2} \pi\, g \sqrt{8\, C_{4,l}} \int_0^{\infty} dq\, q^n f_l^{(p)} \left(q \left(\frac{1/M + m_l/M^2}{2 m_l} \right) \right) + \\ & \sum_r \left(\frac{1 + m_r/M}{2 m_r} \right)^{3/2} \pi\, g \sqrt{8\, C_{4,r}} \int_{-\infty}^{0} dq\, q^n f_r^{(p)} \left(q \left(\frac{1/M + m_r/M^2}{2 m_r} \right) \right). \end{aligned} \tag{3.18}$$

We rescale q and find the new integral may be written as

$$\alpha_n^{(p)} = \sum_i (\pm)^{n+p} \left(\frac{1 + m_i/M}{2 m_i} \right)^{3/2} \left(\frac{2 m_i}{1/M + m_i/M^2} \right)^{n+1} \pi\, g \sqrt{8\, C_{4,i}} \int_0^{\infty} dv\, v^n f_i^{(p)}(v) \tag{3.19}$$

where the $+(-)$ sign corresponds to particles to the left (right) of the ion. First we consider the limit that $p > n$; then by integration by parts we arrive at

$$\begin{aligned} \alpha_n^{(p)} = & (-1)^n n! \sum_i (\pm)^{n+p} \left(\frac{1 + m_i/M}{2 m_i} \right)^{3/2} \left(\frac{2 m_i}{1/M + m_i/M^2} \right)^{n+1} \pi\, g \sqrt{8\, C_{4,i}} \times \\ & \int_0^{\infty} dv\, f^{(p-n)}(v) \end{aligned} \tag{3.20}$$

where the integral equals $-f^{(p-n-1)}(0)$ which vanishes for $p-n$ even and for $p-n$ odd equals

$$(-1)^{\frac{1}{2}(p-n+1)} c_i \left(\frac{m}{2\,\pi\, k_B T_i} \right)^{\frac{1}{2}} \left(\frac{m}{k_B T_i} \right)^{\frac{1}{2}(p-n-1)} (p-n-2)!!. \tag{3.21}$$

For $p \leq n$ we arrive at

$$\begin{aligned} \alpha_n^{(p)} = & (-1)^p \frac{n!}{(n-p)!} \sum_i (\pm)^{n+p} \left(\frac{1 + m_i/M}{2 m_i} \right)^{3/2} \left(\frac{2 m_i}{1/M + m_i/M^2} \right)^{n+1} \pi\, g \sqrt{8\, C_{4,i}} \times \\ & \int_0^{\infty} dv\, v^{n-p} f_i(v) \end{aligned} \tag{3.22}$$

where the integral evaluates to

$$\frac{2^{\frac{1}{2}(n-p-2)}}{\sqrt{\pi}} \Gamma \left[\frac{1}{2}(n-p+1) \right] c_i \left(\frac{m_i}{k_B T_i} \right)^{\frac{1}{2}(p-n)} \tag{3.23}$$

Thus $\alpha_n^{(p)}$ in general evaluates to

$$\begin{aligned}\alpha_n^{(p)} =& 2^{n+2}(-1)^{\frac{1}{2}(n+p+1)} n!(p-n-2)!! M^{n+1}\sqrt{\pi}\sum_i (\pm)^{n+p} g\, c_i \sqrt{C_{4,i}} \times \\ & m_i^{\frac{1}{2}(p+n+2)} (k_B T_i)^{\frac{1}{2}(n-p)} (1+m_i/M)^{-n+\frac{1}{2}}; \\ & p > n.\ p-n \text{ odd}. \\ =& 0;\ p > n.\ p-n \text{ even}. \\ =& 2^{\frac{1}{2}(3n-p+1)}(-1)^p \frac{n!}{(n-p)!}\Gamma\left[\frac{1}{2}(n-p+1)\right] M^{n+1}\sqrt{\pi}\sum_i (\pm)^{n+p} g\, c_i \sqrt{C_{4,i}} \\ & m_i^{\frac{1}{2}(p+n)} (k_B T_i)^{\frac{1}{2}(n-p)} (1+m_i/M)^{-n+\frac{1}{2}} \end{aligned} \tag{3.24}$$

3.3.3 Kramers-Moyal Expansion

Using the redefinitions of the $\alpha_n^{(p)}$, let us re-derive some of the relationships of the $\mathcal{O}(\epsilon^2)$ relationships between the $\alpha_n^{(p)}$ in the two temperature bath limit for particles with an elastic collision cross-section[1]. Proceeding from Eqn. (20a) of [1], let us prove the pressures on both sides of the ion are equal at equilibrium to $\mathcal{O}(\epsilon^2)$ i.e. we calculate the time rate of change of the velocity of the ion for a sub-ensemble of systems with velocity v_0 at $t = 0$

$$\begin{aligned}\frac{d}{dt}\langle v\rangle_{sub} = \frac{\langle dv\rangle_{sub}}{dt} &= \left\langle \lim_{\Delta t\to 0}\frac{v-v_0}{\Delta t}\right\rangle_{sub} \\ &= \left\langle \lim_{\Delta t\to 0}\frac{\Delta v}{\Delta t}\right\rangle_{sub} \\ &= \frac{\alpha_1(v_0)}{M}\end{aligned} \tag{3.25}$$

where we used $v = v_0 + \Delta v$ and the definition of α_n found in Eqn. (9) of [1]. Taking an overall ensemble average at equilibrium, we find that

$$\frac{d}{dt}\langle v\rangle_{eq} = \langle \alpha_1(v)\rangle_{eq} = 0. \tag{3.26}$$

Expanding Eq. (3.26) to $\mathcal{O}(\epsilon^2)$, we find that $\langle \alpha_1(V)\rangle_{eq} = \left\langle \alpha_1^{(0)}(0)\right\rangle = \mathcal{O}(\epsilon^2) \approx 0$, which implies that the pressures, p_l and p_r, on both sides are equal (much like in [1]'s one temperature system) i.e. $\sum_l k_B T_l c_l - \sum_r k_B T_r c_r = p_l - p_r = 0$ after dropping all higher order terms in ϵ. Knowing now that $\alpha_1^{(0)} = 0$ (to $\mathcal{O}(\epsilon^2)$), we may now proceed to write

[1]The calculations are nearly identical for the Langevin collision cross-section with the appropriate substitutions of terms

out the Master Equation expanded in the small parameter ϵ (using [1]'s redefinition of v i.e. $v \to M^{1/2}v$) of [1] to $\mathcal{O}(\epsilon^2)$ i.e.

$$\partial_t \mathcal{P}(v,t) = -\,\epsilon\,\partial_v\left(\epsilon\alpha_1^{(1)} v\mathcal{P}(v,t)\right) + \frac{\epsilon^2}{2}\alpha_2^{(0)}\partial_v^2\mathcal{P}(v,t) \tag{3.27}$$

We may use Eqn. (3.27) to calculate the time rate of change of the average velocity $\langle v(t)\rangle$ which is

$$\frac{d}{dt}\langle v(t)\rangle = \epsilon^2\,\alpha_1^{(1)}\;\langle v(t)\rangle \tag{3.28}$$

Note that the boundary condition of $\langle v\rangle_{eq} = 0$ from equilibrium considerations is already built into our solution as $\operatorname{sgn}\alpha_1^{(1)} = -1$, and our previous arguments in Eqn. (3.26) allowed us to drop the $\alpha_1^{(0)}$ term. We arrive at the following solution for Eqn. (3.28) of

$$\langle v(t)\rangle = \langle v(0)\rangle \exp\left[\frac{\alpha_1^{(1)}}{M}t\right] \tag{3.29}$$

thereby indicating that had we started from a phenomenological theory of the movement of the ion, one would have identified $\alpha_1^{(1)}$ as the damping constant $-\Gamma$. This fact will be exploited in our Langevin approach in the next subsection.

In addition to allowing us to solve for the average velocity, Eqn. (3.27) allows us to solve for the equilibrium distribution of velocities for the ion (which we expect to be Maxwellian) if we wish. Rewriting Eqn. (3.27) for the equilibrium distribution we find $-\partial_v\left(\alpha_1^{(1)} v\mathcal{P}_{eq}(v)\right) + \left(\alpha_2^{(0)}/2\right)\,\partial_v^2\mathcal{P}_{eq}(v) = 0$. We integrate once and solve the inhomogenous first-order differential equation in v, impose the boundary conditions that $\int dv\mathcal{P}_{eq}(v) = 1$ and $\langle v\rangle_{eq} = 0$ to find

$$\mathcal{P}_{eq}(v) = \left(\frac{M}{2\pi k_B T_P}\right)^{\frac{1}{2}} \exp\left[-\frac{Mv^2}{2k_B T_P}\right]; \tag{3.30}$$

$$T_P = \frac{\sum_l T_l^{3/2} m_l^{1/2} c_l + \sum_r T_r^{3/2} m_r^{1/2} c_r}{\sum_l T_l^{1/2} m_l^{1/2} c_l + \sum_r T_r^{1/2} m_r^{1/2} c_r}, \tag{3.31}$$

where T_P is the effective temperature of the ion using the Kramers-Moyal expansion to second order in ϵ, noting that the pressure condition must hold true for this equilibrium distribution to hold, thereby restricting the values the temperatures and concentrations the gasses can take.

Repeating the equilibrium arguments of Eqn. (20a) in [1], independent of our calculation of $\mathcal{P}_{eq}(v)$, we find T_P again and through some trivial algebra (to order $\mathcal{O}(\epsilon^2)$) it is easy to prove that

$$\alpha_2^{(0)} + 2\alpha_1^{(1)} k_B T_P = 0 \tag{3.32}$$

Similarly, we may perform such an expansion then the gasses have a Langevin collsion cross-section with the ion. Rewriting the expanded Master equation using the velocity variable, v, we find that we may describe the velocity distribution of the ion to lowest order in ϵ as

$$\partial_t P(v,t) = -\alpha_1^{(1)} \partial_v (v\, P(v,t)) + \frac{\alpha_2^{(0)}}{2\, M} \partial_v^2 P(v,t) \tag{3.33}$$

where $\alpha_1^{(1)} = -2^{3/2}\pi \sum_i \sqrt{C_{4,i}} g\, m_i\, c_i$ and $\alpha_2^{(0)} = 2^{5/2}\pi \sum_i \sqrt{C_{4,i}} g\, m_i\, c_i k_B T_i$ which clearly satisfies the necessary fluctuation-dissipation theorem relationship between the friction and the thermal fluctuations much like the elastic collision cross section. To show that these results are identical to those expected from a linear approximation, we use a Langevin noise approach to study the system next.

3.3.4 Langevin Approach

Let us write down a stochastic differential equation for the ion's velocity subject to two random thermal forces, $f_l(t)$ and $f_r(t)$ (white thermal noise) and solve for the corresponding probability distribution, $\mathcal{P}(v,t)$ using standard methods such as those found in [14] i.e.

$$M \frac{d}{dt} v(t) = -(\Gamma_l + \Gamma_r)\, v(t) + f_l(t) + f_r(t)$$

$$\langle f_l(t) \rangle = \quad p_l; \langle \Delta f_l(t) \Delta f_l(t') \rangle = 2\Gamma_l k_B T_l \delta(t - t') \tag{3.35}$$

$$\langle f_r(t) \rangle = -p_r; \langle \Delta f_r(t) \Delta f_r(t') \rangle = 2\Gamma_r k_B T_r \delta(t - t') \tag{3.36}$$

where $\Delta f_i(t) = f_i(t) - \langle f_i(t) \rangle \{i = l, r\}$ and $\Gamma = \Gamma_l + \Gamma_r = -\alpha_1^{(1)}$.
Let us rewrite Eqn. (3.35) in the ω space using the $\Delta f_i(\omega) = \int dt \exp(i\omega t) \Delta f_i(t)$

$$v(\omega) = \frac{\Delta f_l(\omega) + \Delta f_r(\omega)}{(-i\,\omega\, M + \Gamma)} + \frac{2\pi (p_l - p_r)\delta(\omega)}{(-i\,\omega\, M + \Gamma)} \tag{3.37}$$

which now allows us to calculate the velocity-velocity correlation function $C_{vv}(\omega) = \langle v(\omega)v(-\omega)\rangle$ averaged over the thermal noises

$$C_{vv}(\omega) = \frac{2k_BT_l\Gamma_l + 2k_BT_r\Gamma_r}{|-i\omega\, M + \Gamma|^2} + \frac{4\pi^2(p_l - p_r)^2\delta(\omega)}{|-i\omega\, M + \Gamma|^2}. \tag{3.38}$$

Let us transform $C_{vv}(\omega)$ back to the time domain and solve for the equal time velocity-velocity correlation function in order to figure out what T_{eq} of the ion must be subject to these two thermal forces and using the equipartition theorem[2] i.e.

$$\left\langle v^2(t)\right\rangle_{eq} = \frac{k_BT_{eq}}{M} = \int \frac{d\omega}{2\pi} C_{vv}(\omega) = \frac{2k_BT_l\Gamma_l + 2k_BT_r\Gamma_r}{2\,M\,\Gamma}. \tag{3.39}$$

A quick glance of Eqn. (3.39) immediately reveals that T_{eq} is nothing more than

$$T_{eq} = \frac{T_l\,\Gamma_l + T_r\,\Gamma_r}{\Gamma_l + \Gamma_r} = T_P \tag{3.40}$$

or the average of the temperatures, weighted by their associated damping coefficient, a much more insightful way of expressing Eqn. (3.31). Having now recovered the same equilibrium temperature as our small parameter expansion Master equation approach from the Fluctuation-Dissipation theorem, we should expect to recover the same Focker-Planck equation for the probability distribution, $\mathcal{P}(v,t)$ to $\mathcal{O}(\epsilon^2)$. We do this below.

Given that the conditional probability of the ion to go from a state with velocity v_0 at t_0 to a state of velocity V at t is $\mathcal{P}(v,t|v_0,t_0) = \langle\delta(v - v(t))\rangle_{v_0,t_0}$, we may find the probability that a ion is in a state with velocity v at time $t + \Delta t$ from

$$\mathcal{P}(v,t+\Delta t|v_0,t_0) = \int dv_1 \mathcal{P}(v,t+\Delta t|v_1,t)\mathcal{P}(v_1,t|v_0,t_0) \tag{3.41}$$

We may expand the conditional probability $\mathcal{P}(v,t+\Delta t|v_1,t) = \langle\delta\left(v - v(t+\Delta t)\right)\rangle_{v_1,t}$ in orders of $\Delta v = v(t+\Delta t) - v(t)$

$$\langle\delta(v - v(t+\Delta t))\rangle_{v_1,t} = \delta(v - v_1) - \langle\Delta v\rangle_{v_1,t}\,\partial_{v_1}\delta(v - v_1) + \frac{\left\langle(\Delta v)^2\right\rangle_{v_1,t}}{2}\partial^2_{v_1}\delta(v - v_1) \tag{3.42}$$

and using the integrated form of the equation of motion of the ion from t to $t+\Delta t$, we may solve for the moments of Δv averaged over the thermal noise i.e. taking the average

[2]The astute reader will complain that we have thrown away the $(p_l - p_r)$ term of Eqn. (3.38), however using equilibrium considerations, we will find it to be zero in the derivation of the probability distribution $\mathcal{P}(v,t)$ using the Langevin approach.

of

$$\Delta v = -\frac{\Gamma}{M}\, v_1 \Delta t + \frac{1}{M}\int_t^{t+\Delta t} dt' \left(f_l(t') + f_r(t')\right). \tag{3.43}$$

The two most important moments in calculating the conditional probability, $\mathcal{P}(v, t+\Delta t|v_0, t_0)$, to first order in Δt are $\langle \Delta v \rangle_{v_1,t}$ and $\left\langle (\Delta v)^2 \right\rangle_{v_1,t}$ which are respectively

$$\langle \Delta v \rangle_{v_1,t} = -\frac{\Gamma}{M} v_1 \Delta t + \frac{1}{M}\left(p_l - p_r\right)\Delta t \tag{3.45}$$

$$\left\langle (\Delta v)^2 \right\rangle_{v_1,t} = \frac{2\,\Gamma\, k_B\, T_p}{M^2}\Delta t. \tag{3.46}$$

Now having the moments of Δv, we may perform the appropriate integrations by parts on Eqn. (3.41) and expansion to $\mathcal{O}(\Delta t)$ to recover the following Focker-Planck equation

$$\begin{aligned}\partial_t \mathcal{P}(v, t|v_0, t_0) = &-\frac{1}{M}\partial_v \left[\left(p_l - p_r - \Gamma\, v\right)\mathcal{P}(v, t|v_0, t_0)\right] + \\ &\frac{\Gamma\, k_B\, T_p}{M^2}\partial_v^2 \mathcal{P}(v, t|v_0, t_0).\end{aligned} \tag{3.47}$$

Solving for the equilibrium distribution of Eqn. (3.47) and imposing the equilibrium condition of $\langle v \rangle_{eq} = 0$ yields $\mathcal{P}_{eq}(v)$ of Eqn. (3.30) and $p_l = p_r$ as before. Two separate approaches to solving for the probability distribution have yielded to same results to $\mathcal{O}(\epsilon^2)$. In the next section, we proceed on with our Kramers-Moyal expansion to $\mathcal{O}(\epsilon^4)$ in the presence of a spatially dependent force field.

3.3.5 Particle in a Harmonic Trap

We generalize our master equation approach to include interactions with a spatial and time-dependent force field $F(x,t) = -\partial_x U(x,t) + F_0(t)$ where $U(x,t)$ is the potential energy of the ion at position x and time t, and $F_0(t)$ is some active forcing term. This means that the energy of the ion in the absence of the ideal gas buffers may be written as

$$E(x, v, t) = \frac{1}{2} M\, v^2 + U(x,t) - x\, F_0(t) \tag{3.48}$$

In order to derive the master equation of the now spatially dependent probability distribution, $P(x, v, t)$, we must derive the transition probability rates from a state with velocity and position $\{x, v\}$ to a state with velocity and position $\{x', v'\}$, i.e.in the absence of a collision with the buffer gases and in the presence of a collision with the

buffer gases. The total transition rate from the initial to final states may be written as $W_{\rm total}(x',v'|x,v) = W_{\rm free}(x',v'|x,v) + W_{\rm collision}(x',v'|x,v)$. The transition probability rate during a time interval dt in the absence and presence of collisions may be written as

$$W_{\rm free}(x',v'|x,v) = \frac{1}{dt}\delta(v' - (v + \frac{F(x,t)}{M}dt))\delta(x' - (x + v\,dt)) \tag{3.49}$$

$$W_{\rm collision}(x',v'|x,v) = (\text{Eqn. (3.3)}\,\theta(v'-v) + \text{Eqn. (3.4)}\,\theta(v-v'))\,\delta(x' - (x + v\,dt)) \tag{3.50}$$

where we have dropped terms of $\mathcal{O}(dt)$ in Eqns. (3.3) and (3.4). Expanding to order dt yields Eq. 3.1

3.4 Solution to the Position Dependent Master Equation to $\mathcal{O}(\epsilon^2)$ in a Time-Dependent Force Field

We seek solutions to $\mathcal{O}(\epsilon^2)$ for the Master equation, in the presence of the arbitrary time-dependent force field of the form $F(x,t) = -x\,F_1(t) + F_0(t)$ is:

$$\partial_t P(x,v,t) = -\frac{1}{M}\left(-x\,F_1(t) + F_0(t)\right)\partial_v P(x,v,t) - v\,\partial_x P(x,v,t) - \tag{3.51}$$

$$\frac{\alpha_1^{(1)}}{M}\,\partial_v\left(\,v\,P(x,v,t)\right) + \frac{\alpha_2^{(0)}}{2M^2}\partial_v^2\left(\,P(x,v,t)\right). \tag{3.52}$$

This equation may be written in a more suggestive form a la [44] as

$$\partial_t P = -C_i(t)\partial_{x_i} P - A_{ij}(t)\partial_{x_i}\left(x_j\,P\right) + \frac{1}{2}B_{ij}\partial^2_{x_i x_j} P \tag{3.53}$$

where $P = P(\vec{x},t)$, $x_1 = x$, $x_2 = v$, and

$$C_i(t) = \begin{pmatrix} 0 \\ F_0(t)/M \end{pmatrix};$$

$$A_{ij}(t) = \begin{pmatrix} 0 & 1 \\ -F_1(t)/M & \alpha_1^{(1)}/M \end{pmatrix};$$

$$B_{ij}(t) = \begin{pmatrix} 0 & 0 \\ 0 & \alpha_2^{(0)}/M^2 \end{pmatrix}. \tag{3.54}$$

Making the substitution of $x_i = y_i + u_i(t)$ where $u_i(t)$ is the solution to $\dot{u} = A(t)u + C(t)$, the transformed expanded Master equation may now be written as

$$\partial_t P = -A_{ij}(t)\partial_{y_i}\left(y_j P\right) + \frac{1}{2}B_{ij}\partial^2_{x_i x_j} P. \tag{3.55}$$

The solution to such equations is well known in the literature [15] (and can be derived explicitly by a method of characteristics for the characteristic function of $P(\vec{x},t)$, $G(\vec{k},t)$) to be a Gaussian distribution with the following mean and covariance matrix

$$\langle y\rangle_t = Y(t)y_0; \tag{3.56a}$$

$$\Xi(t) = \int_0^t dt' Y(t)Y^{-1}(t')B(t')(Y^T)^{-1}(t')Y^T(t) \tag{3.56b}$$

where the matrix $Y(t)$ is known as the propagator and is the solution to the following differential equation

$$\dot{Y}(t) = A(t)Y(t); \qquad Y(0) = 1 \tag{3.57}$$

and y_0 is the value of y at $t = 0$.

Therefore the full probability distribution for P requires solving for $u(t)$, $Y(t)$ in Eqn. (3.57) for the appropriate $F_0(t)$ and $F_1(t)$ of interest, and then evaluating the integral in Eqn. (3.56b) to have a full expression for the covariance matrix. The full solution may be written as

$$P(\vec{y} = \vec{x} - \vec{u}(t), t) = (2\pi)^{-1} \left(\det \Xi(t)\right)^{-1/2} \exp\left[-\frac{1}{2}\left(y - \langle y\rangle_t\right)^T \Xi^{-1} \left(y - \langle y\rangle_t\right)\right]. \tag{3.58}$$

From here, we can compare the time-dependent force field solutions using a Kramers-Moyal expansion as opposed to our exact Master equation approach for the deviations from the Gaussian theory. We now proceed to continue our expansion of the Master equation and study the nature of higher order corrects in ϵ to see whether they can satisfy the necessary conditions for Maxwell-Boltzmann statistics to hold for the two noninteracting gasses at different temperatures.

3.5 $\mathcal{O}(\epsilon^4)$ calculation of $\mathcal{P}(v,t)$ in the two bath system

Expanding the Master equation to fourth order in ϵ^4 yields (once again using $v \to M^{1/2}v$ as in [1])

$$\begin{aligned}\partial_t \mathcal{P}(v,t) = &-\epsilon\,\partial_v\left(\alpha_1^{(0)}\mathcal{P}(v,t) + \epsilon\,\alpha_1^{(1)}\,v\,\mathcal{P}(v,t) + \frac{\epsilon^2}{2!}\,\alpha_1^{(2)}\,v^2\,\mathcal{P}(v,t) + \frac{\epsilon^3}{3!}\,\alpha_1^{(3)}\,v^3\,\mathcal{P}(v,t)\right) + \\ &\frac{\epsilon^2}{2!}\partial_v^2\left(\alpha_2^{(0)}\,\mathcal{P}(v,t) + \epsilon\,\alpha_2^{(1)}\,v\,\mathcal{P}(v,t) + \frac{\epsilon^2}{2!}\,\alpha_2^{(2)}\,v^2\,\mathcal{P}(v,t)\right) - \\ &\frac{\epsilon^3}{3!}\partial_v^3\left(\alpha_3^{(0)}\,\mathcal{P}(v,t) + \epsilon\,\alpha_3^{(1)}\,v\,\mathcal{P}(v,t))\right) \\ &\frac{\epsilon^4}{4!}\partial_v^4\left(\alpha_4^{(0)}\,\mathcal{P}(v,t)\right). \end{aligned} \tag{3.59}$$

We repeat the calculation of [36] for our two gas system and calculate the conditions necessary among the $\alpha_n^{(p)}$ in order for $P_{eq}(v)$ to be the Maxwellian distribution to fourth order in ϵ. After some lengthy calculations using arguments of microscopic reversibility as well as ensuring that the ϵ^4 terms cancel appropriately for the equilibrium solution of Eqn. (3.59), we can verify and restate the same relationships of [36]:

$$\mathcal{O}(\epsilon^2) = 2\,k_B T_{eq}\alpha_3^{(1)} + \alpha_4^{(0)} \tag{3.60}$$

$$\mathcal{O}(\epsilon^2) = \frac{1}{\epsilon^2}\left(k_B T_{eq}\,\alpha_1^{(1)} + \frac{\alpha_2^{(0)}}{2}\right) - \frac{k_B T_{eq}}{2}\alpha_2^{(2)} + \frac{1}{8\,k_b T_{eq}}\alpha_4^{(0)} \tag{3.61}$$

$$\mathcal{O}(\epsilon^2) = \alpha_1^{(3)} + \frac{3}{2\,k_B T_{eq}}\alpha_2^{(2)} - \frac{1}{4\,(k_B T_{eq})^3}\alpha_4^{(0)} \tag{3.62}$$

These relationships come with a caveat. They only hold true if all temperatures of the system (including those of the working gas mixtures) are equal to $k_B T_{eq}$ (This was the limit examined in [36]).

If the temperatures of the working gas mixtures are not all equal to the final equilibrium temperature of the ion, then the Maxwell distribution is not an equilibrium solution to Eqn. (3.59) as the relationships between the $\alpha_n^{(p)}$ to fourth order in ϵ do not hold for any temperature T_{eq}. The ϵ^3 relationships are trivially satisfied in the limit of symmetric left and right hand chambers. This result means that there must be another equilibrium distribution.

There is another problem however with Eqn. (3.59). As pointed out in [44] and [63], it is not possible to have a probability distribution that can be both normalized and be

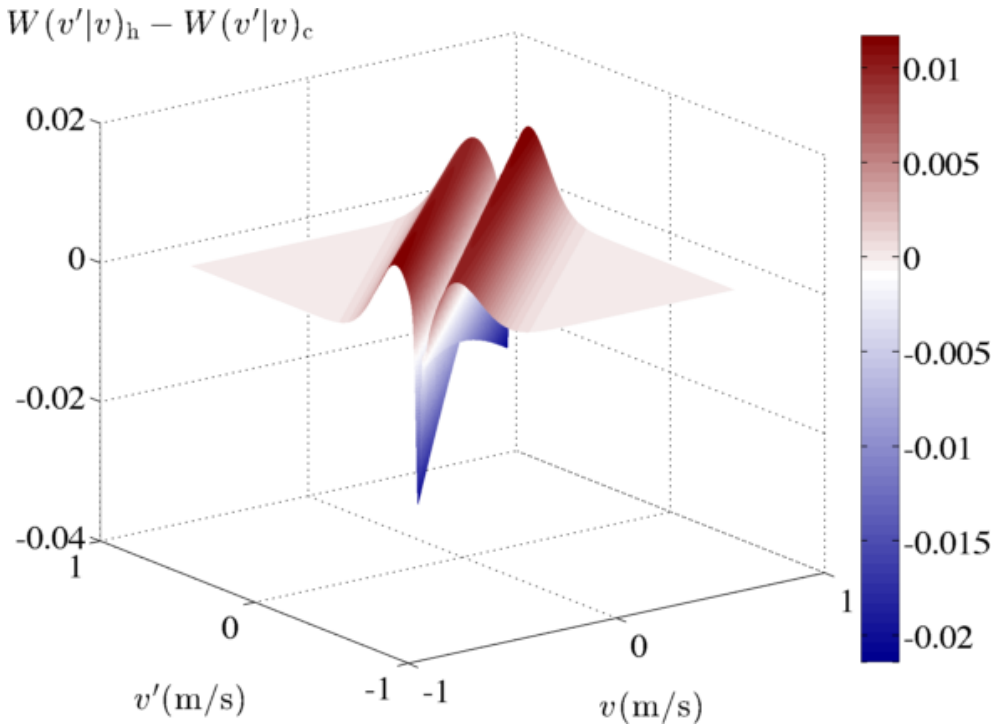

Figure 3.5.1: $W(v'|v)_h - W(v'|v)_c$ for a two buffer temperature buffer gas system where $T_h = 100\,T_c$ for $W(v'|v)_h$ and $T_h = T_c$ for $W(v'|v)_c$. The broad, positive set of transition rate differences corresponds to the hot gas allowing a great range of velocity transitions to happen. The narrow, negative set of transition rate differences corresponds to the fact that a single, cold temperature system favors a much narrower band of velocity transition rates.

nonnegative for all values of v that comes from an equation of the form of Eqn. (3.59). Hence if one wishes to calculate the probability distribution, one must treat terms of $\mathcal{O}(\epsilon^3)$ and above as a perturbation to the Master Equation of $\mathcal{O}(\epsilon^2)$. This is acceptable if there is only one temperature in the system. However, even this procedure breaks down in the presence of two separate buffer gas temperatures separated by a large temperature difference. This can be explained by examining Fig. 3.5.1. As one can see from Fig. 3.5.1, in the presence of two temperatures of buffer gasses, there are two scales by which the velocity transitions must be described, that set by the hot collisions and that set by the collisions. The broad, positive set of transition rate differences corresponds to the hot gas allowing a great range of velocity transitions to happen. The narrow, negative set of transition rate differences corresponds to the fact that a single, cold temperature system favors a much narrower band of velocity transition rates.

The $\alpha_n^{(p)}$ and their differential operators no longer serve as appropriate approximations to the original master equation in the two temperature limit. This can be easily seen by plugging in $kT_1 = 1$ and $kT_2 = 100$ in the appropriate units into the $\alpha_n^{(p)}$ of Eqn. (3.59) and find that the coefficient of the ∂_v^4 operator is of the same order of magnitude as the ∂_v^2 operator, which contradicts the original assumption of the Kramers-Moyal expansion of higher order terms being smaller than their predecessors in the expansion series.

Hence the correct equation to analyze in order to find the probability distribution for the ion in the presence of two buffer gasses at different temperatures is the original Master Equation of Eq. 3.1.

This also implies that the fluctuation-dissipation relationships such as those derived in Eqn. (3.62) to order to orders ϵ^2 and ϵ^4 no longer hold for the two temperature system. This can be easily explained by noting that the hot gas of the two buffer gasses must be pumping energy into the system in order to maintain its given temperature, meaning the ion-buffer gas system is out of thermal equilibrium.

3.6 Numerical Solution to Equations of Motion

We have now justified the need to solve the full Master equation in order to properly describe the statistics of the ion colliding with the two buffer gasses at different temperatures. However, this equation is analytically intractable unless the two temperatures of the gasses are equal hence we are forced to solve Eq. 3.1 numerically using semi-Lagrangian and quadrature methods [7] as described below.

3.6.1 Steady-State Distribution Calculation

In order to solve for the steady state distrbution of the two temperature buffer gas system, we must solve the full master equation. Given the difficulty of singular intergral equations, we are forced to make a numerical approximation to the solution. First we rewrite the Master equation using an integration factor i.e.

$$\partial_t \left(P(v,t) \, \exp(\mathcal{W}(v)\, t) \right) = f(v,t) \exp\left(\mathcal{W}(v)\, t\right) \tag{3.63}$$

where

$$f(v,t) = \int dv'\, W(v|v')P(v',t)\,;$$
$$\mathcal{W}(v) = \int dv'\, W(v'|v) \tag{3.64}$$

and $\mathcal{W}(v)$ can be evaluated exactly for both the elastic and Langevin collisions cross-sections to yield respectively

$$\mathcal{W}(v) = \sum_i c_i \frac{v}{2}\left(1 + \mathrm{erf}\left(\sqrt{\frac{m_i}{2\,k_B T_i}}v\right) - \mathrm{erfc}\left(\sqrt{\frac{m_i}{2\,k_B T_i}}v\right)\right)$$
$$+ c_i\sqrt{\frac{2k_B T_i}{\pi\, m_i}}\exp\left(-m_i\, v^2/2\,k_B T_i\right) \tag{3.65}$$

and the form of σ_L with $W(v'|v)$ now modifies $\mathcal{W}(v)$ for the Langevin cross-section to

$$\mathcal{W}_L = 2\pi\, c_i\, g\sqrt{\frac{C_4}{\mu}}. \tag{3.66}$$

Note that $\mathcal{W}_L$ is now velocity independent, meaning the rates of collision from the two gasses are constant and independent of one another. We use these collisions rates in our collision simulations to reproduce the velocity distribution calculated from the Master Equation.

The integration factor ensures a rapid convergence of our solution to the steady-state distribution (a generalization of [24] for a continuum of states). Integration of Eqn. (3.63) for a small time step Δt and making the assumption $f(v,t)$ is constant over this time interval yields

$$P(v,t+\Delta t) \approx \exp\left(-\mathcal{W}(v)\Delta t\right)P(v,t) +$$
$$\left(1 - \exp\left(-\mathcal{W}(v)\Delta t\right)\right)\frac{f(v,t)}{\mathcal{W}(v)}. \tag{3.67}$$

We use Eqn. (3.67) to find our steady state probability distribution $P_{eq}(v)$ such that $f(v) - \mathcal{W}(v)P_{eq}(v) \approx 0$. We plot such a time evolution in Figure 3.6.1

3.6.2 Semi-Lagrangian Advection Method

We solve the full time-dependent integro-differential Master equation using a Semi-Langrangian advection method using a three time step level algorithm as seen in [8].

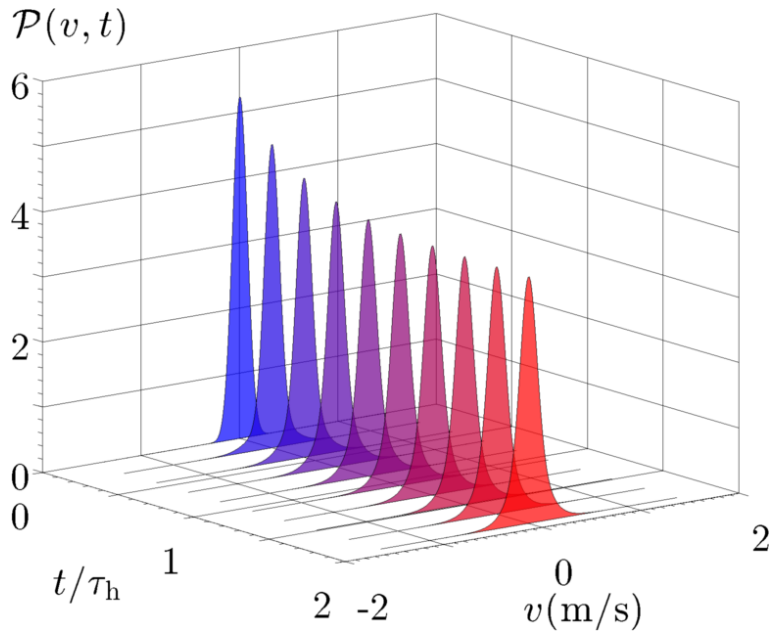

Figure 3.6.1: Time Evolution of the probability distribution of an ion experiencing elastic collisions with a hot and cold buffer gasses. Initial distribution is $\propto \exp\left[-Mv^2/2k_BT_{\rm c}\right]$. Time is measured in units $\tau_{\rm h}^{-1} = c_{\rm h}\sqrt{k_BT_{\rm h}/m_{\rm h}}$.

We merely restate the main results. We rewrite Eqn. 3.1 as

$$\frac{D}{Dt}P(x,v,t) = f(x,v,t) - \mathcal{W}(v)P(x,v,t) \tag{3.68}$$

where

$$\begin{aligned} f(x,v,t) &= \int dv'\, W(v|v')P(x,v',t)\,; \\ \frac{D}{Dt} &= \partial_t + v\,\partial_x + \frac{F(x,t)}{M}\,\partial_v = \partial_t + \vec{u}\cdot\vec{\nabla} \end{aligned} \tag{3.69}$$

The solution to the probability distribution at time $t+dt$ is found by solving the following system of equations

$$\begin{aligned} \frac{P^+ - P^-}{2\,\tau} + \frac{1}{2}\left(\mathcal{W}^+P^+ + \mathcal{W}^-P^-\right) &= f^0\,; \\ P^+ &= P(x,v,t^n+\tau); \\ P^0 &= P(x-\alpha_x, v-\alpha_v, t^n); \\ P^- &= P(x-2\,\alpha_x, v-2\,\alpha_v, t^n-\tau); \\ \alpha_j &= \tau u_j\left(x_j-\alpha_j, t^n\right) \end{aligned} \tag{3.70}$$

where τ is the size of the time step, $\vec{u}$ is the advection velocity in the $\{x,v\}$ space, and $\vec{\alpha}$ is the distance moved by a probability density point during the time step τ.

We plot the time-evolution of a ion in a steady state with a cold buffer gas solution in Fig. 3.6.1 where at $t = 0$ we introduce a hot buffer gas and allow the system to achieve a new steady-state. We use the elastic cross-section. As one can see there is a reduction in the low velocity states due to collisions with the hot buffer gas as well as an increase in the high velocity states, again due to collisions with the hot buffer gas.

3.6.3 Discussion of Results

Now that we have a method to arrive at solutions to Eq. 3.1,. We consider two forcing terms: (i) a simple harmonic trap $F = -k\,x$, and (ii) a simple model of the rf trap in one-dimension $F = -k\,x\cos(\Omega t)$.

In Fig. 3.2.1 we show the steady-state ionic velocity distributions for the various collision cross sections and forcings. These are calculated by evolving from an equilibrium distribution at $T_{\rm c} = (1/2)v^2 = 1$ (m/s)^2. We work in units where $k_{\rm B} = 1$ and amu $= 1$. After the hot buffer gas ($T_{\rm h} = 100\,T_{\rm c}$) is introduced, the initial ionic MB velocity distribution consistent with temperature $T_{\rm c}$ (blue, dashed line) broadens. After a few mean collision times with the hot buffer gas, it reaches the new steady-state non-MB velocity distribution (purple, solid line) having power-law high-velocity tails, which are significantly enhanced as compared to the $T_{\rm c}$-MB distribution. The nonequilibrium steady-state velocity distribution agrees with Monte Carlo simulations (open squares) of the system. The appearance of the power-law tails occurs in all cases including the rf trap with a Langevin ion-atom cross section (purple, solid line) or in a static trap with a simple geometric scattering cross section (red,dash-dotted line).

Such power-law tails were also reported [23] for an ion interacting with a single-temperature neutral buffer in an rf trap. Multiplicative noise associated with the stochastic (with respect to the rf phase) interruption of ionic micromotion alone can account for these [43]. Indeed, the high-velocity power-law tails that we observe in the *absence of micromotion* are strongly enhanced in our model of the rf trap (dotted, green line), so a variety of nonequilibrium forcing methods generate this particular feature.

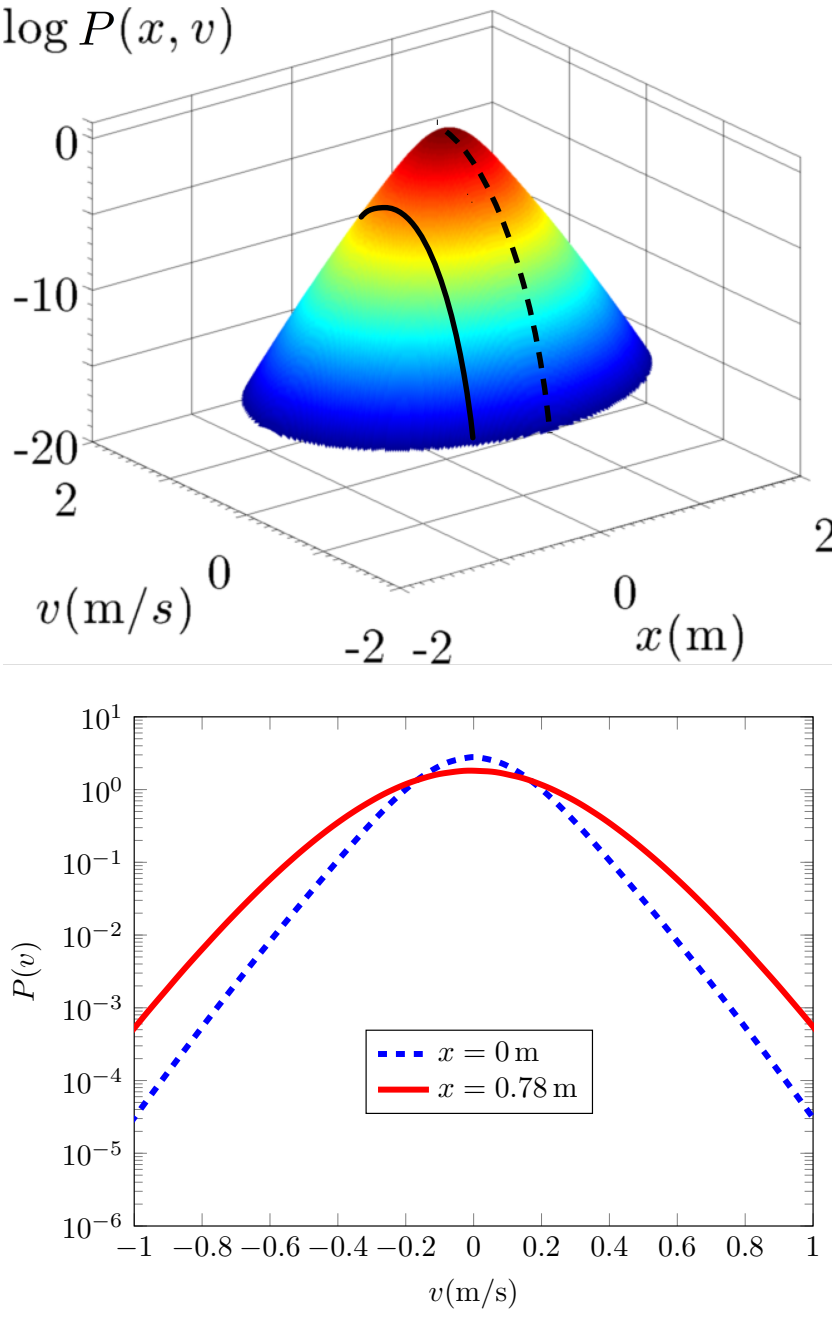

Figure 3.6.2: Top: Steady state probability distribution $P(x, v)$ in the same two-temperature buffer gas – Fig. 1 – and in a static harmonic potential, with spring constant $k_0 = 100\,\mathrm{s}^{-2}$. Bottom: Comparison of the velocity distributions at different positions (shown by the solid and dashed lines in the top figure), showing position-velocity sorting.

3.6.4 Failure of Maxwell-Boltzmann Statistics

One of the foundational principles of classical statistical mechanics is that the joint probability distribution of the position and momentum degrees of freedom factorizes: $P(x, v) = \mathcal{P}(v; T)\mathcal{P}(x; T)$ – e.g., an isothermal gas in a gravitational field has the same MB velocity distribution at each height even though its density decreases with height. This factorizibility does not survive in the nonequilibrium system of current interest. In Fig. 3.6.2 (upper panel) we plot the ionic steady-state joint probability distribution $P(x, v)$ in a static harmonic trap [13], with spring constant $k_0 = 100$ s^{-2}. In the lower panel, we consider two normalized velocity distributions at different positions: $x_1 = 0$ (blue, dashed) and $x_2 = 0.78$ m (red, line) in the static trap, and see that the high-velocity states are over represented at higher potential energy (red, line) relative to those at zero potential energy at x_1. This demonstrates that the joint probability distribution is non-factorizible – a feature we term *position-velocity sorting.* Conversely, integrating over all velocities at a given x to obtain the spatial distribution, one finds that the potential energy microstates are not populated according a Boltzmann relation $\sim \exp[-U(x)]$. We speculate that position-velocity sorting arises from the fact that rare hot atom collisions with the ion typically drive it simultaneously to high velocity states and out of the center of the trap, leading to a nonequilibrium correlation between fast states and high potential energy ones.

The nonequilibrium ionic spatial probability distribution in an rf trap, shown in Fig. 3.6.3, is similar to that predicted for the static trap – see Fig. 2. In both cases the high potential energy states are overrepresented in the form of power-law tails. The one-dimensional calculation (solid, black line) based on Eq. 1 provides a good fit to the distribution of the ion's z coordinate as computed from a molecular dynamics simulation of a three-dimensional rf trap with the two-temperature buffer, using experimental realizable parameters from the full three-dimensional molecular dynamics simulation of the trapped ion [17], which has been verified against the experimental system. To compare the one-dimensional theory to three dimensional simulation, we adjusted the one-dimensional buffer concentrations in the calculation as a single fitting parameter.

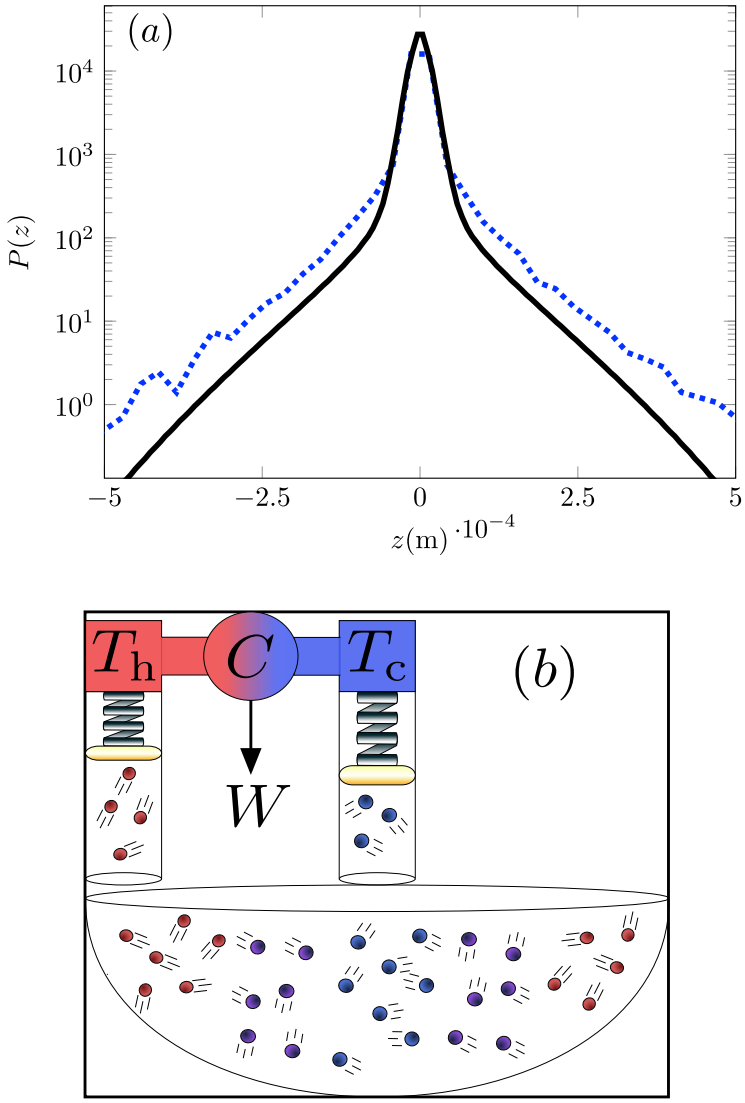

Figure 3.6.3: (a) Ionic vertical position distribution $P(z)$ in an rf trap computed from a 3D molecular dynamics simulation (blue, dashed) and from the 1D master equation (black, solid) using the same simulation parameters for the trap and collision cross section. 1D buffer concentrations were adjusted as a free parameter but the ratio $c_\mathrm{h}/c_\mathrm{c} = 10^{-2}$ was fixed by simulation parameters. (b) Schematic Carnot engine used to extract work from the position-velocity sorted state.

3.6.5 Extraction of work from the system

Because of position-velocity sorting, it is, in principle, possible to extract free energy from the system to run a heat engine. For this to happen one needs a nonequilibrium system that also breaks a spatial symmetry to generate the directional movement necessary to do work on its surroundings. An example is a molecular motor [42] in which the chemical potential difference between ATP and ADP can generate work only if the motor interacts with a directional track (e.g. F-actin) breaking inversion symmetry. We find that, for an ion in the two-temperature buffer, *both the static and rf harmonic traps* provide the necessary symmetry breaking to generate work via *position-velocity sorting*.

In Fig. 3.6.3 (b) we show a schematic representation of a Carnot engine (CE) extracting energy out of the trapped ion system to generate work. No equilibrium system, such as the thermal reservoirs of the CE, can come into equilibrium with the nonequilibrium steady-state of the ion. Rather, we imagine two thin wires coming from the hot and cold thermal reservoirs of the CE allowing energy and momentum exchange with an ensemble of ions at the edge and the center of the static trap, respectively. Momentum transfers between the wire and ion are balanced by the wires' elastic deformation, represented by springs. The temperatures of two reservoirs are adjusted so that the net energy transfer vanishes between them and the ensemble of ions. If these were two equilibrium systems, such a balance would imply equal temperatures and pressures, but neither thermodynamic variable is meaningful for the ion. Nevertheless, the vanishing net energy flow between the two thermal reservoirs and the ionic ensemble allows us to assign nominal temperatures to both of them. When computed this way, the temperature of the hot reservoir in thermal contact with the edge of the trap is greater than that of the cold reservoir in thermal contact at the trap center. It is then possible to generate work in the usual way. For the buffer gas parameters used in Fig. 2 (cold reservoir at $x = 0\,\mathrm{m}$; hot reservoir at $x = 0.39\,\mathrm{m}$) we find a thermodynamic efficiency of 0.166.

3.6.6 Violations of the fluctuation-dissipation theorem

Another robust feature of equilibrium systems is the relation between their fluctuations and linear response, known as the fluctuation-dissipation theorem (FDT) [14]. In some

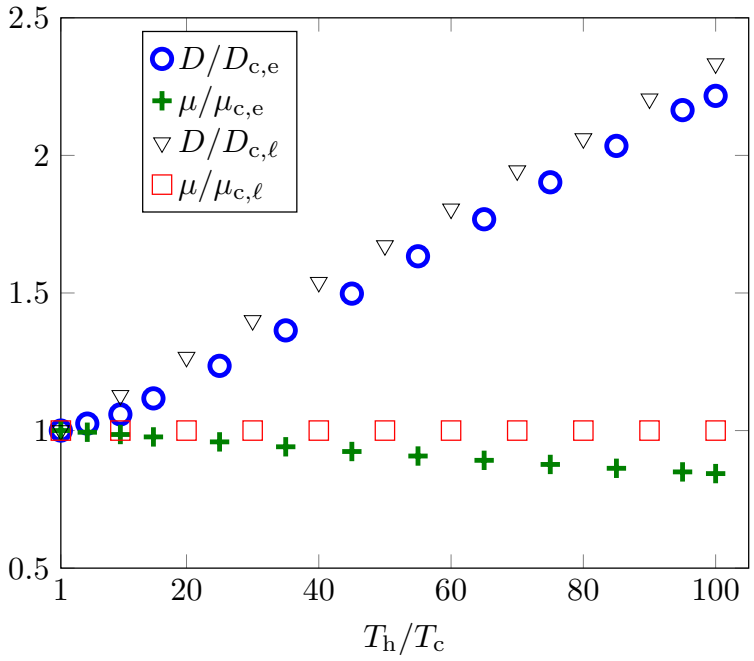

Figure 3.6.4: Comparison of the ion diffusivities and mobilities in a two-temperature buffer for a geometric (e) and Langevin (ℓ) atom-ion cross sections. We drive the system from equilibrium by controlling $T_\mathrm{h}/T_\mathrm{c}$. Diffusivities and mobilities are normalized by their equilibrium values: $D_{\mathrm{c,i}}$ and $\mu_{\mathrm{c,i}}$ respectively, $\mathrm{i} = \mathrm{e}, \ell$.

active matter systems of biological interest, the breakdown of the FDT is used as an indicator of nonequilibrium physics associated with endogenous molecular motor activity [59, 56]. Unlike in that system, however, the two-temperature buffer gas provides a simple and independent control on the nonequilibrium nature of the system – the temperature of the hot gas. As T_h is reduced to T_c, the system must return to equilibrium.

The FDT implies a relation between the mean ionic velocity in the presence of a static electric field and its diffusion in the absence of one. We test this Einstein relation by applying a constant force $U = -F_0\, x$ and determining the mean ionic velocity in steady-state. By examining the the ratio of that ionic mean velocity to the applied force in the linear response regime, one extracts the ionic mobility μ. Alternatively, by placing the ion at a given initial location and examining the spread of its spatial probability distribution *without an applied force*, one obtains the ionic diffusion constant from $D = \lim_{t\to\infty}\langle x^2\rangle/2\,t$.

Figure 3.6.4 shows μ and D as a function of the buffer gas temperature ratio $T_\mathrm{h}/T_\mathrm{c}$,

used to control the nonequilibrium steady-state. Both μ and D separately normalized by their equilibrium values, computed by setting the buffer gas temperatures to be equal: $T_\mathrm{h} \to T_\mathrm{c}$. As the temperature of the hot buffer gas is increased to drive the system from equilibrium, the ionic diffusivity D increases roughly linearly. We attribute this to the higher occupation probabilities of high velocity states. Though rare, collisions with the hot atoms enhance ionic diffusion relative to its equilibrium value at $T_\mathrm{h} = T_\mathrm{c}$. For the geometric collision cross section μ decreases since the ion's collision rate with the buffer gas increases with relative velocity. For the Langevin cross section, μ is constant because the collision rate is independent of the relative velocities of the ion and the buffer atoms. The Einstein relation breakdown due to the presence of even a low concentration of a hot buffer gas makes the analysis of charge transport in cold plasmas [18] more difficult, requiring one to independently consider diffusivity and mobility.

3.7 Experimental Suggestions

We have shown that, due to the combination interactions with a hot and cold neutral buffer gas, the ionic joint probability distribution for position and velocity in a trap shows a number of striking nonequilibrium features that can be quantitatively controlled by the temperature difference between the two buffers. In addition, ionic conductivity and diffusion should demonstrate marked departures from the FDT. Experimental observation of these effects is, in principle, straightforward. A single ion can be prepared at the center of a linear quadrupole trap with weak axial confinement by strong laser cooling. The ion can be released by extinguishing the laser cooling, allowing the ion to interact with the buffer gases and thereby explore the system phase space. After an evolution time, the ion's position can be measured using radial ejection [69, 76] from the ion trap onto an imaging micro-channel plate (MCP). By repeating the experiment, the probability distribution of the ion's position and analogs of the diffusion constant can be measured, as well as their dependence on the experimental parameters, such as buffer gas temperature and density, explored. Further, it may be possible to use a retarding potential in front of the MCP, or a variation of velocity map ion imaging [80], to measure the ion's kinetic energy as a function of trap position to explore position-velocity sorting. It may also be possible

to build up the ion position distribution by stroboscopic laser imaging, as long as the duty cycle is low enough to not significantly affect ion dynamics. Finally, using the same system, the laser cooling can be adjusted to prepare the ion with a displacement from the trap minimum. By monitoring the transport of the ion in response to the axial trapping force analogs of the ion mobility can be measured.

CHAPTER 4

2 Harmonically Coupled Particles in Non-Gaussian White Noise

4.1 Introduction

The study of the effect of multiple white noise sources on a stochastic system was explored in the first part of Chapter 3, however we found there that this method of describing stochastic fluctuations was inaccurate to describe the system in the presence of two fluctuation sources when the two noise sources have large differences between the size of transitions they may induce upon the stochastic system, in the case of Chapter 3, the velocity and position transitions of an ion in a time-varying harmonic trap. Instead, we were able to study the ions' velocity and position distribution exactly using a Master equation approach by solving the Master equation numerically, circumventing the analytic difficulty of a closed, algebraic solution.

However the study of phase spaces corresponding to the stochastic dynamics of multiple particles becomes even numerically untameable to solve as the number of dimensions in the phase spaces grows as N, where N is the number of particles in the system. For example, to achieve the same numerical resolution as the probability density calculations of Chapter 3 for a two dimensional system consisting of two particles, one would have to do an order of 10^{18} calculations per time step to solve the joint position-velocity distribution for the two particles. Only the fastest computers on the planet at the moment could handle such calculations. in a reasonable frame of time.

Hence as discussed in Chapter 1, we seek a different method to describe transitions in stochastic systems with non-Gaussian, white noise. The non-Gaussian part of the noise allows us to describe a much more broad class of transitions that cannot be approximated by a simple Fokker-Planck equation, but rather requires an infinite set of terms for the

time-dependent partial differential equation describing the time evolution of the conditional probability as demonstrated in Chapter 1. The system we choose to study is a two particle system as shown in Figure 4.1.1 that consists of the two particles being harmonically coupled to each other as well as being coupled to two walls which can compress the system on either side of the particles by a distance b, with a harmonic restoring force in the $\hat{y}$ direction whose magnitude in response is independent of the $\hat{x}$ position of the particles

This system is interesting as it exhibits a second-order, mechanically induced phase transition in the deflection field of the particles in the absence of thermal fluctuations. For small compression of the walls, i.e. small b, the deflection field of the particles is a symmetric compression along the $\hat{x}$ directions. However, as the compression from the walls increases, rather than continue to deflect only along the $\hat{x}$ direction, the system seeks a global minimum in the potential energy by allowing anti-symmetric deflections in the $\hat{y}$ direction as shown in Figure 4.1.1. We are interested in how this mechanical system responds to both Gaussian and non-Gaussian noise near this mechanical transition, and whether one type of noises effect is amplified near this transition as opposed to another.

We study this two particle system as it is experimentally realizable given the recent advancements in Penning trap experiments such as those found in [74], which allow for the formation of Coulombic crystals, a system analogous to the one explored here. We will begin this chapter by first simplifying the equations of motion in the small deflection limit, near the equilibrium configuration of the particles in the absence of fluctuations. We will then outline in detail the functional form of the non-Gaussian, white noise fluctuations of interest, as well as their physical interpretation. Finally we solve the equations of motion in a perturbative, diagrammatic manner, and calculate the two-point function to one-loop order for the system, discussing the diffierences between terms in the correlation function arising from Gaussian and non-Gaussian fluctuations.

4.2 The Model

We begin our study of the effect of non-Gaussian, white noise on the two particles harmonically coupled to each other and to two walls. The Hamiltonian for the system is

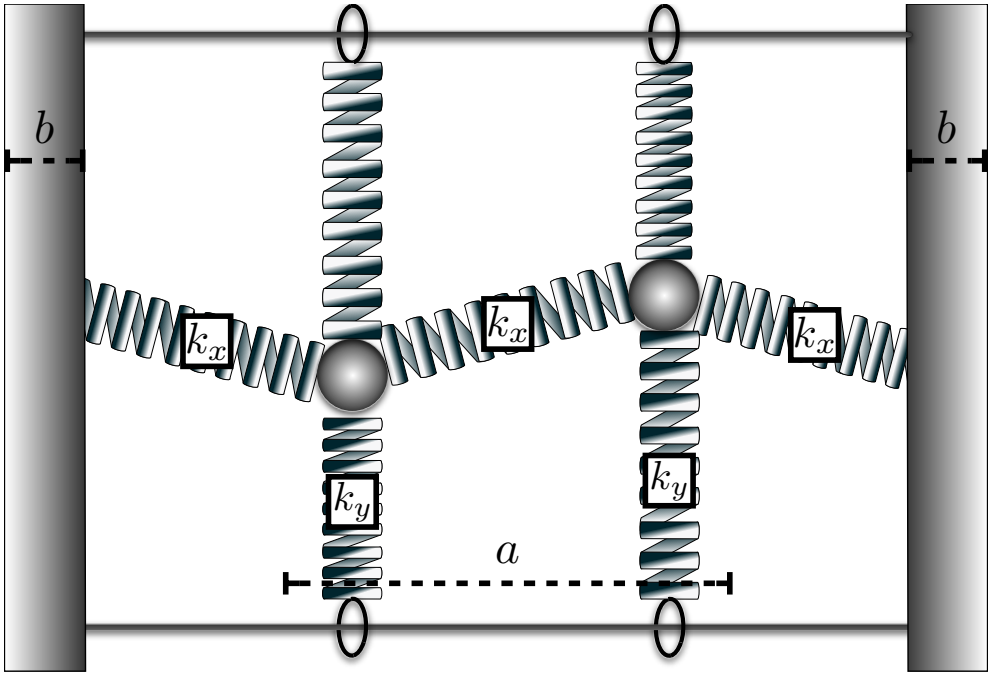

Figure 4.1.1: Schematic of the System to be studied in the presence of non-Gaussian white noise

given by

$$\begin{aligned} H =& \frac{1}{2}\, m\, \dot{\vec{x}}_1^{\,2} + \frac{1}{2}\, m\, \dot{\vec{x}}_2^{\,2} + \frac{1}{2} k_y \left(y_1^2 + y_2^2\right) + \\ & \frac{1}{2} k_x \left((|\vec{x}_2 - \vec{x}_1| - a)^2 + (|\vec{x}_1 - \vec{b}_1| - a)^2 + (|\vec{x}_2 - \vec{b}_2| - a)^2 \right) \end{aligned} \tag{4.1}$$

where $\vec{x}_i = \{x_i, y_i\}$ is the two-dimensional position vector of the i^{th} particle, a is the rest spacing between the particles, $\vec{b}_1$, the locations of the walls on both sides of the particles, m is the mass of the particles, and $k_{x/y}$ are spring constants characterizing the strength of the potential in which the particles are embedded in.

First we examine the Hamiltonian in the absence of the Non-Gaussian white noise in order to have an idea of where to expand the potential energy about to study the motion of the system in the presence of the non-Gaussian white noise. Note that the Hamiltonian is nonlinear in the positions of the particle, and intractable to solve analytically, hence why an expansion of the equations of motion is necessary. Using physical intuition, one can convince themselves that the equilibrium position of the two particles must go through two separate mechanical phases depending on how much the walls have been compressed on both sides of the particles. The first phase consists simply of the two particles being compressed along the $\hat{x}$ direction with no deflection in the $\vec{y}$ direction. The equilibrium

positions for the particles in this limit are $\vec{x}_1 = \{-a/2+b/3, 0\}$ and $\vec{x}_2 = \{a/2-b/3, 0\}$ as can be easily seen by solving for the appropriate minimum of the potential energy of the system. The second mechanical phase happens for much larger compressions of the walls b, and leads to an antisymmetric mode with equal in magnitude and opposite direction deflection for the $\vec{x}$ and $\vec{y}$ positions of the particles. This soft mode phase cannot be solved for using standard analytic methods, but has been verified using numerical minimization procedures.

Given that we are interested in examining the two particle system near this transition point in the presence of non-Gaussian fluctuations, we choose to expand the potential about the first set of equilibrium positions and examine the equations of motion for each of particle coordinates the presence of an isotropic damping $2\,\Gamma$. The equations of motion for the two particle's x and y coordinates are

$$
\begin{aligned}
m\,\ddot{x}_1 + 2\,\Gamma\dot{x}_1 =& -k_x \left(\frac{(\frac{3a}{2} - b + x_1)(-a + \sqrt{(\frac{3a}{2} - b + x_1)^2 + y_1^2}\,)}{\sqrt{(\frac{3a}{2} - b + x_1)^2 + y_1^2}} \right. \\
& \left. - \frac{(x_2 - x_1)(-a + \sqrt{(x_2 - x_1)^2 + (y_2 - y_1)^2})}{\sqrt{(x_2 - x_1)^2 + (y_2 - y_1)^2}} \right) \\
m\,\ddot{x}_2 + 2\,\Gamma\dot{x}_2 =& -k_x \left(-\frac{(\frac{3a}{2} - b - x_2)(-a + \sqrt{(\frac{3a}{2} - b - x_2)^2 + y_2^2}\,)}{\sqrt{(\frac{3a}{2} - b - x_2)^2 + y_2^2}} \right. \\
& \left. + \frac{(x_2 - x_1)(-a + \sqrt{(x_2 - x_1)^2 + (y_2 - y_1)^2})}{\sqrt{(x_2 - x_1)^2 + (y_2 - y_1)^2}} \right) \\
m\,\ddot{y}_1 + 2\,\Gamma\dot{y}_1 =& -k_y\,y_1 - k_x \left(\frac{y_1(-a + \sqrt{(\frac{3a}{2} - b + x_1)^2 + y_1^2}}{\sqrt{(\frac{3a}{2} - b + x_1)^2 + y_1^2}\,)} \right. \\
& \left. - \frac{(y_2 - y_1)(-a + \sqrt{(x_2 - x_1)^2 + (y_2 - y_1)^2})}{\sqrt{(x_2 - x_1)^2 + (y_2 - y_1)^2}} \right) \\
m\,\ddot{y}_2 + 2\,\Gamma\dot{y}_2 =& -k_y\,y_2 - k_x \left(\frac{y_2(-a + \sqrt{(\frac{3a}{2} - b + x_1)^2 + y_2^2}}{\sqrt{(\frac{3a}{2} - b + x_1)^2 + y_1^2}\,)} \right. \\
& \left. + \frac{(y_2 - y_1)(-a + \sqrt{(x_2 - x_1)^2 + (y_2 - y_1)^2})}{\sqrt{(x_2 - x_1)^2 + (y_2 - y_1)^2}} \right).
\end{aligned}
$$

The x coordinates of the two particles near the soft-mode/strictly $\hat{x}$ compressional phase may be written in terms of their small deflections about the $\hat{x}$ compressional phase as $x_1(t) = -a/2 + b/3 + \epsilon_1(t)$ and $x_2(t) = a/2 - b/3 + \epsilon_2(t)$. The $\hat{y}$ deflections are small in

this limit as well. Hence we may do an expansion of the equations of motion assuming $\epsilon_i(t)$ and $y_i(t)$ are both small. In addition this, a great simplification to the equations of motions happens when we go from the actual coordinates of the particles to the symmetric and antisymmetric modes of the $\hat{x}$ and $\hat{y}$ deflections. These modes may be written as $s_x(t) = (\epsilon_1(t)+\epsilon_2(t))/2$ for the symmetric $\hat{x}$ mode, $as_x(t) = (\epsilon_1(t)-\epsilon_2(t))/2$ and similarly for $s_y(t)$ and $as_y(t)$. The new equations of motion from the potential written in the limit of a small deflection fields in the presence of the non-Gaussian white noise are

$$\begin{aligned}
m\,\ddot{s}_x + 2\,\Gamma\dot{s}_x + k_x s_x =& f_{sx} - \frac{9\,a\,k_x}{4(3a-2b)^2} 2\,as_y\,s_y \\
&- \frac{27\,a\,k_x}{4(3a-2b)^3}\left(-\,as_y^2\,s_x - 2\,as_x\,as_y\,s_y\right. \\
&\left. - s_x\,s_y^2\right) \\
m\,\ddot{as}_x + 2\,\Gamma\dot{as}_x + 3\,k_x\,as_x =& f_{ax} - \frac{9\,a\,k_x}{4(3a-2b)^2}(-3as_y^2 + s_y^2) \\
&- \frac{27\,a\,k_x}{4(3a-2b)^3}\left(-2\,as_y\,s_x\,s_y\right. \\
&\left. -as_x(9\,as_y^2 + s_y^2)\right) \\
m\,\ddot{s}_y + 2\,\Gamma\dot{s}_y + \left(k_y - \frac{2\,k_x\,b}{3a-2b}\right) s_y =& f_{sy} - \frac{9\,a\,k_x}{4(3a-2b)^2}(2as_y s_x + 2as_x s_y) \\
&- \frac{27\,a\,k_x}{4(3a-2b)^3}\left(-2\,as_y\,s_x\,as_x - as_x^2 s_y\right. \\
&\left. +\frac{3}{2}as_y^2 s_y - s_x^2 s_y + \frac{1}{2}s_y^3\right) \\
m\,\ddot{as}_y + 2\,\Gamma\dot{as}_y + \left(k_y - \frac{6\,k_x\,b}{3a-2b}\right) as_y =& f_{ay} - \frac{9\,a\,k_x}{4(3a-2b)^2}(-6as_x as_y + 2s_y s_x) \\
&- \frac{27\,a\,k_x}{4(3a-2b)^3}\left(-9\,as_y\,as_x^2 - s_x^2 as_y\right. \\
&\left. +\frac{9}{2}as_y^3 - 2as_x s_x s_y + \frac{3}{2}as_y s_y^2\right)
\end{aligned} \tag{4.2}$$

where $f_{sx} = f_{1x} + f_{2x}$ and $f_{ax} = f_{1x} - f_{2x}$ are the components of the non-Gaussian noise acting on the individual particles in the $\hat{x}$ directions. Similar expressions hold for the f_{sy} and f_{ay} forcing terms.

Immediate inspection of Eq. 4.2 for the s_y and as_y mode reveals that our physical intuition regarding the equilibrium positions was correct. For a critical amount of compression from the walls, b, we find that the effective spring constant in the $\hat{y}$ direction goes from having a positive to negative value. This is the origin of the soft mode due to compression

and has a larger effect on the as_y mode as opposed to the s_y as expected. The critical value for b for which the as_y spring constant goes to zero is $b_c = 3\,a\,k_y/(2(3\,k_x + k_y))$ for the linearized theory of the two particles. We analyze the equations of motion near this level of wall compression below.

4.3 Non-Gaussian, White Noise

Before solving the equations of motion, we must first specify the exact nature of our white noise terms in our problem. We define our Langevin forces at the different sites to be composed of two separate terms i.e. $\vec{f_1} = \vec{f}_{1g} + \vec{f}_{1d}$,where 1 refers to the noise at particle 1, g refers to the Gaussian part of the noise spectrum that follows the typical statistics[1] and d refers to the non-Gaussian part of the white noise. We take this part of the noise to have a Dirac Delta function probability density for its magnitude in its jumps and to be isotropic in the $\{x, y\}$ directions.

The probability distribution for $\vec{f_d}$ does not have the simple properties of averaging that Gaussian, white noise sources have for higher order cumulants and hence will lead to different averaging statistics for the solutions of Eq. 4.2 than those normally studied for white, Gaussian noise. We take the moments for this type of noise to come from a compound Poisson processes a la Snyder[71] where they can be described via their integrated process i.e. we describe the probability distribution of the following quantity:

$$\vec{Z}(t) = \int_0^t \mathrm{d}t' \vec{f}_d(t'). \tag{4.3}$$

Since $\vec{f_d}(t)$ is temporally uncorrelated, this means that the increments of $\vec{Z}$ i.e. $\vec{z} = \vec{Z}(t_2) - \vec{Z}(t_1)$ i.e. the momentum influxes into the two particle system, are independent of one another, and hence, we must simply describe the probability distributions of these increments to describe the non-Gaussian part of the noise.

The distribution for z consisting of n of increments in an interval τ is Poissonian with average $\rho\,\tau$ where ρ is a constant density of increments on the time axis. The increment $\vec{z}$ is the sum of these n jumps, with $\vec{Z}$ jumping by an amount $\vec{z}$ with a probability

[1] $P[\vec{f}_{1g}(t)] = \mathcal{N}\mathrm{e}^{-\frac{1}{2D}\int dt \vec{f}_{1g}(t)^2}$ where $\mathcal{N}$ is a normalization constant for the functional probability distribution

distribution $w(\vec{z})$. Hence the distribution of $\vec{z}$ is

$$T_\tau(\vec{z}) = \sum_{n=0}^{\infty} \frac{\rho\,\tau}{n!} \exp\left[-\rho\,\tau\right] w(\vec{z}) * w(\vec{z}) ... * w(\vec{z}) \tag{4.4}$$

where the product is the convolution of n factors of w and $T_\tau(z)$ has the same meaning as it did in Chapter 1. The characteristic function of $T_\tau(z)$ is hence given by

$$\int \mathrm{d}\vec{z}\, \mathrm{e}^{i\,\vec{k}\cdot\vec{z}} T_\tau(\vec{z}) = \exp\left[\rho\tau \int \mathrm{d}\vec{z} (\mathrm{e}^{i\,\vec{k}\cdot\vec{z}} - 1) w(\vec{z})\right] \tag{4.5}$$

which in turn yields the moments of the distribution of

$$\Gamma_m = \rho \int \mathrm{d}\vec{z}\, \vec{z}^{\,m}\, w(\vec{z}) \tag{4.6}$$

where the Γ_m are symmetric tensorial objects with m indices. The cumulants of $\vec{f}_d$ can now be calculated in a straightforward manner in both the time and frequency domain as

$$\langle\langle \vec{f}_d(t_1)\vec{f}_d(t_2)\cdots\vec{f}_d(t_m)\rangle\rangle = \Gamma_m \delta(t_1-t_2)\delta(t_1-t_3)\cdots\delta(t_1-t_m) \tag{4.7}$$

by definition of a white noise process.

The probability distribution $w(\vec{z})$ as described above is $\delta(|\vec{z}| - z_0)$. Here we give the most important averages over the noise in the frequency space for the four noise terms in Eq. 4.2:

$$\begin{aligned}
\langle f_{sx}(\omega) f_{sy}(\omega')\rangle =& 0 \\
\langle f_{sx}(\omega) f_{sx}(\omega')\rangle =& \langle (f_{1x}(\omega) + f_{2x}(\omega))(f_{1x}(\omega') + f_{2x}(\omega'))\rangle \\
=& \langle (f_{1x}(\omega) f_{1x}(\omega') + f_{2x}(\omega) f_{2x}(\omega'))\rangle \\
=& \langle (f_{1xg}(\omega) f_{1xg}(\omega') + f_{1xd}(\omega) f_{1xd}(\omega') + \\
& f_{2xg}(\omega) f_{2xg}(\omega') + f_{2xd}(\omega) f_{2xd}(\omega'))\rangle \\
=& 4\pi\delta(\omega+\omega')(D+\Gamma_2) \\
\langle f_{sx}(\omega) f_{sx}(\omega') f_{sy}(\omega''') f_{sy}(\omega'''')\rangle =& \langle f_{sx}(\omega) f_{sx}(\omega')\rangle \langle f_{sy}(\omega''') f_{sy}(\omega'''')\rangle \\
\langle f_{sx}(\omega) f_{sx}(\omega') f_{sx}(\omega''') f_{sx}(\omega'''')\rangle =& 4\pi\Gamma_4\delta(\omega+\omega'+\omega''+\omega''') + \\
& ((4\pi)(D+\Gamma_2))^2 (\delta(\omega+\omega')\delta(\omega''+\omega''') + \\
& \delta(\omega+\omega'')\delta(\omega'+\omega''') + \delta(\omega+\omega''')\delta(\omega'+\omega'')).
\end{aligned} \tag{4.8}$$

where $\Gamma_2 = z_0^2/2$ and $\Gamma_4 = 3z_0^4/8$. Identical quadratic and quartic averages exist for the other forces of the modes and combinations of the modes. We point out the newest feature of our averaging different than white, Gaussian noise is the term proportional to Γ_4, which will lead to novel loop integrals that those associated with white, Gaussian noise in our diagrammatic analysis. These moments of the forces will become important when calculating solutions to the equations of motion and correlation functions to one-loop order, which we explore next.

4.4 Fourier Transform of the Equations of Motion and Feynman Diagrams

In order to study the solutions to the equations of motion, we proceed via a perturbative analysis. We justify this perturbative expansion by examining the coefficients of the terms that are quadratic and cubic in the deflection fields in the equations of motion. Since we are primarily interested in the regime between the symmetric $\hat{x}$-compression mode and the antisymmetric $\hat{y}$ mode due to the compression from the walls, we set $b = b_c$. In this limit, the coefficient of the quadratic and cubic terms in the equations of motion respectively are $(3\,k_x + k_y)^2/36\,a\,k_x$ and $(3\,k_x + k_y)^3/108\,a^2\,k_x^2$ which both have prefactors less than 1 in magnitude. Hence, a perturbative expansion is indeed justified near the mechanical transition, meaning we may expand the non-linear solutions to the equations of motion in terms of the solutions of the equations of motion to linear order.

We Fourier transform the equations from the time to frequency space[2] and solve the equations of motion in the frequency space. For the sake of space, we rewrite only the equation of motion for the $as_x(\omega)$ function, as all other deflection fields follow in a similar

[2]We use the following normalization for our Fourier transforms: $f(\omega) = \int \mathrm{d}t\, \mathrm{e}^{i\omega t} f(t)$ and $f(t) = \int \frac{\mathrm{d}\omega}{2\pi}\, \mathrm{e}^{-i\omega t} f(\omega)$

fashion:

$$
\begin{aligned}
as_x(\omega) =& G_{ax}(\omega) f_{ax} \\
&- \lambda_1 \, G_{ax}(\omega) \int \frac{\mathrm{d}\omega'}{2\pi} 2\pi\delta\left(\omega - (\omega' + \omega'')\right) \left(-3as_y(\omega')as_y(\omega'') + s_y(\omega')s_y(\omega'')\right) \\
&- \lambda_2 \, G_{ax}(\omega) \int \frac{\mathrm{d}\omega'}{2\pi} \frac{\mathrm{d}\omega''}{2\pi} \frac{\mathrm{d}\omega'''}{2\pi} 2\pi\delta\left(\omega - (\omega' + \omega'' + \omega''')\right) \left(-2\, as_y(\omega')s_x(\omega'')s_y(\omega''')\right. \\
&\left. -as_x(\omega')(9\, as_y(\omega'')as_y(\omega''') + s_y(\omega'')s_y(\omega'''))\right) \qquad (4.9)
\end{aligned}
$$

where $G_{ax} = \left(-m\,\omega^2 - 2\,i\,\omega\,\Gamma + 3\,k_x\right)^{-1}$, $\lambda_1 = 9\,a\,k_x/(4(3a-2b)^2)$, and $\lambda_2 = 27\,a\,k_x/(4(3a-2b)^3)$. It becomes apparent that there are repetitive elements to the solutions to the equations of motion if a perturbative expansion is done, making them amenable to a diagrammatic analysis [30, 58].

In Fig. 4.4.1, we represent the equation of motion for the s_x mode in Fourier space using said diagrammatic representation. The rules to interpret the diagrams are the following:

- Double lines signify a complete solution to the equations of motion for the labeled field.
- Single lines represent the G_i for the appropriate i, in the case of Fig. 4.4.1, s_x.
- An $\times$ signifies the appropriate force for the attached single line, in this case f_{sx}.
- Arrows pointing to the right signify a positive frequency; to the left, a negative frequency. There are delta functions in frequency at the vertices.
- A vertex with a backslash pattern means $\lambda_1 \int \frac{d\omega'}{2\pi}\frac{d\omega''}{2\pi} 2\pi\delta(\omega - (\omega' + \omega''))$.
- A vertex with a hash pattern means $\lambda_2 \int \frac{d\omega'}{2\pi}\frac{d\omega''}{2\pi}\frac{d\omega'''}{2\pi} 2\pi\delta(\omega - (\omega' + \omega'' + \omega'''))$.

Diagrams can be made for all the equations of motion using these rules, meaning a perturbative expansion of the solutions to the equations of motion amounts to nothing more than an exercise in algebra and some straightforward calculus and complex analysis to evaluate the convolution integrals associated with the vertices and force averaging, which we proceed to evaluate next.

4.4.1 Correlation Functions

We seek to calculate the correlation functions between the modes of our system using solutions from the equations of motion. Given that the force terms for the different modes are uncorrelated, the correlation functions between different modes average to zero i.e. 2-point correlation functions of the form $\langle u_i(\omega)u_j(\omega')\rangle$ with $i \neq j$ where the u stands for the symmetric and antisymmetric $\{\hat{x}, \hat{y}\}$ modes, and the angled brackets stand for averaging over the noise. Hence the four correlation functions that yield nontrivial results to one loop order are $\langle as_y(\omega)as_y(\omega')\rangle$, $\langle s_y(\omega)s_y(\omega')\rangle$, $\langle as_x(\omega)as_x(\omega')\rangle$, $\langle s_x(\omega)s_x(\omega')\rangle$..

As described above, the calculation of these diagrams amounts to writing out the appropriate force averages and performing the appropriate loop integrals. We show the calculation of the $\langle as_y(\omega)as_y(\omega')\rangle$ as all correlation functions proceed analogously to this calculation. In addition to this, the lowest order corrections to this correlation function show the influence of the non-Gaussian part of the noise. Representative diagrams associated with the one-loop order corrections to $\langle as_y(\omega)as_y(\omega')\rangle$ are given in Fig. 4.4.2.

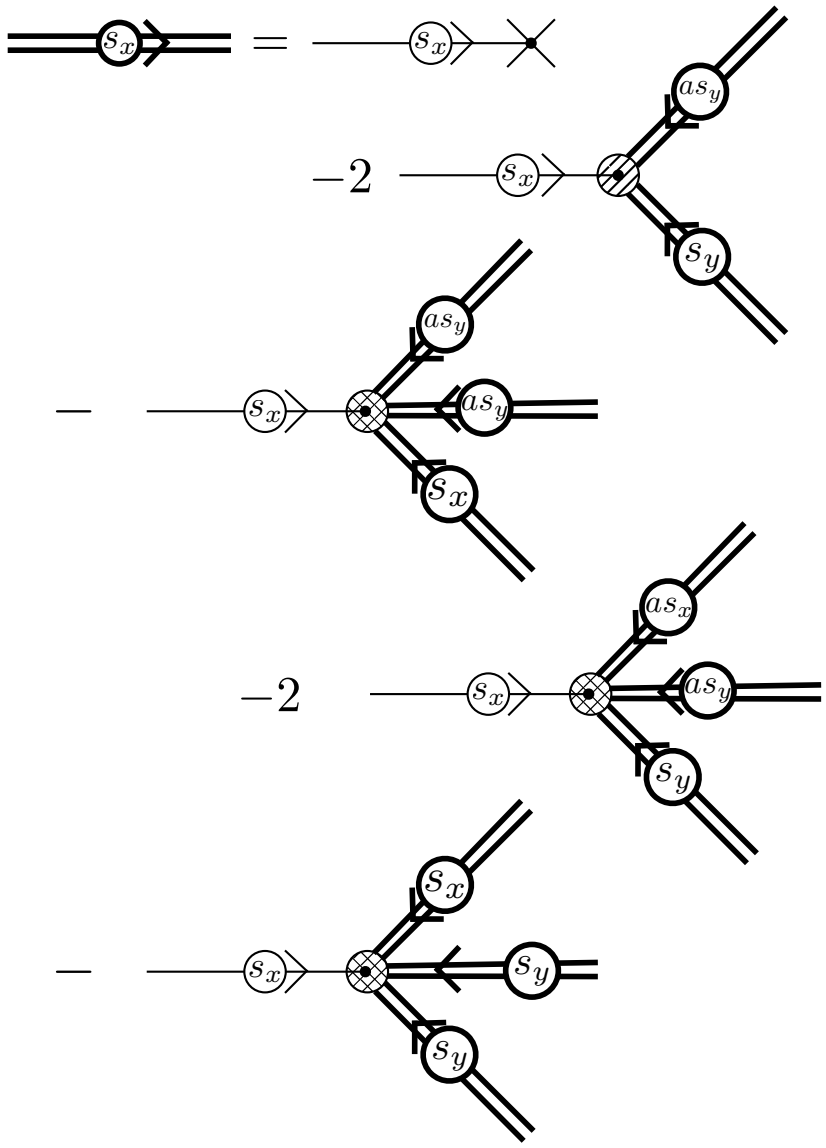

Figure 4.4.1: Diagrammatic representation of the equations of motion for the two-particle system. Rules for interpreting the diagrams are given in the text. Linear theory solution consists of the first diagram on the top.

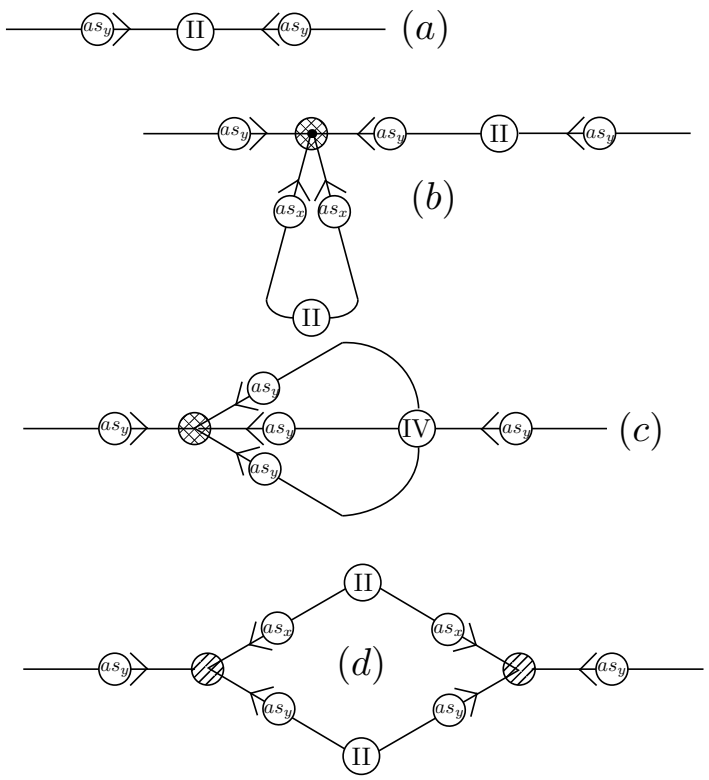

Figure 4.4.2: Diagrams representative of the types of corrections seen at one loop order to the $\langle as_y(\omega)as_y(\omega')\rangle$ function

The first type of terms involve a simple averaging of two identical force terms with different frequencies. The new feature that would not exist in the presence of the non-Gaussian, white noise is the averaging over four identical force terms. Here we must take into account that the quartic cumulant over the forces does not yield zero, but rather yields new terms. We ascribe more rules for the diagrams in order to take into account the force averaging:

- Averages over two identical force terms are denoted with a circle with the roman numeral II and are given by the appropriate term in 4.8.
- Averages over four identical force terms are denoted with a cirlce with the roman numeral IV and are given by the appropriate term in 4.8.

- Averages that involve any forces raised to some odd power yield zero.

Obviously these rules can be generalized to include high order moments, but it will be unnecessary for our lowest order corrections. Using these new rules for our Feynman diagrams, we give the results of the integrations for the four types of terms shown in Fig. 4.4.2 in order from top to bottom

$$
\begin{aligned}
(a) =& 4\pi G_{ay}(\omega)G_{ay}(\omega')\delta(\omega+\omega')(D+\Gamma_2) \\
(b) =& 2\pi\lambda_2\frac{k_{sx}}{\Gamma}(D+\Gamma_2)^2|G_{ay}(\omega')|^2 G_{ay}(\omega)\delta(\omega+\omega') \\
(c) =& 24\pi\frac{\lambda_2}{m^3}\Gamma_4 G_{ay}(\omega)G_{ay}(\omega')\delta(\omega+\omega')\times \\
& \frac{1}{\left(\omega'-\frac{3(i\,\Gamma-\sqrt{k_{ay}m-\Gamma^2})}{m}\right)\left(\omega'-\frac{3(i\,\Gamma+\sqrt{k_{ay}m-\Gamma^2})}{m}\right)}\times \\
& \frac{1}{\left(\omega'-\frac{3i\,\Gamma-\sqrt{k_{ay}m-\Gamma^2}}{m}\right)\left(\omega'-\frac{3i\,\Gamma+\sqrt{k_{ay}m-\Gamma^2}}{m}\right)} \\
(d) =& \lambda_1^2(4(D+\Gamma_2)^2)G_{ay}(\omega)G_{ay}(\omega')g(\omega,k_{ax},k_{ay})\delta(\omega+\omega')
\end{aligned}
\tag{4.10}
$$

where $g(\omega,k_i,k_j) =$

$$
\begin{aligned}
&\left(-2m^2\omega^2\left(m\left(-6k_ik_j+k_j^2+k_i^2\right)-10\Gamma^2(k_j+k_i)\right)-k_i^2m^2k_j+\right. \\
&m^4\omega^4(k_j+k_i)-k_im^2k_j^2+64\Gamma^4k_j+m^2k_j^3+16\Gamma^2mk_j^2+k_i^3m^2+ \\
&16\Gamma^2k_i^2m+64\Gamma^4k_i\Big)\Big/\Big(2\Gamma k_ik_j\left(2m^2\omega^4\left(m^2\left(2k_ik_j+3k_j^2+3k_i^2\right)\right.\right. \\
&\left.-16\Gamma^2m(k_j+k_i)+72\Gamma^4\right)-4\omega^2\left(2\Gamma^2m^2\left(-18k_ik_j+k_j^2+k_i^2\right)+\right. \\
&m^3(k_i-k_j)^2(k_j+k_i)+16\Gamma^4m(k_j+k_i)-64\Gamma^6\Big)- \\
&\left.\left.4m^4\omega^6\left(m(k_j+k_i)-6\Gamma^2\right)+\left(8\Gamma^2(k_j+k_i)+m(k_j-k_j)^2\right)^2+m^6\omega^8\right)\right)
\end{aligned}
\tag{4.11}
$$

The results for diagrams having different types of propagator lines can be easily calculated by simple replacements of the results above with the appropriate effective spring constants associated with said propagator lines.

It is worth mentioning now that there is a difference in the type of corrections seen for the correlation functions to order λ_1^2. The correlation functions for the $\hat{x}$ modes do not have any contributions from the non-Gaussian part of the noise related to the Γ_4 moments, while the s_y and as_y mode autocorrelation functions in fact do have contributions from

these cumulants. This inherent asymmetry between the modes with regard to the effect of the non-Gaussian part of the noise is not obvious, but provides an interesting insight that would be of use to study this system experimentally and determine whether there is a source of non-Gaussian noise or not.

The reasoning goes as follows: One can estimate all the system parameters of interest except for those associate with the noise fluctuations i.e. $\{D, \Gamma, \Gamma_2, \Gamma_4, \}$. In order to make an estimate of Γ, one could measure the s_x correlation function in time and look at the characteristic time scale of decay of the fluctuations. Once one has an estimate of Γ, then one could make an estimate of the sum of $D + \Gamma_2$ based on this value. This value could then be used to fit the $\{as_y, s_y\}$ correlation functions of interest. As demonstrated below, if there is a source of non-Gaussian noise near the mechanical phase transition, there will be drastic deviations from the predicted correlation function from the estimated parameters of associated with the noise. If these differences exist, one can them make an estimate of Γ_4 by looking at the differences between the measured correlation function for the as_y mode and the predicted as_y correlation function from a Gaussian theory.

Knowing now the nature of the calculations, we use the results of Eq. 4.10,and write

out $\langle as_y(\omega)as_y(\omega')\rangle$ as

$$
\begin{aligned}
\langle as_y(\omega)as_y(\omega')\rangle =& 4\pi G_{ay}(\omega)G_{ay}(\omega')\delta(\omega+\omega')(D+\Gamma_2)+ \\
& 9\left(2\pi\frac{k_{ax}}{\Gamma}(D+\Gamma_2)^2\lambda_2|G_{ay}(\omega)|^2(G_{ay}(\omega)+G_{ay}(\omega'))\delta(\omega+\omega')\right) \\
& +\left(2\pi\frac{k_{sx}}{\Gamma}(D+\Gamma_2)^2\lambda_2|G_{ay}(\omega)|^2(G_{ay}(\omega)+G_{ay}(\omega'))\delta(\omega+\omega')\right) \\
& +\frac{3}{2}\left(2\pi\frac{k_{sy}}{\Gamma}(D+\Gamma_2)^2\lambda_2|G_{ay}(\omega)|^2(G_{ay}(\omega)+G_{ay}(\omega'))\delta(\omega+\omega')\right) \\
& +\frac{27}{2}\left(2\pi\frac{k_{ay}}{\Gamma}(D+\Gamma_2)^2\lambda_2|G_{ay}(\omega)|^2(G_{ay}(\omega)+G_{ay}(\omega'))\delta(\omega+\omega')\right) \\
& +144\lambda_1^2(D+\Gamma_2)^2G_{ay}(\omega)G_{ay}(\omega')g(\omega,k_{ax},k_{ay})\delta(\omega+\omega') \\
& +16\lambda_1^2(D+\Gamma_2)^2G_{ay}(\omega)G_{ay}(\omega')g(\omega,k_{sx},k_{sy})\delta(\omega+\omega') \\
& -108\pi\frac{\lambda_2}{m^3}\Gamma_4G_{ay}(\omega)G_{ay}(\omega')\delta(\omega+\omega')\,(\\
& \frac{1}{\left(\omega'-\frac{3(i\,\Gamma-\sqrt{k_{ay}m-\Gamma^2})}{m}\right)\left(\omega'-\frac{3(i\,\Gamma+\sqrt{k_{ay}m-\Gamma^2})}{m}\right)}\times \\
& \frac{1}{\left(\omega'-\frac{3i\,\Gamma-\sqrt{k_{ay}m-\Gamma^2}}{m}\right)\left(\omega'-\frac{3i\,\Gamma+\sqrt{k_{ay}m-\Gamma^2}}{m}\right)}+ \\
& \frac{1}{\left(\omega-\frac{3(i\,\Gamma-\sqrt{k_{ay}m-\Gamma^2})}{m}\right)\left(\omega-\frac{3(i\,\Gamma+\sqrt{k_{ay}m-\Gamma^2})}{m}\right)}\times \\
& \frac{1}{\left(\omega-\frac{3i\,\Gamma-\sqrt{k_{ay}m-\Gamma^2}}{m}\right)\left(\omega-\frac{3i\,\Gamma+\sqrt{k_{ay}m-\Gamma^2}}{m}\right)}\Bigg)+\mathcal{O}(\lambda_2^2)
\end{aligned}
\tag{4.12}
$$

Though daunting, Eq. 4.12 contains the new feature that would not be encountered in the presence of strictly Gaussian noise sources, a term $\propto \Gamma_4$. The magnitude of this part of the correlation function will be examined next.

4.4.2 Analysis of the correlation functions near the critical compression

As stated before, the correlation functions for the $\hat{x}$ modes are fundamentally different in nature than the correlations in the $\hat{y}$ modes due to the presence of Γ_4 terms to order λ_1^2. Given that we are interested in seeing how non-Gaussian fluctuations look like in the presence of a second order phase transition, we examine the correlation function of as_y mode given in Eq. 4.12 near the critical compression b_c. Doing an expansion in $\delta b = b - b_c$

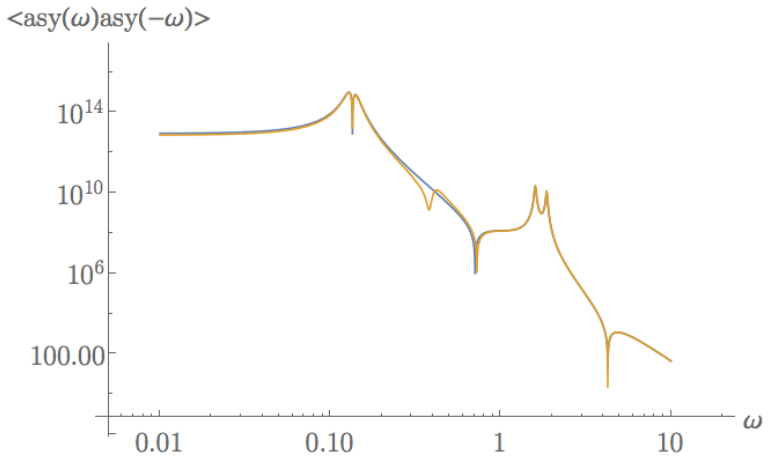

Figure 4.4.3: Comparison of the absolute value of the correlation function in the presence of (yellow) and absence of (blue) non-Gaussian, white noise for the following set of parameters $k_x = k_y = 1\,\mathrm{N/m}$, $\Gamma = 10^{-2}\,\mathrm{N\,s/m}$, $a = 1\,\mathrm{m}$, $m = 1\,\mathrm{kg}$, $D = 1\,\mathrm{N^2\,s}$, $z_0 = 10\,\mathrm{N\,s^{1/2}}$, and $\delta b = -5.9 \times 10^{-4}\,\mathrm{m}$. Note that the introduction of the non-Gaussian noise causes the correlation function to drop significantly in magnitude near the frequencies associated with the poles of the Γ_4 proportional terms in the correlation function i.e. the dip near $\omega \approx 0.25\,\mathrm{s^{-1}}$.

yields even more unruly expressions than those seen in Eq. 4.12. These functional forms yield little insight. What is more fruitful to examine is the magnitude of the correlation functions near the critical compression and to see whether the Γ_4 correction is of the same order of magnitude or larger than its Gaussian noise counterparts. We examine such a regime in Fig. 4.4.3. The figure illustrates the drastic effect of the addition of the non-Gaussian corrections to the $\mathcal{O}(\lambda_1^2)$.

At low frequencies in comparison to the inverse of the friction time scale, $\omega_f = \Gamma/m$, where the f stands for friction, the terms proportional to Γ_4 are orders of magnitude larger than those expected from a strictly Gaussian noise profile. The same holds true for the correlation function of s_y. These order of magnitude differences should be experimentally observable for a a set of particles trapped in a potential analogous to the one provided in Eq. 4.1. The fact that there is an asymmetry in the effect of the noise between the two different sets of coordinates is also striking.

This result shows that white noise fluctuations with different probability distributions are amplified differently near phase differences for a given system. As expected from our

Chapter 1, if we are examining the correlation for short times in comparison to the time scale set by the friction m/Γ, we expected to see the contributions from the non-Gaussian noise to be largest. An underdamped system is thus ideal to study the fluctuation system with non-Gaussian noise. Given our procedure above to discern between a system with strictly Gaussian noise versus non-Gaussian noise, this model system should serve well to explore the effects in experimental settings.

In particular, by examining the pole structure of the terms $\propto \Gamma_4$ we see the source of these new found differences in the correlation function. These new poles cause sign shifts in the corresponding terms in the correlation functions and lead to the new peak seen in the correlation function as given in Fig. 4.4.3. Hence, much like in Chapter 1, our non-Gaussian noise adds new features to our correlation function for time scales of order of the decay correlation time, m/Γ Hence we now have two ways to determine the presence of non-Gaussian noise in the system. Either measure the peak in the correlation function associated with the non-Gaussian noise, or do the comparison of the experimentally measured correlation function to the predicted correlation function in the presence of only Gaussian, white noise.

4.5 Discussion of Results

We have solved the equations of motion for two particles harmonically coupled to each other and their environment. We have shown that the Hamiltonian of Eq. 4.1 near its second order phase transition due to compression from the walls exhibits a drastically different correlation function behavior near its critical point in the presence of Gaussian and non-Gaussian, white noise. We have shown that non-Gaussian contributions dominate in the underdamped regime and short time scales. Finally we have given a method to measure these effects in an experimental setting by either doing a comparison of the expected correlation function in the presence of Gaussian and non-Gaussian white noise, or searching for the correlation function peak in frequency space corresponding to the contributions from the non-Gaussian noise. We expect that this system will be useful in the study in the effects of non-Gaussian noise in and lead to fundamental new understandings in the field of non-equilibrium statistical mechanics as it is amenable to studies

highly tunable atomic trapping experiments.

CHAPTER 5

Future Work and Outlook

5.1 Future work

A natural extension of the problems solved within this text would be to consider the problem of a particle escaping a potential well [47] a la Fig. 5.1.1. In future work, we will examine how the introduction of two non-interacting ideal gas buffers at different temperatures colliding with the escaping particle affect the mean escape time from one side of the well to another, along with other quantities of interest. This problem is of interest in non-equilibrium thermodynamics in general as it serves as a model for many two state systems that experience transitions from state to another which are ubiquitous throughout many branches of physics. Knowing how these transition rates change in nonequilibrium settings will be essential to making accurate predictions for much more difficult systems.

In particular, this system shown can be constructed using the type of atomic trapping experiments discussed in Chapter 3 and 4, making it an ideal system to explore the modified Kramers' escape rate problem. The methodology used to study the system in Chapter 3 also allows it to yield immediate theoretical results, and we are currently in the process of finishing these.

5.2 Summary of Results and Outlook

We found that lower dimensional systems are amenable to an exact analysis by using a Master equation approach to study the conditional probability as a function of time. Higher dimensional systems are easier studied using a Langevin-like approach. We learned that both of these approaches can model an exact master equation in Chapter 1. Hence

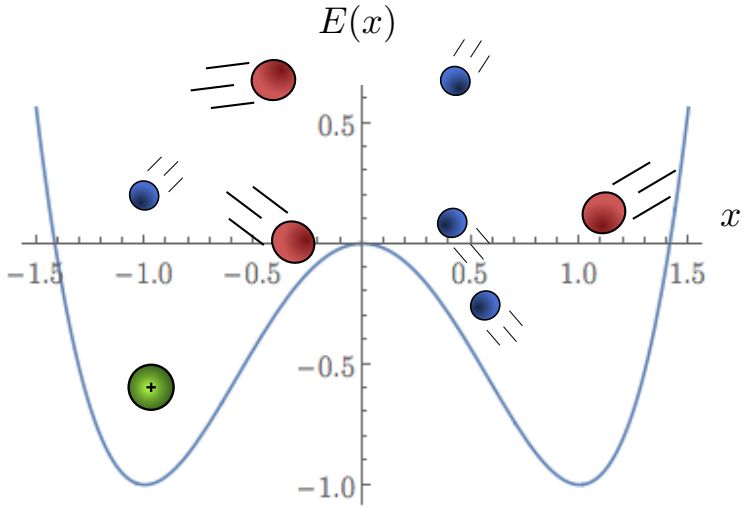

Figure 5.1.1: Schematic of the Kramers' Escape rate problem to be studied in the presence of two temperature baths. A particle resides in the left hand side minimum of the potential. One would be interested in studying the mean time of escape to the right hand side minimum of the potential.

the best way to approach any problem out of thermal equilibrium is to write down mathematical expression specific to the phenomena of interest that captures all of the details of the non-Gaussian noise.

We found that white, Gaussian noise in only appropriate in the study of systems at or near equilibrium. Though simple and useful in describing a multitude of physical phenomena, it lacks the complexity necessary to describe phenomena far out of equilibrium where contributions from rare events may lead to drastically different responses to the system which cannot be ignored. Though the collisions with hot atoms were rare with our trapped ion problem in Chapter 3, these rare events completely changed the probability distribution from the expected normal distribution to one with drastically different moments than a Gaussian distribution encountered in equilibrium physics. New phenomenology occurred where the intuition built from studying the equilibrium versions of the system failed.

We found that non-Gaussian noise introduces changes to the response function for shorter time scales that can lead to drastically different responses from the system near a phase transition, including spatial anisotropies in the response of the system. Though

a Langevin-like approach requires a perturbative expansion in a non-linear system to yield significant results, it can still model non-trivial effects in the averaged response of a system.

Though all of the types of systems studied in this work are drastically different in both their methodology of study and physical phenomena that they described, they were all systems that were out of equilibrium with their surroundings. We found that by having a thorough understanding of the phenomena, we were able to write down an appropriate stochastic theory to study the system and make testable predictions of various physical quantities of interest. Hence the best tool a theorist has when dealing with non-equilibrium systems is to have a good physical intuition for what is driving their system out of equilibrium. Though non-equilibrium systems do not share the robust theoretical framework that their equilibrium counterparts have, one must simply focus on the details of the system components to come up with a correct description and an answer, however difficult, will come.

APPENDIX A

Code for Ion Trap Experiments

Here we give a pseudo MATLAB code, representative of the code used to solve for the probability density in the Ion Trap experiment probability distribution. For full details of the Semi-Lagrangian advection method employed here see Boyd[8], Staniforth and Cote[73].

```
% Semi-Lagrangian Advection Method for Solving 1-D Master Eqn.
% author: Christian Vaca
%Set the Physical Parameters of the system.
%Working in units where Boltzmann Constant=amu=1;
M=173;%Mass of Ion.
coldgas=buffergaslangevin(40,1,10^-1,10);%Constructor for object
 % holding all parameters/methods associated with cold gas.
 %(mass,temperature,concentration,polarizability constant);
 hotgas=buffergaslangevin(2,100,10^-3,1);
 %Hot gas constructor.
 potential=rftrap(1,0,1);%Constructor for object
 %holding all parameters/methods associated with
 %potential.  (k_0,k_1,t_0).  k_0=Static Spring Constant;
 %k_1=RF Spring Constant;
 %t_0=RF Trap Period;
 %Time Steps
NOTS=100;%Number of Time Steps
```

```
tmax=10;%Max time
t=linspace(0,tmax,NOTS);%Time Vector
dt=diff(t(1:2));%Time increment

% Size of grid in velocity and position, Units of velocity in m/s;
%Position is in m.
GridDimension=2^8;
v=linspace(-1,1,GridDimension);%Velocity vector array
x=linspace(-2,2,GridDimension);%Position vector array
[X,V]=meshgrid[x,v];%2-D arrays of position and velocity
%coordinates.

%Initial State;  Delta Function Approximation
a=0.025;%As a->0, PZero becomes a Dirac Delta Function.
PZero=1/a/sqrt(pi)*exp(-(X.^2)/a^2)*1/a/sqrt(pi).*exp(-(V.^2)/a^2);
Pt=zeros(GridDimension,GridDimension,length(t));%Initialize
% each of the time slices
Pt(:,:,1)=PZero; clear PZero%Set the initial Condition

%Preallocation for variables
alpha=zeros(GridDimension,GridDimension,2);%Alpha is the distance
%traveled due to advection in the phase space.
rV=zeros(GridDimension,GridDimension);%The integral of the
%probability distribution with the transition rates.
wV=zeroes(1,length(v));%Integral over the transition rates only
wV=wVcreatorlangevin(coldgas,M)+wVcreatorlangevin(hotgas,M);
%wVcreator creates the integrated transition rates for the
%appropriate collision cross-section.
Pminus=zeroes(GridDimension,GridDimension);
```

```
%For loop to evolve probability density in time
for i=1:NOTS
alpha=alphatrap(X,V,rftrap,M,t(i),dt); %Calculation of advenction
%distance
rV=rVcreatorlangevin(X,V,alpha,coldgas,hotgas,Pt(:,:,i),M);
%Calculation of integral with transition rates and probability
%distribution.  Clenshaw-Curtis Quadrature method used.
if iterator==1
Pminus=interp2(X,V,Pt(:,:,iterator),X-alpha(:,:,1),...
V-alpha(:,:,2),'linear',0);
%Calculation of Pminus a distance alpha back necessary
%for First Order Semi-Lagrangian advection method;
Pt(:,:,i+1)=(1-dt*wV/2).*Pminus./(1+dt*wV/2)+dt*rV./(1+dt*wV/2);
%Evaluation of time step.
else
Pminus=interp2(X,V,Pt(:,:,iterator),X-2*alpha(:,:,1),...
V-2*alpha(:,:,2),'linear',0);
Pt(:,:,i+1)=(1-dt*wV).*Pminus./(1+dt*wV)+2*dt*rV./(1+dt*wV);
%Evaluation of time step for Second Order Semi-Lagrangian
%advection method
end
end
```

References

[1] C. Alkemade, N. van Kampen, and D. MacDonald. *Proc. R. Soc. Lond. A*, 271:449, 1962.

[2] A. Altland and B. Simons. *Condensed Matter Field Theory*. Cambridge University Press, 2010.

[3] A. R. Bausch and K. Kroy. A bottom-up approach to cell mechanics. *Nat Phys*, 2(4):231–238, Apr. 2006.

[4] G. I. Bell. Models for the specific adhesion of cells to cells. *Science*, 200:618, 1978.

[5] P. Benetatos and E. Frey. Depinning of semiflexible polymers. *Phys. Rev. E*, 67(5):051108, May 2003.

[6] O. J. N. Bertrand, D. K. Fygenson, and O. A. Saleh. Active, motor-driven mechanics in a DNA gel. *pnas.org*, pages 17342–17347, 2012.

[7] J. Boyd. *Chebyshev and Fourier Spectral Methods*. Dover, New York, 2001.

[8] J. P. Boyd. *Chebyshev and Fourier Spectral Methods*. Dover Publications, Inc, Mineola, New York, 2001.

[9] C. Broedersz, C. Storm, and F. MacKintosh. Nonlinear Elasticity of Composite Networks of Stiff Biopolymers with Flexible Linkers. *Phys. Rev. Lett.*, 101(11):118103, Sept. 2008.

[10] C. P. Broedersz, K. E. Kasza, L. M. Jawerth, S. Münster, D. A. Weitz, and F. C. MacKintosh. Measurement of nonlinear rheology of cross-linked biopolymer gels. *Soft Matter*, 6(17):4120, 2010.

[11] C. P. Broedersz and F. C. MacKintosh. Molecular motors stiffen non-affine semiflexible polymer networks. *Soft Matter*, 7(7):3186, 2011.

[12] T. Brotto, J.-B. Caussin, E. Lauga, and D. Bartolo. Hydrodynamics of Confined Active Fluids. *Phys. Rev. Lett.*, 110(3):038101, Jan. 2013.

[13] W. Campbell, E. Tsikata, H.-I. Lu, L. van Buuren, and J. Doyle. *Phys. Rev. Lett.*, 98:213001, 2007.

[14] P. Chakin and T. Lubensky. *Principles of Condensed Matter Physics*. Cambridge University Press, Cambridge, U.K., 1995.

[15] S. Chandrasekhar. Stochastic Problems in Physics and Astronomy. *Rev. Mod. Phys.*, 15(1):1–89, Jan. 1943.

[16] K. Chen, S. T. Sullivan, and E. R. Hudson. Neutral Gas Sympathetic Cooling of an Ion in a Paul Trap. *Phys. Rev. Lett.*, 112(14):143009, Apr. 2014.

[17] K. Chen, S. T. Sullivan, W. G. Rellergert, and E. R. Hudson. Measurement of the Coulomb Logarithm in a Radio-Frequency Paul Trap. *Phys. Rev. Lett.*, 110(17):173003, Apr. 2013.

[18] R. Côté. *Phys. Rev. Lett.*, 85:5316, 2000.

[19] M. Cross and P. Hohenberg. Pattern formation outside of equilibrium. *Rev. Mod. Phys.*, 65(3):851–1112, July 1993.

[20] C. J. Cyron, K. W. Müller, K. M. Schmoller, A. R. Bausch, W. A. Wall, and R. F. Bruinsma. Equilibrium phase diagram of semi-flexible polymer networks with linkers. *Europhys. Lett.*, 102(3):38003, May 2013.

[21] A. Dalgarno, M. R. C. McDowell, and A. Williams. The Mobilities of Ions in Unlike Gases. *Philosophical Transactions of the Royal Society A: Mathematical, Physical and Engineering Sciences*, 250(982):411–425, Apr. 1958.

[22] B. Derrida. Non-equilibrium steady states: fluctuations and large deviations of the density and of the current. *J. Stat. Mech.*, 2007(07), July 2007.

[23] R. DeVoe. *Phys. Rev. Lett.*, 102:063001, 2009.

[24] R. Dickman. Numerical analysis of the master equation. *Phys. Rev. E*, 65(4):047701, Mar. 2002.

[25] B. DiDonna and A. Levine. Filamin Cross-Linked Semiflexible Networks: Fragility under Strain. *Phys. Rev. Lett.*, 97(6):068104, Aug. 2006.

[26] B. DiDonna and A. Levine. Unfolding cross-linkers as rheology regulators in F-actin networks. *Phys. Rev. E*, 75(4):041909, Apr. 2007.

[27] G. Düring, E. Lerner, and M. Wyart. Phonon gap and localization lengths in floppy materials. *Soft Matter*, 9(1):146–154, 2012.

[28] E. Evans and K. Ritchie. Dynamic strength of molecular adhesion bonds. *Biophysical Journal*, 72(4):1541–1555, Apr. 1997.

[29] N. Fakhri, A. D. Wessel, C. Willms, M. Pasquali, D. R. Klopfenstein, F. C. MacKintosh, and C. F. Schmidt. High-resolution mapping of intracellular fluctuations using carbon nanotubes. *Science*, 344(6187):1031–1035, May 2014.

[30] A. Fetter and J. Walecka. *Quantum Theory of Many-Particle Systems*. Dover Publications, Inc, 2003.

[31] S. M. Fielding, D. Marenduzzo, and M. E. Cates. Nonlinear dynamics and rheology of active fluids: Simulations in two dimensions. *Phys. Rev. E*, 83(4):041910, Apr. 2011.

[32] Y. Fily, A. Baskaran, and M. C. Marchetti. Cooperative self-propulsion of active and passive rotors. *Soft Matter*, 8(10):3002–3009, 2012.

[33] K. Fujiwara. Fluorescent antibody localization of myosin in the cytoplasm, cleavage furrow, and mitotic spindle of human cells. *The Journal of Cell Biology*, 71(3):848–875, Dec. 1976.

[34] M. L. Gardel, I. C. Schneider, Y. Aratyn-Schaus, and C. M. Waterman. Mechanical Integration of Actin and Adhesion Dynamics in Cell Migration. *Annu. Rev. Cell Dev. Biol.*, 26(1):315–333, Nov. 2010.

[35] A. Grier et al. *Phys. Rev. Lett.*, 102(223201), 2009.

[36] A. M. Guenault and D. K. C. MacDonald. Non-Linear Brownian Movement of a Generalized Rayleigh Model. II. Extension of the Model to Include 'Sticky' Collisions. *Proceedings of the Royal Society A: Mathematical, Physical and Engineering Sciences*, 275(1361):175–189, Sept. 1963.

[37] Z. Guttenberg, A. R. Bausch, B. Hu, R. Bruinsma, L. Moroder, and E. Sackmann. Measuring LigandReceptor Unbinding Forces with Magnetic Beads: Molecular Leverage . *Langmuir*, 16(23):8984–8993, Nov. 2000.

[38] F. Hall et al. *Phys. Rev. Lett.*, 107(243202), 2011.

[39] D. Head, A. Levine, and F. MacKintosh. Deformation of Cross-Linked Semiflexible Polymer Networks. *Phys. Rev. Lett.*, 91(10):108102, Sept. 2003.

[40] C. Heussinger. Stress relaxation through crosslink unbinding in cytoskeletal networks. *New J. Phys.*, 14(9):095029, Sept. 2012.

[41] C. Jarzynski. Energy diffusion in a chaotic adiabatic billiard gas. *Phys. Rev. E*, 48(6):4340–4350, Dec. 1993.

[42] F. Jülicher, A. Ajdari, and J. Prost. *Rev. Mod. Phys.*, 69:1269, 1997.

[43] E. H. K. Chen, S.T. Sullivan. *PRL*, 112(143009), 2014.

[44] N. V. Kampen. *Stochastic Processes in Physics and Chemistry*. North-Holland, 2007.

[45] N. V. Kampen. *Stochastic Processes in Physics and Chemistry*. North-Holland, 2007.

[46] H. Kang, Q. Wen, P. A. Janmey, J. X. Tang, E. Conti, and F. C. MacKintosh. Nonlinear Elasticity of Stiff Filament Networks: Strain Stiffening, Negative Normal Stress, and Filament Alignment in Fibrin Gels . *J. Phys. Chem. B*, 113(12):3799–3805, Mar. 2009.

[47] H. Kramers. *Physica*, 7:284, 1940.

[48] R. Kubo, M. Toda, and N. Hashitsume. *Statistical Physics II: Nonequilibrium Statistical Mechanics*. Springer, 2003.

[49] L. D. Landau and E. M. Lifshitz. *Theory of Elasticity*. Pergamon Press, 1986.

[50] A. Lau and T. Lubensky. State-dependent diffusion: Thermodynamic consistency and its path integral formulation. *Phys. Rev. E*, 76(1):011123, July 2007.

[51] L. Lauer, C. Klein, and A. Offenhäusser. Spot compliant neuronal networks by structure optimized micro-contact printing. *Biomaterials*, 22(13):1925–1932, July 2001.

[52] D. Leibfried et al. *Rev. Mod. Phys.*, 75:281, 2003.

[53] A. J. Levine and F. C. MacKintosh. The Mechanics and Fluctuation Spectrum of Active Gels . *J. Phys. Chem. B*, 113(12):3820–3830, Mar. 2009.

[54] O. Lieleg and A. Bausch. Cross-Linker Unbinding and Self-Similarity in Bundled Cytoskeletal Networks. *Phys. Rev. Lett.*, 99(15):158105, Oct. 2007.

[55] O. Lieleg, M. M. A. E. Claessens, and A. R. Bausch. Structure and dynamics of cross-linked actin networks. *Soft Matter*, 6(2):218–225, 2010.

[56] F. MacKintosh and A. Levine. *Phys. Rev. Lett.*, 100:018104, 2008.

[57] F. MacKintosh and A. Levine. Nonequilibrium Mechanics and Dynamics of Motor-Activated Gels. *Phys. Rev. Lett.*, 100(1):018104, Jan. 2008.

[58] R. Mattuck. *A Guide to Feynman Diagrams in the Many-Body Problem.* Dover Publications, Inc, 1992.

[59] D. Mizuno, C. Tardin, C. F. Schmidt, and F. C. MacKintosh. Nonequilibrium Mechanics of Active Cytoskeletal Networks. *Science*, 315(5810):370–373, Jan. 2007.

[60] S. Morris, E. Bodenschatz, D. Cannell, and G. Ahlers. Spiral defect chaos in large aspect ratio Rayleigh-Bénard convection. *Phys. Rev. Lett.*, 71(13):2026–2029, Sept. 1993.

[61] K. W. Müller, R. F. Bruinsma, O. Lieleg, A. R. Bausch, W. A. Wall, and A. J. Levine. Rheology of Semiflexible Bundle Networks with Transient Linkers. *Phys. Rev. Lett.*, 112(23):238102, June 2014.

[62] J. Palacci, S. Sacanna, A. P. Steinberg, D. J. Pine, and P. M. Chaikin. Living Crystals of Light-Activated Colloidal Surfers. *Science*, 339(6122):936–940, Feb. 2013.

[63] R. Pawula. Approximation of the Linear Boltzmann Equation by the Fokker-Planck Equation. *Phys. Rev.*, 162(1):186–188, Oct. 1967.

[64] C. K. Peng, S. Havlin, J. M. Hausdorff, J. E. Mietus, H. E. Stanley, and A. L. Goldberger. Fractal mechanisms and heart rate dynamics. *Journal of Electrocardiology*, 28:59–65, Jan. 1995.

[65] W. Rellergert et al. *Phys. Rev. Lett.*, 107(243201), 2011.

[66] W. Rellergert et al. *Nature*, 495:490, 2013.

[67] J. Rudnick and G. Gaspari. *Elements of the Random Walk: An introduction for Advanced Students and Researchers.* Cambridge University Press, 2004.

[68] M. Scheffer, J. Bascompte, W. A. Brock, V. Brovkin, S. R. Carpenter, V. Dakos, H. Held, E. H. van Nes, M. Rietkerk, and G. Sugihara. Early-warning signals for critical transitions. *Nature*, 461(7260):53–59, Sept. 2009.

[69] C. Schneider et al. *Phys. Rev. Applied*, 2:034013, 2014.

[70] C. Semmrich, T. Storz, J. Glaser, R. Merkel, A. R. Bausch, and K. Kroy. Glass transition and rheological redundancy in F-actin solutions. *Proceedings of the National Academy of Sciences*, 104(51):20199–20203, Dec. 2007.

[71] D. Snyder. *Random Point Processes.* Wiley-Interscience, 1975.

[72] M. Soares e Silva, M. Depken, B. Stuhrmann, M. Korsten, F. C. MacKintosh, and G. H. Koenderink. Active multistage coarsening of actin networks driven by myosin motors. *Proceedings of the National Academy of Sciences*, 108(23):9408–9413, June 2011.

[73] A. Staniforth and J. Côté. Semi-Lagrangian Integration Schemes for Atmospheric Models—A Review. *Mon. Wea. Rev.*, 119:2206–2223, 1991.

[74] R. Thompson. Ion coulomb crystals. *Contemporary Physics*, 56(1):63–79, 2015.

[75] T. Thoresen, M. Lenz, and M. L. Gardel. Reconstitution of Contractile Actomyosin Bundles. *Biophysical Journal*, 100(11):2698–2705, June 2011.

[76] S. Trippel et al. *J. Phys.: Conf. Ser.*, 194:012046, 2009.

[77] V. K. Vanag. Inwardly Rotating Spiral Waves in a Reaction-Diffusion System. *Science*, 294(5543):835–837, Oct. 2001.

[78] K. Wang and D. Sun. Influence of semiflexible structural features of actin cytoskeleton on cell stiffness based on actin microstructural modeling. *Journal of Biomechanics*, 45(11):1900–1908, July 2012.

[79] Q. Wen, A. Basu, P. A. Janmey, and A. G. Yodh. Non-affine deformations in polymer hydrogels. *Soft Matter*, 8(31):8039–8049, 2012.

[80] R. Wester. *Phys. Chem. Chem. Phys.*, 16:396, 2014.

[81] J. Wilhelm and E. Frey. Elasticity of Stiff Polymer Networks. *Phys. Rev. Lett.*, 91(10):108103, Sept. 2003.

[82] J. L. W.W. Smith, O.P. Makarov. *J. Mod. Phys.*, 52(2253), 2005.

[83] Y. Yang, M. Bai, W. S. Klug, A. J. Levine, and M. T. Valentine. Microrheology of highly crosslinked microtubule networks is dominated by force-induced crosslinker unbinding. *Soft Matter*, 9(2):383, 2012.

[84] C. Zipkes et al. *Nature*, 464(388), 2010.